NORTHWESTERN UNIVERSITY

Anisotropic Semiconducting Thin Films: Synthesis, In-Plane and Cross-Plane Characterization, and Thermoelectric Application

A DISSERTATION

SUBMITTED TO THE GRADUATE SCHOOL
IN PARTIAL FULFILLMENT OF THE REQUIREMENTS

for the degree

DOCTOR OF PHILOSOPHY

Field of Electrical Engineering

By

Yang Tang

EVANSTON, ILLINOIS

December 2016

© Copyright by Yang Tang 2016

All Rights Reserved

Abstract

Anisotropic Semiconducting Thin Films: Synthesis, In-Plane and Cross-Plane Characterization, and Thermoelectric Application

Yang Tang

Anisotropic semiconducting thin films have attracted attention in recent years for important applications such as electrical interconnects, electronic sensors, field-emission devices and thermoelectric devices. However, the characterization of the full conductivity tensor, especially the cross-plane conductivity, remains a great challenge for anisotropic thin films. In addition, the synthesis of large-area thin-film conductors with controllable in-plane conductivity anisotropy is not thoroughly studied. To address these problems, this work explores new directions in the characterization, synthesis, and applications of anisotropic conductors.

A new method to characterize the in-plane and cross-plane electrical conductivity of anisotropic semiconductor thin films is proposed. In this method, a "triple stripline" device structure is created by adding three narrow stripline contacts to the top of the anisotropic thin-film layer of interest. The substrate is assumed to be highly conductive, as is typical for optical devices, and serves as a grounding back-plane. The electrostatic

potential distribution of this device is proved to have no analytical solution and solved numerically. It is shown that experimental measurements of the potential can uniquely determine all components of the conductivity tensor. Initial progress towards an experimental demonstration is presented.

Three semiconducting thin films with artificial in-plane conductivity anisotropy are synthesized: the carbon nanotube (CNT) film, the graphene-polymer film, and the AlGaAs thin film. The conduction channels for these three films are aligned by evaporation-driven self-assembly, three-dimensional printing, and ion-implantation isolation, respectively. Anisotropy ratios above 10^4 are observed for both the CNT and AlGaAs thin films. While the CNT and graphene-polymer films are p-type, the AlGaAs film can be doped to be either n or p-type.

"Cross-hatched" n and p-type anisotropic thin-film conductors with conducting axes orthogonal to each other can open up new applications in $p \times n$-type transverse thermoelectrics, in which the induced heat flow is perpendicular to the applied electric current or conversely, the generated electric field is perpendicular to the applied temperature gradient. The theory of transverse thermoelectrics is studied with normalized electric field and heat flux scales, and the maximum cooling performance is presented here for the first time. The theoretical model of the $p \times n$-type transverse thermoelectrics is reviewed, and candidate materials are proposed. Among the candidate materials, artificially structured anisotropic thin films are shown to enable the cross-hatched $p \times n$ structures, and development towards a $p \times n$ AlGaAs structure is reported.

Acknowledgements

Firstly, I would like to express my sincere gratitude to my advisor Prof. Matthew Grayson for the continuous support of my Ph.D. study and related research, for his patience, motivation, and immense knowledge. His guidance helped me in all the time of research and writing of this thesis. I could not have imagined having a better advisor and mentor for my Ph.D. study.

Besides my advisor, I would like to thank the rest of my thesis committee: Prof. Manijeh Razeghi, Prof. Ramille Nirav Shah, Prof. Selim M. Shahriar and Prof. Koray Aydin, and the rest of my prospectus committee: Prof. Mark Hersam and Prof. Lincoln James Lauhon for their insightful comments and encouragement, but also for the hard question which incented me to widen my research from various perspectives.

I thank my fellow labmates in for the stimulating discussions, for the sleepless nights we were working together before deadlines, and for all the fun we have had in the last several years. Also, I thank my friends in the following institution: Nufab, ISEN, and Ryan Fellows. In particular, I am grateful to Dr. Chuanle Zhou and Dr. Ming Ma for their inspiring work and insightful discussions.

My sincere thanks also goes to Dr. Gregor Koblmller, Dr. Adam Jakus, Dr. Tejas Shastry, Dr. Arpun Nagaraja, Dr. Blake Stevens, Kevin Roche, Sam Davis, and Dr. Taewan Noh, who provided me opportunities to collaborate, and who gave me great help

on research facilities. Without they precious support it would not be possible to conduct this research.

Last but not the least, I would like to thank my family: my parents and to my fiance for supporting me spiritually throughout my Ph.D. study, thesis writing and my life in general.

Contents

Abstract 3

Acknowledgements 5

List of Tables 9

List of Figures 10

Chapter 1. Introduction to anisotropic conductors 28

1.1. Anisotropic electrical conductivity tensor characterization 28

1.2. Synthesis of anisotropic conductors 34

1.3. Application of anisotropic conductors 37

1.4. Thesis outline 38

Chapter 2. Triple stripline method: characterizing conductivity of anisotropic thin films 39

2.1. Magnetotransport potentional distribution in anisotropic thin films: Analytical description of the problem 39

2.2. Magnetotransport potentional distribution in anisotropic thin films: Numerical solution 46

2.3. Triple stripline method: theory 62

2.4. Triple stripline method: device fabrication 77

Chapter 3. Synthesis of anisotropic thin film semiconductors 86
3.1. Aligned carbon nanotube (CNT) stripes 86
3.2. 3D-printed graphene-polymer stripes 98
3.3. Ion implantation-induced anisotropy in semiconducting layers 113

Chapter 4. $p \times n$-type transverse thermoelectrics: Application of anisotropic conductors 125
4.1. Introduction to transverse thermoelectrics 126
4.2. Cooling power of transverse thermoelectrics 133
4.3. $p \times n$-type transverse thermoelectrics model 145
4.4. $p \times n$-type transverse thermoelectrics candidates 150
4.5. Cross-hatched $p \times n$ layer interconnect model 156
4.6. Cross-hatched $p \times n$ AlGaAs fabrication progress and future work 161

Bibliography 168

Appendix A. Transverse thermoelectric phenomena 183

Vita 191

List of Tables

1.1 Conductivity tensors for 3D and 2D materials with principle crystalline axes unaligned and aligned with respect to the x, y, z-measurement axes, or aligned in the presence of a magnetic field $\boldsymbol{B}$. For 2D materials, the magnetic field direction is perpendicular to the plane $\boldsymbol{B} = B_z \hat{z}$. 29

3.1 The fluctuation-induced tunneling model fitting parameters for the temperature dependent anisotropic conductivities in Fig. 3.10. 109

3.2 The low temperature ($T = 4$ K) hole density p and anisotropic mobilities μ_x, μ_y estimated from the slope of R_{xy} near $B = 5$ T. 113

3.3 The post-anneal resistivity and anisotropy ratio at $T = 300$ K. 120

4.1 The geometrically corrected Seebeck coefficient for $p + n$-AlGaAs and single layer AlGaAs. 165

List of Figures

1.1 An L-shape Hall bar in the x-y plane in the presence of a magnetic field B_z. The current I_x and I_y are applied along the principal axis directions x and y, respectively. The longitudinal resistances along two directions R_{xx} and R_{yy} are measured with two voltage contacts along the bar, and the Hall resistance R_{xy} is measured with two voltage contacts across the bar. 30

1.2 Vertical magnetoresistance measurement setup for p-type InAs/GaSb type-II superlattices by Umana-Membreno *et al.* [**1**]. This measurement method is only able to extract the longitudinal component of the resistivity tensor ρ_{yy} and the other two components ρ_{xx} and ρ_{xy} are missing, which reduces the reliability and accuracy of the extraction of the conductivity tensor, carrier density, and mobilities. 32

1.3 (a) The crystal structure of $YBa_2Cu_3O_{6+x}$ showing the conducting Cu-O layers perpendicular to the c-axis. Figure reproduced from Ref. [**2**]. (b) Application of anisotropic conductive film (ACF) for circuitry connection [**3**]. 35

1.4 (a) Isotropic nanomaterials: 0D spheres and clusters and Anisotropic nanomaterials: (b) 1D nanofibers, wires, and rods, (c) 2D films, plates, and networks, and (d) 3D nanomaterials (reproduced from Ref. [**4**]). (e) Schematic showing the slip-stick behavior of evaporation-driven self-assembly (EDSA), reproduced from Ref. [**5**]. (f) Schematic of the capillary printing process using a nano-patterned PDMS stamp to produce highly aligned Ag nanowire arrays, reproduced from Ref. [**6**]. 36

2.1 (a) The typical structure of optical device layers, with an active layer sitting between two highly conductive top- and bottom-contacts. (b) The proposed single stripline diagnostic structure. The top conducting layer is etched away, and the bottom conducting layer is used as a ground plane. One narrow contact stripline is deposited on the top of the active layer. The electromagnetic potential distribution of this structure will be calculated as a first step towards developing a measurement method of the full conductivity tensor. 41

2.2 Calculation of the amount of current flowing through the elementary segment before and after the conformal map. The isotropic z'-plane is conformally mapped into the w-plane, whereby the elementary segment $d\boldsymbol{L_{z'}}$ and the current density $\boldsymbol{j_{z'}}$ that passes it are transformed to $d\boldsymbol{L_w}$ and $\boldsymbol{j_w}$, respectively. The total amount of current flowing through $d\boldsymbol{L_{z'}}$ and $d\boldsymbol{L_w}$ should be identical. 50

2.3 The conformal maps transforming the infinite strip from (a) z'-plane to (b) upper half s-plane, to (c) a finite rectangle in the w-plane. The purple line in all three plots represents the Dirichlet boundary at fixed ground potential, and the black dot or string of dots represent the Dirichlet boundary at potential V. The red and green circles trace specific boundary points that map to the corners in the w-plane of panel (c). 52

2.4 Triangle meshes generated in the finite rectangle in w-plane for FEM simulation. The rectangle is divided into small triangle elements using DistMesh [**7**]. The mesh density is enhanced near the stripline contact and the edges and corners of the rectangle, where the boundary conditions are applied, and a higher resolution is preferred. 55

2.5 The FEM simulated potential distribution (red lines) and current flux density (blue lines) in a finite rectangle with top and bottom facet contacts with (a) zero and (b) non-zero off-diagonal component of the conductivity tensor. A Hall angle $\theta_H = \arctan(\sigma_{uv}/\sigma_{uu})$ is formed between the current flux and potential gradient directions. 56

2.6 (a) The calculated potential distribution (red lines) and current flux density (blue lines) in the finite isotropic rectangle (w-plane) corresponding to $\sigma_{yy}/\sigma_{xx} = 2$ and $\sigma_{xy}/\sigma_{xx} = 1$ in the z-plane coordinates. (b) The potential distribution in the upper-half s-plane is mapped with an inverse Schwarz-Christoffel transformation from the w-plane. (c) The potential distribution in the z-plane is mapped

with the inverse scaling transformation from the s-plane. The dots represent the locations of the top stripline contact (black) and corner coordinates in the w-plane (red and green). The purple line represents the ground plane. 58

2.7 The FEM-calculated potential distribution in finite rectangles with isotropic conductivity are mapped to the infinite strip with $\sigma_{xy} = 0$ and anisotropy ratio (a) $A = \sigma_{yy}/\sigma_{xx} = 0.2$, (b) $A = 1$ (isotropic), and (c) $A = 5$. The mapped rectangles have thickness $t_v = 10$ and width $W_u = 17.7, 28.8, 53.5$ respectively. The resultant potential distribution representing the anisotropic infinite strip is shown in (d)-(f). The dots represent the stripline contact (black) and w-plane corner points (red and green), and the purple line represents the ground plane. 59

2.8 The FEM-calculated potential distribution for the case of an infinite strip with isotropic conductivity ($A = 1$) is plotted for various magnetic field strengths represented by $\sigma_{xy}/\sigma_{xx} =$ (a) 0.2, (b) 1 and (c) 5. Because all plots are derived for the same conductivity anisotropy ratio $A = 1$, namely the isotropic case, the mapped rectangles have the same thickness $t_v = 10$ and width $W_u = 28.8$. The resultant potential distribution representing the infinite isotropic strip in a finite B-field is shown in (d)-(f).The dots represent the stripline contact (black) and w-plane corner points (red and green), and the purple line represents the ground plane. 61

2.9 The triple stripline device structure for measuring the three independent conductivity components of an anisotropic active layer on a conducting substrate. Three narrow stripline electrodes are deposited on top of the active layer, with a pitch width equal to the active layer thickness t and a width much smaller than t. 63

2.10 Two measurement setups with the triple stripline device. (a) Measurement I: apply current I from the left-most stripline contact 1 and measure four-point voltages V_2, V_3 relative to the ground plane. (b) Measurement II: apply current I from the center stripline contact 2 and measure voltages V_1, V_3 from the two sides relative to the ground plane. 65

2.11 (a) The potential distribution of the infinite strip for different conductivity anisotropy ratio $A = \sigma_{yy}/\sigma_{xx}$, when $\sigma_{xy} = 0$ reproduced from Fig. 2.7 (d)-(f). (b) The calculated voltage ratio V_2/V_3 increases monotonically with the anisotropy ratio $A = \sigma_{yy}/\sigma_{xx}$. 68

2.12 (a) The potential distribution of the infinite strip for isotropic conductivities ($A = \sigma_{yy}/\sigma_{xx} = 1$) with varied $\tan\theta_H = \sigma_{xy}/\sigma_{xx}$ ratios, which can be induced by different magnetic field strengths, as reproduced from Fig. 2.8(d)-(f). (b) The calculated voltage ratio V_1/V_3 increases monotonically with the tangent Hall angle $\tan\theta_H = \sigma_{xy}/\sigma_{xx}$. 69

2.13 Contour map of with iso-voltage-ratio lines V_2/V_3 (measurement I, solid line) and V_1/V_3 (measurement II, dashed line) for the tangent

Hall angle $\sigma_{xy}/sigma_{xx}$ and anisotropy ratio σ_{yy}/σ_{xx}. For any pair of measured voltage ratios, *e.g.* $V_2/V_3 = 6$ and $V_1/V_3 = 12$, corresponding contour lines can be located from the map (blue and red), and their intersection uniquely defines the values for σ_{yy}/σ_{xx} and σ_{xy}/σ_{xx}. 71

2.14 Contour map of the factor g as a function of the conductivity component ratios σ_{yy}/σ_{xx} and σ_{xy}/σ_{xx}. Once g is determined, the conductivity component amplitude can be calculated with $\sigma_{xx} = g\left(\frac{\sigma_{yy}}{\sigma_{xx}}, \frac{\sigma_{xy}}{\sigma_{xx}}\right)\frac{I}{V_{23}\cdot L}$, whereby $V_{23} = V_2 - V_3$ in the first measurement. 72

2.15 Contour map of V_2/V_3 (Measurement I), solid line) and V_1/V_3 (Measurement I), dashed line) as a function of the conductivity anisotropy ratio σ_{yy}/σ_{xx} and the ratio σ_{xy}/σ_{xx}, identical to Fig. 2.13, but for a larger range.. 75

2.16 Two measurement setups with the penta stripline device. (a) Apply current I between two side stripline contacts on top and measure four-point voltages V_2, V_3 relative to the ground. b) Apply current I from the center stripline contact and ground the two contacts on two sides, measure voltages V_2, V_4 of the stripline contacts between the current source and ground. 77

2.17 The growth protocol of GaAs and GaAs/AlGaAs superlattice based triple stripline devices. The 3 µm thick active layer is lightly doped ($N_D = 2 \times 10^{16}\text{cm}^{-2}$) (a) single crystal GaAs with (100)

orientation (b) GaAs/$Al_{0.33}Ga_{0.67}As$ (115 / 15 Å) suplerlattice and (c) GaAs/$Al_{0.33}Ga_{0.67}As$ (100 / 30 Å). The three different active layers will provide different conductivity anisotropy ratios. 78

2.18 E-beam and photolithography mask patterns (a)-(c) and zoom-in for narrow metal stripline evaporation patterns (d). 80

2.19 SEM images of the metal strip contacts after liftoff with ebeam lithography bilayer resist consisting of : (a) PMGI + PMMA, (b) MMA (3000 rpm) + PMMA (4000 rpm) and (c) MMA (2000 rpm) + PMMA (3000 rpm). The number in the parentheses is the spinning rate, the lower of which leads to the thicker and more stiff resist layer. The ebeam lithography pattern line width is set to be $W = 250$ nm. The latter two resist combinations have different width for different layers of the metalization, which may be attributed to the larger undercut and smaller thickness compared with the first resist combination. 81

2.20 Dosage test for PMGI + PMMA bilayer resist. The SEM images of the metal strips after liftoff with various dosages are shown on top. The zoom-in images at bottom show that the width of the metal strips increase with dosage. 83

2.21 Cross-section view of the triple stripline device with T-shape narrow stripline contacts. The metal contacts have narrower bottom width to fit the point contact model, and larger top width to reduce the metal

strip resistance and ensure the uniform potential distribution along the strip direction. 85

3.1 Scanning electron microscopy (SEM) images of aligned single-wall carbon nanotube (SWCNT) stripes with stripe width of (a) $W \sim$ 1-3 μm (b) $W \sim$ 5-7 μm. For each panel, the morphology of stripes is shown in the top images. Each stripe consists of a group of aligned SWCNT bundles around 10-15 nm in diameter as shown in the high-contrast SEM images of a single stripe at the bottom. The wider stripe shows better morphological uniformity and alignment. 88

3.2 (a) Scanning electron microscopy (SEM) images of aligned CNT stripes deposited on a Si substrate with SiO_2 insulating layer. Gold pads are deposited on top of CNT stripes. The 4-probe method is used to measure the longitudinal resistance between two adjacent gold pads: $R_{||} = (V_+ - V_-)/I$. (b) Average longitudinal conductivity $\sigma_{||}$ (triangles) for different width of as-grown p-type CNT stripes. The longitudinal resistance $R_{||}$ (circles) for multiple CNT stripes between two gold pads is measured to be decreasing with increasing stripe width W. The stripe width/pitch ratio W/P (squares) increases almost linearly when $W < 10$ μm, and stays around 0.5 for 10 μm $< W < 20$ μm. 90

3.3 Longitudinal conductance $G_{||}$ hysteresis versus gate voltage from -20 V to +20 V. $G_{||}$ is determined by taking an $I - V$ curve at

each V_g value plotted above. The device structure is similar to a back-gated CNT-based field-effect transistor, as shown in the inset. The red arrows depict the sweep directions. For V_g up to +20 V, the p-CNT channel is still not pinched off, as indicated by non-zero $G_{||}$, which may be caused by the much larger thickness of the CNT stripes compared with the diameter of a single CNT. The hysteresis is attributed to the injection and trapping/de-trapping of carriers in the SiO_2 at large V_g [**8**]. 92

3.4 (a) Microprobe Seebeck measurement set-up compatible with probe-station measurement. (b) Average longitudinal Seebeck coefficient of 20 μm wide aligned p-type SWCNT stripes under different gate voltages. The results show that $S_{||}$ does not depend on gate voltage in the range of −20 V to 20 V. 93

3.5 Longitudinal Seebeck coefficient $S_{||}$ measurement for nominally n-doped aligned CNT stripes of width around 5-7 μm. The as-grown CNT stripes (black) show p-type Seebeck coefficient + 15.4 μV/K, which decreases after viologen-doping (red) and decreases further after annealing (blue) since the annealing assists the dopant diffusion and oxygen desorption. However, the Seebeck coefficient remains p-type. After exposing to air for 48 hours the Seebeck coefficient recovers to the value before annealing (cyan), indicating the original "n-doping" effect was air-stable within this time scale while the annealing effect

disappeared. Another attempt of n-doping with HfO_2 dissipation layer (purple) shows similar reduced p-type $S_{||}$. 95

3.6 The bottom and top surfaces of 3DG thin films printed with nozzle diameter (a) $D = 100$ μm, (b) $D = 200$ μm, (c) $D = 400$ μm and (d) $D = 800$ μm. The stripe width of the printed film is roughly equal to the nozzle diameter. The top surface is corrugated, and the width of the grooves between adjacent stripes increases with the nozzle diameter D. 99

3.7 The (a) bottom and (b) top surface profile of 3DG films printed with nozzle diameters $D = 100$, 200, 400 and 800 μm. The film thickness t is typically around half of D, due to the ink spreading before drying up. The top surface shows a much larger roughness compared with the bottom surface, as indicated by the depth of the deepest valley R_v in the figure legend. 101

3.8 The anisotropic van der Pauw measurement contact configurations and results for the 3DG film printed with nozzle diameter $D = 100$ μm, measured at $T = 300$ K. The resistance anisotropy $A_R = R_{AD,BC}/R_{AB,DC}$ is measured for different combinations of the four contacts, and the resistivity anisotropy $A_\rho = \rho_{yy}/\rho_{xx}$ is calculated via anisotropic scaling and conformal mapping. The consistency in A_ρ of different configurations indicate the validity of the anisotropic van der Pauw method. Note for four edge center contacts in (d), $A_R = 1$

is expected independent of A_ρ. The deviation from 1 can be partially attributed to the contact displacement. 102

3.9 The temperature dependence of (a) the anisotropic resistivity components ρ_{xx}, ρ_{yy} and (b) their ratio $A_\rho = \rho_{yy}/\rho_{xx}$ for 3DG thin films printed with different nozzle diameter D. Both ρ_{xx} and ρ_{yy} slightly increase as the temperature decreases from $T = 300$ K to 4 K, except for ρ_{yy} for the thin film with nozzle diameter $D = 800$ μm, which reduces by about 15% when the temperature decreases from $T = 300$ K to 140 K. The resistivity anisotropy ratio is robustly temperature independent for most samples, with the exception described above for the $D = 800$ μm at higher temperatures. 105

3.10 The anisotropic conductivities versus temperature fitted by fluctuation-induced tunneling model for 3DG thin films printed with different nozzle diameter D. The median value of the tunneling junction width w is proportional to the ratio T_1/T_0. Note for the $D = 800$ μm sample, only the lower half of the temperature range ($T = 4$ K to 140 K) is fitted. 108

3.11 The Hall resistance R_{xy} measured at $T = 300$ K and $T = 4$ K for 3DG films printed with varied nozzle diameter D. At 300 K, R_{xy} is smaller than the noise level due to the high carrier concentration. At 4 K, the overall positive slope of R_{xy} at large B indicates that p-type conduction dominates the electrical conduction of the 3DG films. However, the concavity at weak magnetic field can be evidence that

n-type conduction of electrons also contribute to the total conduction. The larger amplitude of Hall resistance for thinner films with smaller D is mainly due to their smaller thickness. 110

3.12 The magnetoresistance (top panels) along the longitudinal (R_{xx}, solid squares) and transverse directions (R_{yy}, open circles) for 3DG thin films printed with various nozzle diameters D and the measured resistance anisotropy $A_R = R_{yy}/R_{xx}$ (solid lines, bottom panels) at (a) $T = 300$ K and (b) $T = 4$ K. A_R only decreases by 1 - 2% as the magnetic field B increases from 0 T to 5 T. Note A_R is different from the resistivity anisotropy $A_\rho = \rho_{yy}/\rho_{xx}$. 112

3.13 (a) Schematic of the $Al_{0.42}Ga_{0.58}As$ thin film and proton ion implantation. The doped $Al_{0.42}Ga_{0.58}As$ thin film is electrically isolated from the substrate with the GaAs/$Al_{0.42}Ga_{0.58}As$ superlattices. The SiO_2 mask layer is patterned into stripes by photolithography and wet etching, and defines the protected and damaged regions of $Al_{0.42}Ga_{0.58}As$ in proton (H^+) implantation. The strip width and separation between strips are both 10 μm. (b) The etched L-shaped Hall bar of ion-implanted $Al_{0.42}Ga_{0.58}As$ and resistance measurement set-up. An AC current I is sent through the Hall bar and the voltage drops V_{xx} and V_{yy} can be measured with the voltage contacts on the side, from which the transverse ($\rho_\perp$) and parallel ($\rho_\parallel$) resistivities to the ion-implanted strip direction can be determined. 115

3.14 SRIM [**9**] simulated proton and vacancy defect profile for different proton energies when the $Al_{0.42}Ga_{0.58}As$ layer is 500 nm thick. The dosage used for this simulation is $D = 5 \times 10^{15}$ cm^{-2}. 117

3.15 The SRIM simulation of the implanted proton distribution compared to SIMS measurement of (a) As-grown p-type doped $Al_{0.42}Ga_{0.58}As$ and (b) annealed n-type doped $Al_{0.42}Ga_{0.58}As$. The measured Al and Ga fraction peaks/valleys indicate the depth of the $GaAs/Al_{0.42}Ga_{0.58}As$ superlattice barrier below the doped $Al_{0.42}Ga_{0.58}As$ layer. The peak proton density agrees with simulation for the as-grown sample, and is smaller for the annealed one. Integration of the proton density over depth indicates that more than 50% of the implanted protons diffused towards the surface and more than 30% diffused out of the sample. 119

3.16 The temperature-dependent resistivity of pristine and ion-implanted (a) n-type and (b) p-type $Al_{0.42}Ga_{0.58}As$. For the ion-implanted samples, only the longitudinal resistivity along the conduction channel direction ($\rho_{\parallel}$) is plotted, the transverse resistivity ($\rho_{\perp}$) is at least four orders larger and cannot be accurately determined due to parallel conduction through the highly insulating substrate. The temperature ranges span from room temperature to the lowest temperature where contacts fail, which is around 200 K for n-type and lower than 10 K for p-type. The room temperature longitudinal resistivity increases only by a factor of 3.3 and 3.6 at room temperature after proton

implantation and annealing, indicating that extreme conductance anisotropies can be realized by ion-implantation isolation. 121

3.17 The temperature-dependent Seebeck coefficient of pristine and ion-implanted n-type $Al_{0.42}Ga_{0.58}As$. For the ion-implanted samples, only the longitudinal Seebeck coefficient along the conduction channel direction ($S_{\parallel}$) is plotted, the transverse Seebeck coefficient ($S_{\perp}$) is not measurable. 123

4.1 (a) Longitudinal (b) Transverse thermoelectric Peltier coolers, whereby heat flow (Q, white arrows) from cold side (T_C) to hot side (T_H) is induced by the applied electrical current density (J, black arrows). The subscripts x, y denote the directions of Q and J. Q_y is parallel/anti-parallel to J_y in (a), and transverse to J_x in (b). 129

4.2 (a) Longitudinal and (b) transverse thermoelectric generators for large Seebeck voltage generation. To increase the generated Seebeck voltage $V_+ - V_-$ from a given temperature different $T_H - T_C$, the longitudinal generator requires many thermoelements linked in series, which involves the arrangement of alternate n and p-legs with increasing junction resistance. The transverse thermoelectric generator can just increase the length-to-thickness ratio L_x/L_y. 130

4.3 (a) Cascaded longitudinal Peltier cooler and (b) exponentially tapered transverse Peltier cooler for large thermal differences. Note the simplicity of the single-leg structure on the right. 132

4.4 Normalized temperature profile of transverse thermoelectric coolers operating at maximum temperature difference for various zT_h values. At $y^* = y/L_y = 0$ the heat sink temperature $T^* = T/T_h = 1$ and at the $y^* = 1$ the cold side heat flow $Q_c = Q_y(y^* = 1) = 0$. 137

4.5 The dependence on zT of maximum normalized temperature difference (left axis) whereby $\Delta T^* = (T_h - T_c)/T_h$ and maximum cooling power density when $T_c = T_h$ (right axis) for transverse thermoelectric coolers in comparison with longitudinal coolers. $\Delta T^*_{\mathrm{max}}$ and $Q^*_{\mathrm{c,max}}(T^*_c = 1)$ are numerically calculated for the transverse coolers but can be analytically solved for the longitudinal coolers [**10**, **11**]. 138

4.6 The maximum normalized cooling power density $Q^*_{\mathrm{c,max}}$ for transverse thermoelectric cooling as a function of the normalized cold side temperature T^*_c for various zT_h values. 140

4.7 The dependence on zT_h of maximum normalized temperature difference whereby $\Delta T^* = (T_h - T_c)/T_h$ for an exponentially tapered transverse cooler with $L_x(y) = L_x(0)e^{(-y/L)}$. The parameter L_y/L defines the overall shape of the tapered coolers, since $L_x(y = L_y)/L_x(0) = e^{(-L_y/L)}$, *i.e.*, the larger L_y/L is, the narrower the top width is relative to the bottom width. 142

4.8 (a) Equivalent effective zT_h values to achieve the same normalized temperature difference with a rectangular transverse cooler for various tapering parameters L_y/L. (b) The effective zT_h enhancement depends on the tapering parameter. 143

4.9 (a) The maximum normalized cooling power density $Q^*_{\mathrm{c,max}}$ for an exponentially tapered transverse cooler as a function of the normalized cold side temperature T^*_c for various tapering parameters L_y/L. The figure of merit is assumed to be $zT_h = 1.0$. (b) $Q^*_{\mathrm{c,max}}e^{(-L_y/L)}$ scales the cooling power density at the tapered top by the reduced area of the top surface to effectively give the cooling power density per unit base-area. This is plotted versus T^*_c. 144

4.10 $p \times n$-type thermoelectrics have p-type dominated conduction and Seebeck coefficient along the a-axis and n-type dominated conduction and Seebeck coefficient along the orthogonal b-axis, as indicated by the crossed arrow symbol at the bottom right. The movement of electrons (orange dashed arrows) and holes (green solid arrows) in orthogonal directions results in net charge current J_x to the right and net particle or heat flow Q_y up. The carrier transport shown in this figure can be driven either by drift due to an electric field along $+x$ direction or by diffusion due to a temperature gradient along $-y$ direction [**12**]. 147

4.11 (a) Band alignment of T2SL, where the grey color indicates the forbidden bandgap. GaSb valence band E_V (green) lies energetically above the InAs conduction band E_C (orange). E_F is the Fermi energy. $E_{0,e}$ is the ground energy for electron band, and $E_{0,hh}$ is the the ground energy for heavy hole band. (b) Dispersions simulated using nextnano $8 \times 8 k \cdot p$ envelope function method [**13, 14**]. The in-plane

dispersion is to the left of $k = 0$, and the out-of-plane dispersion to the right of $k = 0$. $\Delta_{sp} = E_s - E_p$ is the $s - p$ band difference. (c) Plot of the optimized $Z_{\perp}T$ at 300 K as a function of different InAs and GaSb layer thicknesses [**15**]. 152

4.12 Cross-hatched $p \times n$ transverse thermoelectrics. (a) By alternatively aligning n-type conduction channel array and orthogonally oriented p-type conduction channel array, $p \times n$ conduction is realized. (b) A schematic diagram of cross-hatched transverse thermoelectric cooler. With an applied current J, electron-hole pairs are generated at top surface absorbing heat and recombine at the bottom giving off heat, cooling top surface. 154

4.13 (a) Diagram of a cross-hatched $p \times n$ Seebeck generator. The p-type (blue strips) and n-type (orange strips) conduction channels are aligned with angle θ_p and θ_n to x axis, respectively. With a temperature difference applied to the left and right surfaces, a transverse Seebeck voltage is generated in the y direction, driving a current I through the load resistor R_L. (b) The formation of tilted longitudinal thermocouple. In the open-circuit model, one pair of p and n channels that overlap at the left/right edges effectively forms a tilted longitudinal thermocouple. 159

4.14 The overall fabrication flow for cross-hatched $p \times n$ AlGaAs crystal. The p and n-type conduction channels are created via ion implantation isolation. 162

4.15 Growth protocol of the $p + n$ bilayer $Al_{0.42}Ga_{0.58}As$ structure. 163

4.16 (a) Photomask patterns for on-chip Seebeck measurement device. (b) Example Seebeck measurement result for the $p + n$ AlGaAs structure with both layers grown at once. S_p and S_n are directly extracted from the slop of the Seebeck voltage measured at two outer contacts, which require further scaling to compensate for the over-estimated temperature difference. 164

4.17 (a) The wafer-scale photolithography patterns for cross-hatched $p \times n$ AlGaAs. (b) Transverse Seebeck measurement device structure. n and p-type ohmic contacts are alternatively deposited on left and right edges and to avoid shorting the temperature difference between top and bottom edges. 167

A.1 (a) NernstEttingshausen effect. In the presence of a B-field, electrons and holes in a semimetal or narrow-gap semiconductor both feel a Lorenz force component in the upwards direction, resulting in a net heat flow transverse to the electrical current. (b) A stacked synthetic transverse thermoelement cut from a two-phase (1 and 2) layered material. The anisotropic Seebeck tensor arises from having the layers in series along one axis, and in parallel along the other axis. 184

CHAPTER 1

Introduction to anisotropic conductors

Anisotropic conductors, with distinct properties in each direction, have attracted tremendous attention in recent years for their important applications such as electronic sensors, field-emission devices, and magnetic devices [16–18]. This chapter is a general introduction to anisotropic conductors. We start with the electrical conductivity tensor representation of anisotropic conductors and introduce the state of art characterization techniques in Section 1.1. The challenges in characterizing anisotropic thin film conductors in both in-plane and cross-plane directions will be presented. In addition, we will cover different categories of anisotropic thin films and the corresponding synthesis methods in Section 1.2. And finally, we discuss the applications of anisotropic conductors in Section 1.3.

1.1. Anisotropic electrical conductivity tensor characterization

The electrical transport properties of anisotropic conductors can be characterized by measuring the conductivity tensor. The generic form of the conductivity tensor $\boldsymbol{\sigma}$ for homogeneous three-dimensional (3D) materials is a symmetric rank-2 tensor [19] (Table 1.1), which only contains 6 unique components. The 3D materials can be rotated to align the three principal axes with the x, y and z axes in Cartesian coordinate system, resulting in a diagonalized conductivity tensor with the number of unique components reduced to 3. If it is possible to know these principle axes in advance, one can align the

material principal axes with those of the characterization structure to reduce the number of independent measurements required.

Table 1.1. Conductivity tensors for 3D and 2D materials with principle crystalline axes unaligned and aligned with respect to the x, y, z-measurement axes, or aligned in the presence of a magnetic field $\boldsymbol{B}$. For 2D materials, the magnetic field direction is perpendicular to the plane $\boldsymbol{B} = B_z\hat{z}$.

	arbitrary axes	crystal axes	crystal axes with $\boldsymbol{B}$
3D	$\begin{bmatrix} \sigma_{xx} & \sigma_{xy} & \sigma_{xz} \\ \sigma_{xy} & \sigma_{yy} & \sigma_{yz} \\ \sigma_{xz} & \sigma_{yz} & \sigma_{zz} \end{bmatrix}$	$\begin{bmatrix} \sigma_{xx} & 0 & 0 \\ 0 & \sigma_{yy} & 0 \\ 0 & 0 & \sigma_{zz} \end{bmatrix}$	$\begin{bmatrix} \sigma_{xx} & -\sigma_{xy} & \sigma_{xz} \\ \sigma_{xy} & \sigma_{yy} & -\sigma_{yz} \\ -\sigma_{xz} & \sigma_{yz} & \sigma_{zz} \end{bmatrix}$
2D	$\begin{bmatrix} \sigma_{xx} & \sigma_{xy} \\ \sigma_{xy} & \sigma_{yy} \end{bmatrix}$	$\begin{bmatrix} \sigma_{xx} & 0 \\ 0 & \sigma_{yy} \end{bmatrix}$	$\begin{bmatrix} \sigma_{xx} & -\sigma_{xy} \\ \sigma_{xy} & \sigma_{yy} \end{bmatrix}$

A magnetic field $\boldsymbol{B}$ is usually applied to extract more information including the carrier density and mobility, which leads to asymmetric conductivity tensors in arbitrarily aligned materials. For 3D materials with measurement axes aligned to the principal crystal axes, the external $\boldsymbol{B}$ will induce purely anti-symmetric off-diagonal components (Table 1.1, last column). To reduce the complexity of the characterization, it is common practice to apply a magnetic field along one principal axis (*e.g.* $\boldsymbol{B} = B_z\hat{\boldsymbol{z}}$). In this case, all off-diagonal tensor components with Cartesian coordinates that include the magnetic field direction (σ_{xz} and σ_{yz}) become zero. In addition, many materials have planar symmetry which

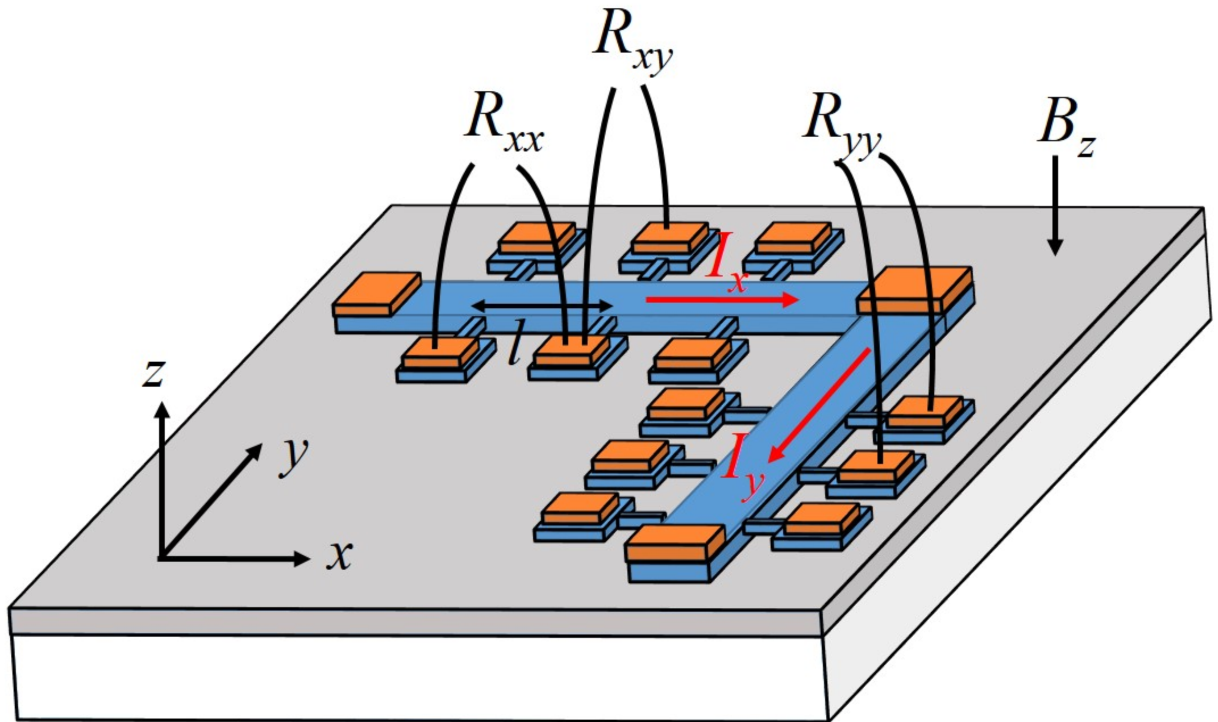

Figure 1.1. An L-shape Hall bar in the x-y plane in the presence of a magnetic field B_z. The current I_x and I_y are applied along the principal axis directions x and y, respectively. The longitudinal resistances along two directions R_{xx} and R_{yy} are measured with two voltage contacts along the bar, and the Hall resistance R_{xy} is measured with two voltage contacts across the bar.

we will define as the x-z plane, so that there are only two unique conductivity tensor components: $\sigma_{xx} = \sigma_{zz}$ and σ_{yy}. In such cases, the 3D conductivity tensor in the presence of a B-field can be reduced to a 2D tensor (Table 1.1, row "2D"), which enables the separate characterization of the three cross-sections parallel to the principal axes.

The most widely used method for measuring an anisotropic conductivity tensor is the Hall bar method. In this method, the material is cut into a bar-shaped sample along one principal axis (*e.g.* x) and a current I_x is applied through the current contacts at two

ends (Fig. 1.1). The longitudinal resistance R_{xx} is measured with two voltage contacts along the bar with a separation l and the Hall resistance R_{xy} is measured with two voltage contacts across the bar under an external magnetic field B_z. Two resistivity components can be extracted from the measured resistances: $\rho_{xx} = R_{xx}A/l$ and $\rho_{xy} = R_{xy}d$, whereby A and d are the bar cross-section area and thickness, respectively. The 2D conductivity tensor can be obtained by inverting the resistivity tensor ($\boldsymbol{\sigma} = \boldsymbol{\rho}^{-1}$). To extract the full 3D tensor, at least three Hall bars are needed for 3D aligned materials, and at least two Hall bars are required for 2D materials. Two orthogonally oriented Hall bars can be combined into an L-shaped Hall bar, as shown in Fig. 1.1. The Hall bar method is known to potentially be imprecise due to the difficulty of accurately measuring the geometric factor l/A [**20**].

Alternatively, methods using planar samples may be adapted to extract the tensor components for 2D or 3D materials. One such method is the van der Pauw (vdP) method [**21**, **22**], which is extensively used in electrical characterization. This method accepts planar samples of arbitrary shape and uses four point-like contacts on the sample periphery. For anisotropic samples, additional requirements are posed on the sample geometry and enough information can be obtained to extract the full in-plane conductivity tensor. The literature on vdP method for anisotropic materials are limited, and most studies use rectangular samples with principal axes aligned with the rectangle edges [**23**, **24**] or with non-standard measurement geometries [**25**–**27**]. Recently the anisotropic vdP method has been extended to parallelogram shaped samples with both known or unknown principal axis orientation [**28**]. To extract the full tensor, the anisotropic vdP

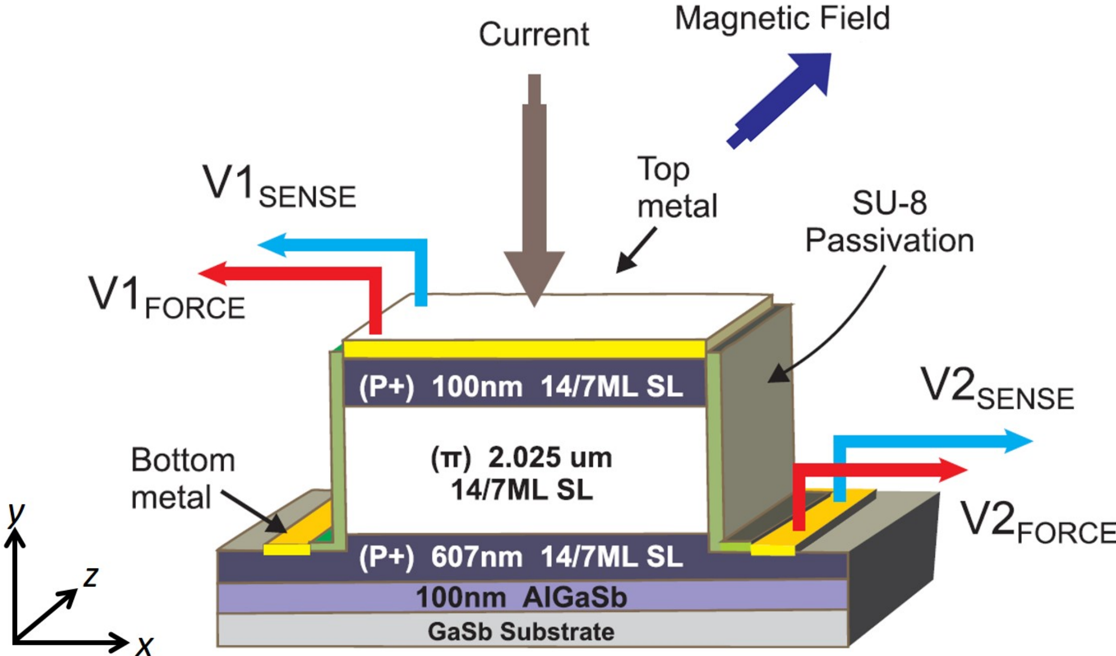

Figure 1.2. Vertical magnetoresistance measurement setup for p-type InAs/GaSb type-II superlattices by Umana-Membreno *et al.* [1]. This measurement method is only able to extract the longitudinal component of the resistivity tensor ρ_{yy} and the other two components ρ_{xx} and ρ_{xy} are missing, which reduces the reliability and accuracy of the extraction of the conductivity tensor, carrier density, and mobilities.

method requires three samples for 3D aligned materials, but only one sample for 2D materials. Also, the accuracy is higher than the Hall bar method since the measurement geometry-induced error is much smaller.

While the conductivity tensor for bulk anisotropic conductors can be characterized with the Hall bar method and the van der Pauw method, the characterization of anisotropic thin films is much more challenging, for both in-plane and cross-plane anisotropic conductivities. The primary obstacle to the in-plane conductivity characterization is the parallel

conduction of the substrate. For anisotropic thin films grown on top of a conductive substrate, *e.g.* the active layer of optical devices [29], the highly conductive substrate will short-circuit any standard in-plane transport characterization that one might attempt at macroscopic scales. Current in-plane transport characterization of such structures either requires additional effort in removing the bottom conductive layer with precise mechanical or chemical approaches [30], low temperatures whereby the bottom conductive layer freezes out [31], or fabrication of the anisotropic thin film on another insulating substrate, whereby the transport properties can be different from the native performance in the original device due to lattice mismatch.

The cross-plane conductivity tensor characterization for anisotropic thin films is even more challenging than the in-plane direction. The film thickness is typically too small to allow any patterning in the vertical direction, as would be required to implement any of the characterization methods above. Unfortunately, in practice, there are many electronic and optoelectronic devices with exactly this sort of anisotropic layer, typically a superlattice, such as for photodetectors [32,33], lasers [34,35], and transistors [36]. One technique has been previously proposed to characterize the vertical transport properties of these materials, using a vertical "bar" structure as shown in Fig. 1.2 [1]. However, in such a structure only the longitudinal component of the resistivity tensor $\rho_{yy}(B)$ can be extracted from the magneto-resistance measurement, the Hall voltage is short-circuited by the facet contacts on top and bottom; thus no information about the off-diagonal tensor components can be extracted. The lack of the off-diagonal components of the conductivity tensor reduces the reliability and accuracy of the calculation, and eliminates the possibility of deducing other important transport parameters such as mobility and

carrier density. Thus a novel method that can characterize both the in-plane and cross-plane conductivities of an anisotropic thin film conductor atop a conductive substrate is highly desirable, as will be introduced in Chapter 2 – the triple stripline method.

1.2. Synthesis of anisotropic conductors

Strictly speaking, any materials with an asymmetric electronic structure are anisotropic conductors. According to the asymmetry and the resulting conductivity anisotropy directions, we divide anisotropic conductors into three categories: homogeneous crystals, anisotropic conductive film (ACF) and aligned nanostructures. The synthesis methods will be discussed for each category, respectively.

Homogeneous crystals with a planar structure typically exhibit high conductivity in-plane and low conductivity cross-plane. One familiar example is copper oxide superconductor compound, which has highly anisotropic conductivity above T_c [37]. Yttrium barium cuprate, $YBa_2Cu_3O_{6+x}$, for example, has planar copper oxide layers separated by barium and yttrium ions [2] (Fig. 1.3a). The electrical conductivity is much higher parallel to the conducting Cu-O bonds than in the perpendicular direction. Similar planar structure can be found in non-stoichiometric rutile TiO_{2-x} [38], intermetallic compounds $TaS_2C_5H_5N$ [39], and silicide $ReSi_{1.75}$ [40]. Crystals with heterostructures such as superlattices are not as prominently discussed since the cross-plane conductivity is rarely measured. The synthesis method for the layered homogeneous crystals will depend on the specific crystal growth technique.

Anisotropic conductive films (ACF), also known as z-axis ACF, are an example of how an anisotropic composite material has important technological relevance. ACF's

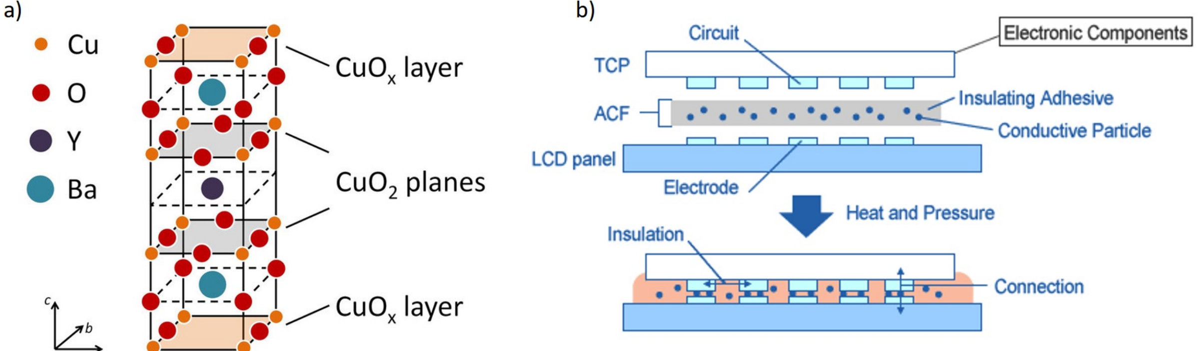

Figure 1.3. (a) The crystal structure of $YBa_2Cu_3O_{6+x}$ showing the conducting Cu-O layers perpendicular to the c-axis. Figure reproduced from Ref. [2]. (b) Application of anisotropic conductive film (ACF) for circuitry connection [3].

are electrically conducting in the cross-plane direction but insulating in the other two in-plane directions [3]. An ACF is typically an insulating polymer-matrix containing conducting particles that can form cross-plane conducting paths. These particles are randomly dispersed in the film but are in low enough concentration that they do not form conducting paths in the in-plane direction, as shown in Fig. 1.3(b). The polymer matrix is typically chosen to be an elastomer (such as silicone) or a thermoplast (such as polyimidesiloxane or seflon) to provide resilience, so the ACF can be reusable [41]. Metal wires [42], metal columns [43], and individual metal coated polymer particles [44] have been used as the conducting particles. After bonding under heat and pressure, the vertical distance between the top and bottom electrodes becomes smaller than or comparable to the particle diameter, forming the cross-plane conducting paths.

The last and most interesting category of anisotropic conductors is aligned nanostructures, which normally have higher conductivity in the alignment direction, and lower

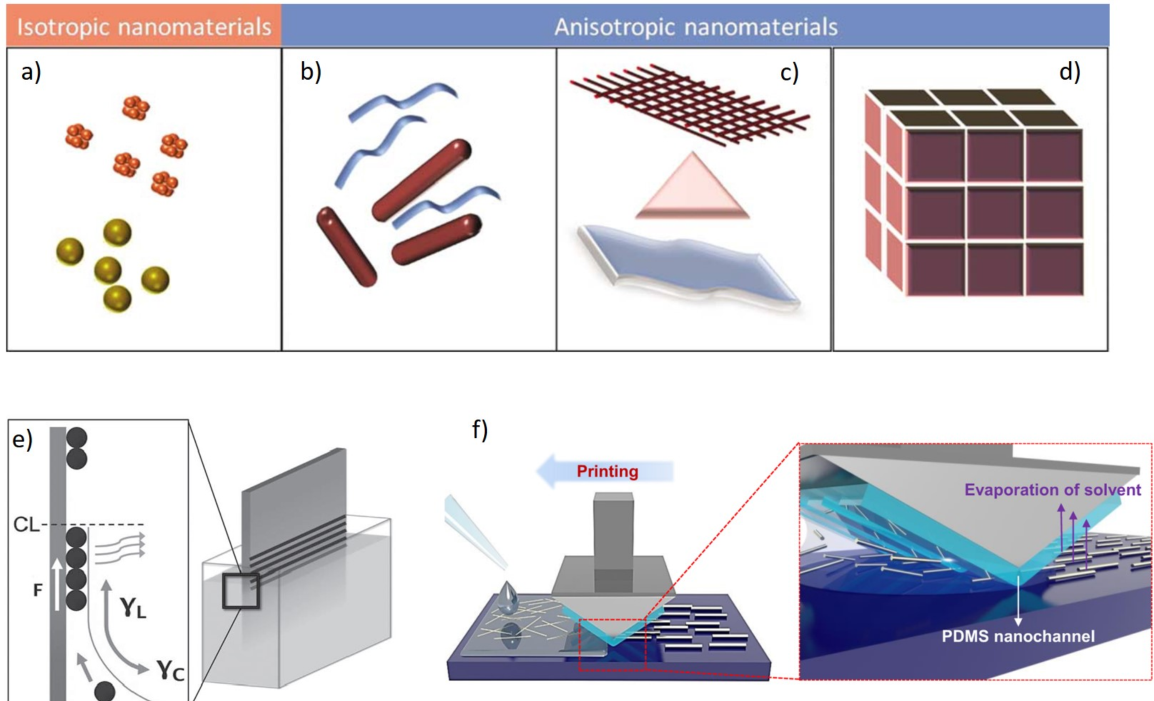

Figure 1.4. (a) Isotropic nanomaterials: 0D spheres and clusters and Anisotropic nanomaterials: (b) 1D nanofibers, wires, and rods, (c) 2D films, plates, and networks, and (d) 3D nanomaterials (reproduced from Ref. [4]). (e) Schematic showing the slip-stick behavior of evaporation-driven self-assembly (EDSA), reproduced from Ref. [5]. (f) Schematic of the capillary printing process using a nano-patterned PDMS stamp to produce highly aligned Ag nanowire arrays, reproduced from Ref. [6].

conductivity in the orthogonal direction. With an in-plane alignment direction, an in-plane conductivity anisotropy can be realized, which is not achievable in the previous two categories. Nanomaterials can present isotropic or anisotropic physical and chemical properties depending on the shape of the nanostructure, as categorized in Fig. 1.4 based on the dimensionality [4]. To develop macroscopic anisotropic properties, a number of self-assembly methods have been studied for aligning the anisotropic nanostructures, including spin coating [45], Langmuir-Blodgett assembly [46], dielectrophoresis [47], blown-bubble

assembly [16], and DNA-linker-induced surface assembly [48]. However, most of these approaches are limited in the material density and coverage area. To achieve large-area, high-density anisotropic nanomaterial thin-film, high-throughput self-assembly methods would be particularly interesting, such as the evaporation-driven self-assembly (EDSA) method [5], which aligns the 1D nanowires into stripes parallel to the solution/substrate interface during evaporation (Fig. 1.4e), and the capillary printing technique [6], which "drags and prints" nanowire arrays along the channels (Fig. 1.4f).

While the synthesis of conductors with cross-plane anisotropic conductivity, *e.g.* the layered crystal and ACF, has been well studied, creation of the in-plane conductivity anisotropy is not well-studied. In chapter 3, we demonstrate the synthesis of anisotropic semiconductor thin films with artificial in-plane conductivity anisotropy, including the carbon nanotube (CNT) film aligned using EDSA, the 3D-printed graphene-polymer film, and finally the AlGaAs thin film with ion-implantation isolated channels. With the synthesis techniques used, both n- and p-type in-plane anisotropic conductivities in controlled orientation can be achieved, which opens up applications involving multiple anisotropically conducting layers.

1.3. Application of anisotropic conductors

Anisotropic conductors have extensive applications in electronics, optics and thermoelectrics. ACF is widely used for interconnection in electronic packaging (chip-to-package, package-to-board and board-to-board) in liquid display manufacturing [49]. Superlattices (SLs) such as InAs/(In,Ga)Sb [32–34], InAs/$InAs_{1-x}Sb_x$ [29, 50] and GaAs/AlGaAs

SLs [51] have been widely used in photodetectors and quantum cascade lasers. Low-dimensional nanostructures such as PbSe-PbTe quantum dots [52], $Si_{1-x}Ge_x$ nanowires [53], and Bi_2Te_3 superlattices [54] have been reported to have superior thermoelectric performance compared with the bulk materials.

In addition to the conventional thermoelectrics mentioned above, we have identified a novel paradigm in thermoelectrics, *i.e.*, the $p \times n$-type transverse thermoelectrics, whereby orthogonally aligned p and n-type anisotropic conduction in a system can generate a heat flow transverse to the electrical current. This opens up new applications for anisotropic conductors, as will be introduced in Chapter 4.

1.4. Thesis outline

This dissertation studies novel directions in the electrical characterization, synthesis, and application of anisotropic semiconducting thin films. Chapter 2 proposes a new method to simultaneously characterize the in-plane and cross-plane electrical conductivity of anisotropic thin films with a "triple stripline" device structure. The motivation and complete theory behind the method will be presented as well as the preliminary progress towards an experimental demonstration. Chapter 3 shows the synthesis of three artificial thin film semiconductors with anisotropic in-plane electrical conductivities, including aligned carbon nanotube stripes, 3D-printed graphene-polymer stripes and ion implantation isolated AlGaAs stripes. Chapter 4 introduces $p \times n$-type transverse thermoelectrics, a novel paradigm of transverse thermoelectrics that is a potential application of anisotropic semiconductors, as well as introducing the "cross-hatched" artificial approach to fabricating $p \times n$-type structures.

CHAPTER 2

Triple stripline method: characterizing conductivity of anisotropic thin films

In this chapter, we propose a new method to characterize the in-plane and cross-plane electrical conductivity of anisotropic semiconductor thin films with a "triple stripline" device structure. The motivation and complete theory behind the method will be presented here as well as the preliminary progress towards an experimental demonstration. Section 2.1 considers the electrostatic potential caused by a single stripline contact to an anisotropic thin film conductor, based on the generic structure of optical devices which have a grounding back-plane, and proposes a closed analytical form for the potential. However, since this closed form has no analytical solution, Section 2.2 provides a numerical alternative solution to the potential distribution. Section 2.3 adds two more voltage-contact striplines to the single current-contact stripline to create the full triple stripline device structure, and considers the experimental potential measurements that can uniquely determine all components of the conductivity tensor. Finally Section 2.4 describes the progress thus far towards realizing the triple stripline device.

2.1. Magnetotransport potentional distribution in anisotropic thin films: Analytical description of the problem

In this section, we identify the appropriate geometry to study the conductivity tensor of anisotropic thin films and identify useful coordinate transformations for describing this

problem. Optical devices such as IR detectors and emitters typically have a bottom doped contact, a central undoped active layer and a top doped contact [29] (Fig. 2.1a). The layer of interest is the anisotropically resistive active layer atop the highly conductive bottom contact layer, as shown in Fig. 2.1(b). By etching away the top doped contact layer, and depositing a narrow metal strip as a top contact, the standard device structure can be readily modified into the geometry under study. Note that this model requires that the stripline contact width D is significantly narrower than the thickness of the active layer t, as shown in Fig. 2.1(b) above. The active layer of interest is assumed to have a width much larger than its thickness t, to minimize edge current effects. For simplicity, we therefore assume the active layer width to be infinite. The work in this section is published has been SPIE conference proceedings [55].

From the discussion in Section 1.1, the anisotropic conductivity tensor in the presence of a magnetic field can be represented by a two-dimensional (2D) tensor since the thin-film is isotropic in-plane:

$$\boldsymbol{\sigma} = \begin{bmatrix} \sigma_{xx} & \sigma_{xy} \\ -\sigma_{xy} & \sigma_{yy} \end{bmatrix}. \tag{2.1}$$

Here the x-axis is the in-plane direction, and the y-axis is the cross-plane direction. The anisotropy ratio is defined as $A = \sigma_{yy}/\sigma_{xx}$. And the 2D anisotropic conductivity tensor is fully described with the three independent components σ_{xx}, σ_{yy} and σ_{xy}. It has to be noted that even within the simple Drude model each component will depend on the magnetic field (B), with more complicated B-field dependence arising, for example, from contributions from multiple carrier species in multi-carrier materials. For simplicity, this

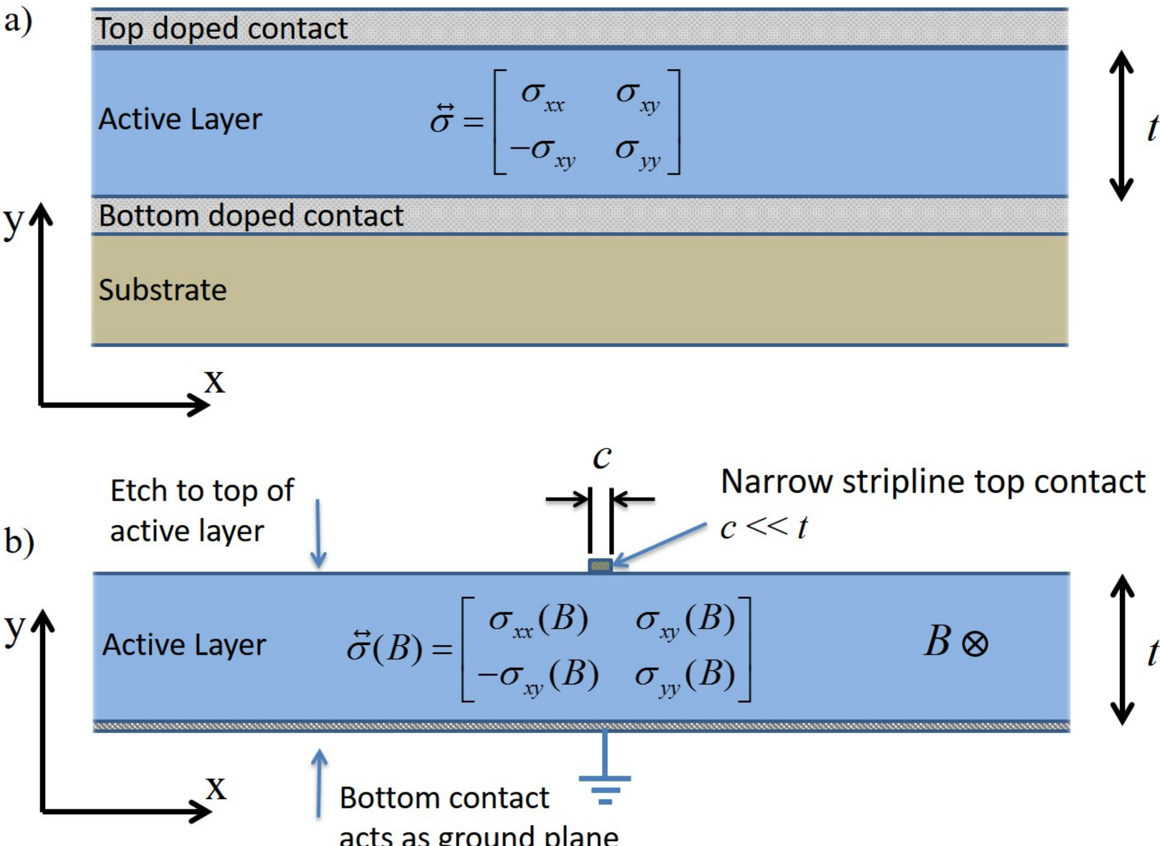

Figure 2.1. (a) The typical structure of optical device layers, with an active layer sitting between two highly conductive top- and bottom-contacts. (b) The proposed single stripline diagnostic structure. The top conducting layer is etched away, and the bottom conducting layer is used as a ground plane. One narrow contact stripline is deposited on the top of the active layer. The electromagnetic potential distribution of this structure will be calculated as a first step towards developing a measurement method of the full conductivity tensor.

chapter will concern itself strictly with the potentials that result from a given conductivity tensor at a fixed B-field.

We will now solve for the electrostatic potential of the proposed single-stripline diagnostic structure, using mixed Dirichlet and Neumann boundary conditions for the bottom and top surfaces of the layer of interest. The potential and current distribution of the diagnostic structure in galvanomagnetic phenomena is governed by the steady-state Laplace equation with corresponding boundary conditions. The Laplace equation has the same form with or without a magnetic field due to the anti-symmetry of the off-diagonal terms of the conductivity tensor:

$$\nabla \cdot (\boldsymbol{\sigma} \cdot \nabla \varphi) = \sigma_{xx} \frac{\partial^2 \varphi}{\partial x^2} + \sigma_{yy} \frac{\partial^2 \varphi}{\partial y^2} = 0, \tag{2.2}$$

where φ is the electric potential and the current density is $\boldsymbol{j} = -\boldsymbol{\sigma} \cdot \nabla \varphi$. The structure is modeled as a 2D infinite strip within $-\infty < x < +\infty$, $0 \leq y \leq t$. Part of its boundary satisfies Dirichlet boundary conditions where the potential is fixed to zero at the bottom grounding plane and set to the applied voltage V at the central stripline on the top plane:

$$\varphi = 0|_{y=0}, \quad \varphi|_{x=0,y=t} = V. \tag{2.3}$$

Neumann boundary conditions can be defined for the remaining part of the strip boundary where the current density perpendicular to the boundary is either zero or fixed value $I\delta(x)$ at the top stripline.

$$j_y = -\left(-\sigma_{xy} \frac{\partial \varphi}{\partial x} + \sigma_{yy} \frac{\partial \varphi}{\partial y}\right)|_{y=t} = I\delta(x) \tag{2.4}$$

Here I is the total current resulting from the voltage V applied on the top stripline. For simplicity we consider the stripline to have zero-width ($c \to 0$) since its width is

much smaller than the film thickness ($c \ll t$). According to the σ_{xy} term for the Neumann boundary conditions in Eq. (2.4), we see that although the Dirichlet condition does not change with the magnetic field, the Neumann condition *will* change under different magnetic field strengths and result in different potential distributions.

Fourier transforms are utilized to analytically solve the boundary value problem (BVP) defined by Eqs. (2.2)-(2.4). The Fourier transform has several forms, here we use the unitary form with angular frequency $\hat{\varphi}(\xi) = \frac{1}{\sqrt{2\pi}} \int\limits_{-\infty}^{+\infty} \varphi(x) e^{-i\xi x} dx$ and the inverse transform $\varphi(x) = \frac{1}{\sqrt{2\pi}} \int\limits_{-\infty}^{+\infty} \hat{\varphi}(\xi) e^{+i\xi x} d\xi$. Making partial Fourier transform for Eqs. (2.2)-(2.4) with $x \to \xi$ (so $\varphi(x, y) \mapsto \hat{\varphi}(\xi, y)$), we arrive at the modified differential equation:

$$\sigma_{xx}(-\xi^2)\hat{\varphi} + \sigma_{yy}\frac{\partial^2 \hat{\varphi}}{\partial y^2} = 0, \tag{2.5}$$

with boundary conditions:

$$\hat{\varphi}\,|_{y=0} = 0 \tag{2.6}$$

at the bottom surface, and

$$\left(-\sigma_{xy}(+i\xi)\hat{\varphi} + \sigma_{yy}\frac{\partial \hat{\varphi}}{\partial y}\right)\bigg|_{y=L} = \frac{I}{\sqrt{2\pi}} \tag{2.7}$$

at the top.

The solution of potential distribution $\hat{\varphi}(\xi, y)$ to Eqs. (2.5)-(2.7) has the form:

$$\hat{\varphi}(\xi, y) = A(\xi)e^{+\gamma\xi y} + B(\xi)e^{-\gamma\xi y}, \tag{2.8}$$

whereby $\gamma = \sqrt{\frac{\sigma_{xx}}{\sigma_{yy}}}$. The fact that $\varphi(x, y)$ is purely real requires $\hat{\varphi}(\xi, y) = \hat{\varphi}^*(-\xi, y)$. Then the Dirichlet boundary condition Eq. 2.6 yields $A(\xi) = B(-\xi)$. Thus the solution in the Fourier regime (Eq. 2.8)) can be rewritten as:

$$\hat{\varphi}(\xi, y) = A(\xi)(e^{+\gamma\xi y} - e^{-\gamma\xi y}) = 2A(\xi)\sinh(\gamma\xi y). \tag{2.9}$$

Since $\hat{\varphi}(\xi, y) = \hat{\varphi}^*(-\xi, y)$, the coefficient $A(\xi)$ needs to satisfy:

$$A^*(\xi) = -A(-\xi). \tag{2.10}$$

Substituting Eq. (2.9) into the Neumann boundary condition Eq. (2.7), we can solve for the parameter $A(\xi)$:

$$A(\xi) = \frac{I}{\sqrt{2\pi}} \frac{1/2\xi}{-i\sigma_{xy} sinh(\gamma\xi L) + \sigma_{yy}\gamma cosh(\gamma\xi L)}, \tag{2.11}$$

which is verified to satisfy the requirement defined by Eq. (2.10). So the complete form of the potential distribution in the Fourier regime can be derived as:

$$\hat{\varphi}(\xi, y) = \frac{I}{\sqrt{2\pi}} \frac{\sinh(\gamma\xi y)}{-i\sigma_{xy}\xi\sinh(\gamma\xi L) + \sigma_{yy}\gamma\xi\cosh(\gamma\xi L)} \tag{2.12}$$

The potential distribution in the real regime $\varphi(x, y)$ can be obtained by applying the inverse Fourier transform to the $\hat{\varphi}(\xi, y)$. Defining parameters $A = \frac{I}{\sqrt{2\pi}\sigma_{xy}}$, $a = \gamma y$, $b = \gamma\frac{\sigma_{yy}}{\sigma_{xy}}$, $c = \gamma L$, Eq. (2.12) can be rewritten as:

$$\hat{\varphi}(\xi, y) = \frac{A}{b^2} \frac{\sinh(a\xi)\,(b\cosh(c\xi) + i\sinh(c\xi))}{\xi(1 + B\sinh^2(c\xi))}, \text{ whereby } \left(B = \frac{b^2+1}{b^2} = 1 + \frac{\sigma_{xx}}{\sigma_{yy}}\right). \tag{2.13}$$

The inverse Fourier transform of $\hat{\varphi}(\xi, y)$ can be simplified as:

(2.14)

$$\begin{aligned}
\varphi(x,y) &= \tfrac{1}{\sqrt{2\pi}} \int_{-\infty}^{+\infty} \hat{\varphi}(\xi,y) e^{+i\xi x} d\xi \\
&= \tfrac{1}{\sqrt{2\pi}} \int_{0}^{+\infty} \hat{\varphi}(\xi,y) e^{+i\xi x} d\xi + \tfrac{1}{\sqrt{2\pi}} \int_{-\infty}^{0} \hat{\varphi}(\xi,y) e^{+i\xi x} d\xi \\
&= \tfrac{1}{\sqrt{2\pi}} \int_{0}^{+\infty} \hat{\varphi}(\xi,y) e^{+i\xi x} d\xi + \tfrac{1}{\sqrt{2\pi}} \int_{0}^{+\infty} \hat{\varphi}(-\xi,y) e^{-i\xi x} d\xi \\
&= \tfrac{1}{\sqrt{2\pi}} \int_{0}^{+\infty} (\hat{\varphi}(\xi,y) + \hat{\varphi}(-\xi,y)) \cos(\xi x) + i(\hat{\varphi}(\xi,y) - \hat{\varphi}(-\xi,y)) \sin(\xi x)) d\xi \\
&= \tfrac{1}{\sqrt{2\pi}} \tfrac{2A}{b^2} \int_{0}^{+\infty} d\xi \tfrac{\sinh(a\xi)}{\xi\left(1+B\sinh^2(c\xi)\right)} \left[b\cosh(c\xi)\cos(\xi x) + \sinh(c\xi)\sin(\xi x)\right]
\end{aligned}$$

So the analytical solution of the potential distribution $\varphi(x, y)$ can be expressed in the integral form:

$$\varphi(x,y) = \frac{1}{\sqrt{2\pi}} \frac{2A}{b^2} \int_{0}^{+\infty} d\xi \frac{\sinh(a\xi)}{\xi\left(1+B\sinh^2(c\xi)\right)} \left[b\cosh(c\xi)\cos(\xi x) + \sinh(c\xi)\sin(\xi x)\right] \quad (2.15)$$

Recalling that a, b, and c all depend on y the final expression becomes:

$$\begin{aligned}
\varphi(x,y) = \tfrac{1}{\pi} \tfrac{\sigma_{xx}}{\sigma_{yy}\sigma_{xy}} \int_{0}^{+\infty} & d\xi \tfrac{\sinh(\sqrt{\frac{\sigma_{xx}}{\sigma_{yy}}} y\xi)}{\xi\left(1+\left(1+\frac{\sigma_{xx}}{\sigma_{yy}}\right)\sinh^2(\sqrt{\frac{\sigma_{xx}}{\sigma_{yy}}} L\xi)\right)} \cdot \\
& \left[\sqrt{\tfrac{\sigma_{yy}}{\sigma_{xx}}} \cosh(\sqrt{\tfrac{\sigma_{xx}}{\sigma_{yy}}} L\xi) \cos(x\xi) + \sinh(\sqrt{\tfrac{\sigma_{xx}}{\sigma_{yy}}} L\xi) \sin(x\xi)\right] .
\end{aligned} \quad (2.16)$$

Equation (2.16), however, has no analytical solution. that there exists no straightforward analytical solution of the potential distribution. It may be appropriate to calculate the infinite integral of Eq. (2.16) numerically for one or two points of interest, however this infinite integral would require a significant amount of time to numerically calculate

an array of points in the $x - y$ plane. Further study shows that there is a more elegant numerical approach to solve for the potential distribution throughout the volume of the anisotropic layer, which involves linear coordinate transformation and finite element method simulation, described below.

2.2. Magnetotransport potentional distribution in anisotropic thin films: Numerical solution

The numerical solution to the potential distribution in the anisotropic thin films requires a different strategic approach than the analytical solution of the previous section. Whereas Hall voltages and resistances of finite 2D structures can be numerically calculated using boundary element methods [56], finite difference [57, 58] or finite element method (FEM) [59, 60], all these numerical methods require a finite calculating area, and the majority demonstrated results only on isotropic materials. To solve the present problem of an anisotropic conductor with infinite lateral dimension, we propose to use linear coordinate transformations to simplify the problem, including a scaling transformation to transform the problem of an infinite anisotropically conducting strip into an isotropic one, and then two conformal maps to transform the infinite isotropic strip into a finite rectangle, which is suitable for numerical calculation. Once these transforms are identified, the problem of the infinitely wide strip can be solved by inverting this same set of the transforms. The work in this section is published has been SPIE conference proceedings [55].

2.2.1. Coordinate transformation: scaling transformations and conformal maps

The boundary condition problem describing the potential $\varphi(x, y)$ for the anisotropic infinite strip (Eq. (2.2)-(2.4)) can be transformed into an equivalent problem in another 2D coordinate system with potential distribution $\varphi'(x', y')$ for an isotropic rectangle. There are two conditions that need to be satisfied for the transformation to preserve the Laplace equation and the boundary conditions. Analogous to the treatment of anisotropic media under zero magnetic field in Ref. [**26**], we require two conditions:

I) $\varphi(x, y) = \varphi'(x', y')$.

II) The net current flowing through any segment $\Delta\boldsymbol{L} = (\Delta x, \Delta y)$ and its image $\Delta\boldsymbol{L'} = (\Delta x', \Delta y')$ must be the same.

Condition I guarantees the potential remains the same on the transformed Dirichlet boundaries. Condition II preserves the current flowing through the Neumann boundaries and the divergence of the current density, so the Laplace equation is still satisfied. These two conditions also ensure that any resistance R is transformed to an identical resistance $R' = R$ in the primed frame.

Scaling transformation: anisotropic to isotropic infinite strip

A non-conformal scaling transformation is required to transform the anisotropic conductivity tensor into an isotropic form. The transformation has been solved for three-dimensional (3D) form by van der Pauw [**22**], but here we explicitly solve for the 2D simpler form. Suppose we perform a linear transformation $x' = \alpha x$, $y' = \beta y$ so that $\varphi(x, y) = \varphi'(x', y')$. This scaling transformation is linear, but it is non-conformal since it does not preserve the local angles in the transformation. The electric field in the new 2D

coordinate system is:

$$E'_x = -\frac{\partial\varphi'}{\partial x'} = -\frac{1}{\alpha}\frac{\partial\varphi}{\partial x} = \frac{1}{\alpha}E_x$$
$$E'_y = -\frac{\partial\varphi'}{\partial y'} = -\frac{1}{\beta}\frac{\partial\varphi}{\partial y} = \frac{1}{\beta}E_y \quad (2.17)$$

Condition II requires that:

$$j'_x dy' = j_x dy \;\Rightarrow\; j'_x = \frac{1}{\beta}j_x$$
$$j'_y dx' = j_y dx \;\Rightarrow\; j'_y = \frac{1}{\alpha}j_y. \quad (2.18)$$

Since $\boldsymbol{j} = \boldsymbol{\sigma}\cdot(-\nabla\varphi)$, Eq. (2.17) and (4.1) lead to:

$$\boldsymbol{j'} = \begin{bmatrix} j'_x \\ j'_y \end{bmatrix} = \begin{bmatrix} \frac{\alpha}{\beta}\sigma_{xx} & \sigma_{xy} \\ -\sigma_{xy} & \frac{\beta}{\alpha}\sigma_{yy} \end{bmatrix}\begin{bmatrix} E'_x \\ E'_y \end{bmatrix} = \boldsymbol{\sigma'}\cdot\boldsymbol{E'} \quad (2.19)$$

When $\frac{\alpha}{\beta} = \left(\frac{\sigma_{yy}}{\sigma_{xx}}\right)^{1/2} = A^{1/2}$, $\boldsymbol{\sigma'}$ reduces to an isotropic conductivity tensor:

$$\boldsymbol{\sigma'} = \begin{bmatrix} \sigma_m & \sigma_{xy} \\ -\sigma_{xy} & \sigma_m \end{bmatrix}, \quad (2.20)$$

where $\sigma_m = (\sigma_{xx}\sigma_{yy})^{1/2}$. Here we adopt $\alpha = A^{1/2}\frac{\pi}{2}\frac{1}{t}$ and $\beta = \frac{\pi}{2}\frac{1}{t}$, to map the anisotropic infinite strip described in Section 2.1 into an isotropic infinite strip within $-\infty < x' < \infty$, $0 < y' < \frac{\pi}{2}$, for convenience in the subsequent conformal mapping.

It has to be noted this transformation is not the only non-conformal mapping that can transform the 2D anisotropic conductivity tensor into an isotropic form. The 2D linear transformation can be represented by the transformation matrix $\boldsymbol{T} = \begin{bmatrix} T_{11} & T_{12} \\ T_{21} & T_{22} \end{bmatrix}$ so

that $\begin{bmatrix} x' \\ y' \end{bmatrix} = \boldsymbol{T} \cdot \begin{bmatrix} x \\ y \end{bmatrix}$. It can be proven that any 2D linear transformation that has :

$$\frac{T_{11}^2 + T_{21}^2}{T_{12}^2 + T_{22}^2} = \frac{\sigma_{yy}}{\sigma_{xx}}, \quad T_{11}T_{12} + T_{21}T_{22} = 0 \tag{2.21}$$

can transform the boundary condition problem into an coordinate system in which the conductivity tensor is isotropic, as long as $\boldsymbol{T} \neq \boldsymbol{0}$.

Conformal map: infinite strip to finite rectangle

Although the conductivity tensor in the transformed frame is now isotropic, the numerical solution would still require an infinite mesh. We will use conformal mapping to transform the problem to a finite-sized mesh that can be solved efficiently with the finite element method (FEM). In this case, we will conformally map the infinitely wide stripe in the (x', y') coordinate system to a finite rectangle in the (u, v) coordinate system, in which the potential distribution can be calculated with FEM simulation. A conformal map is a linear transformation that preserves local angles and can be used to transform open-boundary shapes (*e.g.* infinite strip) to closed shapes [61], which is convenient for solving harmonic functions over a planar domain since the image functions are also harmonic. To simplify the mathematical representation, we use complex coordinates $z' = x' + iy'$ and $w = u + iv$ to represent the coordinates in the origin and final coordinate systems, respectively, and we use analytical functions of the complex coordinates to describe the conformal transformations.

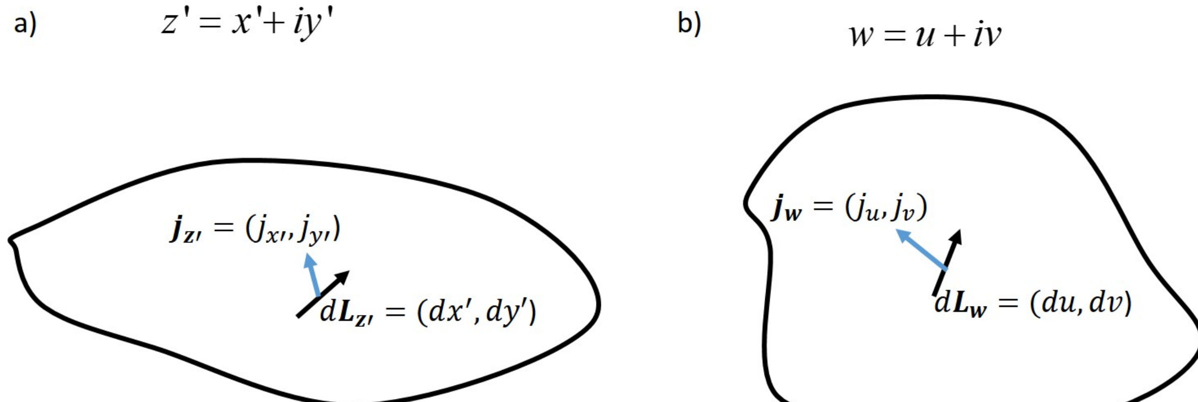

Figure 2.2. Calculation of the amount of current flowing through the elementary segment before and after the conformal map. The isotropic z'-plane is conformally mapped into the w-plane, whereby the elementary segment $d\boldsymbol{L_{z'}}$ and the current density $\boldsymbol{j_{z'}}$ that passes it are transformed to $d\boldsymbol{L_w}$ and $\boldsymbol{j_w}$, respectively. The total amount of current flowing through $d\boldsymbol{L_{z'}}$ and $d\boldsymbol{L_w}$ should be identical.

Before we apply any conformal maps to further simplify the boundary condition problem in the (x', y') coordinate system, we need first prove that the anti-symmetric conductivity tensor $\boldsymbol{\sigma}'$ in the primed frame remains invariant under conformal transformation to satisfy conditions I and II mentioned above. Suppose there is a conformal map from the z'-plane (x', y') to the w-plane (u, v) so that $\varphi'(x', y') = \phi(u, v)$ (Fig. 2.2). The conformal map requires:

$$u_{x'} = \frac{\partial u}{\partial x'} = \frac{\partial v}{\partial y'} = v_{y'},\; u_{y'} = \frac{\partial u}{\partial y'} = -\frac{\partial v}{\partial x'} = -v_{x'}. \tag{2.22}$$

Here we adopt the notation $u_{x'}$ to represent the partial derivative of u with respect to x'. The current flowing through the segment $d\boldsymbol{L_{z'}} = (dx', dy')$ in z'-plane and its image

$d\boldsymbol{L_w} = (du, dv)$ in w-plane are :

$$
\begin{aligned}
dI_{z'} &= |\boldsymbol{j_{z'}} \times d\boldsymbol{L_{z'}}| = j_{y'}dx' - j_{x'}dy' \\
dI_w &= |\boldsymbol{j_w} \times d\boldsymbol{L_w}| = j_v du - j_u dv = (j_v u_{x'} - j_u v_{x'})dx' - (-j_v u_{y'} + j_u v_{y'})dy',
\end{aligned}
$$

respectively. From $dI_{z'} = dI_w$ and using the conformal relations of Eq. (2.22) we can determine the tensor $\boldsymbol{m}$:

$$
\boldsymbol{j_{z'}} = \begin{bmatrix} j_{x'} \\ j_{y'} \end{bmatrix} = \begin{bmatrix} v_{y'} & -u_{y'} \\ -v_{x'} & u_{x'} \end{bmatrix} \begin{bmatrix} j_u \\ j_v \end{bmatrix} = \begin{bmatrix} u_{x'} & -u_{y'} \\ u_{y'} & u_{x'} \end{bmatrix} \boldsymbol{j_w} = \boldsymbol{m j_w}. \tag{2.23}
$$

According to the definition of conductivity tensors, $\boldsymbol{j_{z'}} = \boldsymbol{\sigma'}(-\nabla_z \varphi')$, $\boldsymbol{j_w} = \boldsymbol{\sigma_w}(-\nabla_w \phi)$. From

$$
\nabla_z \varphi' = \begin{bmatrix} \frac{\partial \varphi'}{\partial x'} \\ \frac{\partial \varphi'}{\partial y'} \end{bmatrix} = \begin{bmatrix} u_{x'} & v_{x'} \\ u_{y'} & v_{y'} \end{bmatrix} \begin{bmatrix} \frac{\partial \phi}{\partial u} \\ \frac{\partial \phi}{\partial v} \end{bmatrix} = \begin{bmatrix} u_{x'} & -u_{y'} \\ u_{y'} & u_{x'} \end{bmatrix} \nabla_w \phi = \boldsymbol{m} \nabla_w \phi, \tag{2.24}
$$

we can identify the conductivity tensor in the w-plane:

$$
\boldsymbol{\sigma_w} = (\boldsymbol{m})^{-1} \boldsymbol{\sigma' m} = \frac{1}{u_{x'}^2 + u_{y'}^2} \begin{bmatrix} u_{x'} & u_{y'} \\ -u_{y'} & u_{x'} \end{bmatrix} \begin{bmatrix} \sigma_m & \sigma_{xy} \\ -\sigma_{xy} & \sigma_m \end{bmatrix} \begin{bmatrix} u_{x'} & -u_{y'} \\ u_{y'} & u_{x'} \end{bmatrix} = \boldsymbol{\sigma'}. \tag{2.25}
$$

As a result, we have shown that the anti-symmetric conductivity tensor remains the same after the conformal mapping from the z'-plane to w-plane. This significant result enables us to apply any conformal map that simplifies the geometry of the infinite isotropic strip from Section 2.2.1 to a finite shape that can be simulated numerically.

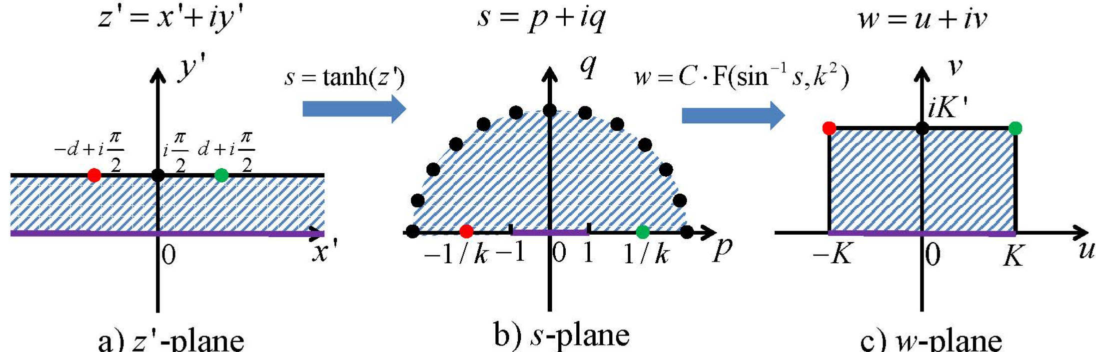

Figure 2.3. The conformal maps transforming the infinite strip from (a) z'-plane to (b) upper half s-plane, to (c) a finite rectangle in the w-plane. The purple line in all three plots represents the Dirichlet boundary at fixed ground potential, and the black dot or string of dots represent the Dirichlet boundary at potential V. The red and green circles trace specific boundary points that map to the corners in the w-plane of panel (c).

We adopt two conformal map steps to transform the output of the scaling transformation, an infinite strip in the z'-plane, to a finite rectangle in the w-plane. One step transforms the infinite strip in z'-plane to an infinite semicircle in the upper-half s-plane, and the following step transforms the infinite semicircle in s-plane into a finite rectangle in w-plane. The first conformal map is:

$$s = \tanh(z'), \tag{2.26}$$

which transforms the infinite strip within $-\infty < x' < +\infty, 0 \leq y' \leq \pi/2$ in the complex z'-plane ($z' = x' + iy'$) in Fig. 2.3(a) into the upper half s-plane in Fig. 2.3(b). The infinite ground plane $y' = 0$ (purple line) is mapped into the finite segment $-1 \leq p \leq 1$ along the line $q = 0$ and the top point contact at $z' = i\frac{\pi}{2}$ is mapped onto infinity in the s-plane. The

points at the top of the infinite strip at $z' = \pm d + i\pi/2$ (red and green dots in Fig. 2.3a), map to the s-plane at $s = \pm 1/k$, where $k = \tanh(d)$.

The second conformal map is a Schwarz-Christoffel transformation [62] that maps the upper half-plane into a finite rectangle, as shown in Fig. 2.3(c). A SchwarzChristoffel mapping is a conformal transformation of the upper half-plane onto the interior of a simple polygon. Consider a polygon in the complex w-plane, there exists a mapping $w(s)$ from the upper half-plane $\{s \in \mathbb{C} : \mathrm{Im}\ s > 0\}$ to the interior of a polygon in the w-plane, which maps the real axis of the upper half-plane to the edges of the polygon. If the polygon has interior angles ϕ_1, ϕ_2, ..., ϕ_n, then the mapping is given by:

$$w(s) = C \int^s (\zeta - \zeta_1)^{-\phi_1/\pi} (\zeta - \zeta_2)^{-\phi_2/\pi} \cdots (\zeta - \zeta_n)^{-\phi_n/\pi} d\zeta, \tag{2.27}$$

where C is a constant, ζ is a real-value integral variable, and $\zeta_1 < \zeta_2 < \cdots < \zeta_n$ are the coordinates of the points along the real axis of the s-plane, which are corresponding to the vertices of the polygon in the w-plane. We choose a specific form of SchwarzChristoffel mapping that maps the upper half-plane in the s-plane to a rectangle in the w-plane:

$$\begin{aligned} w(s) &= -C/k \int_0^s (\zeta + 1/k)^{-1/2} (\zeta + 1)^{-1/2} (\zeta - 1)^{-1/2} (\zeta - 1/k)^{-1/2} d\zeta \quad (0 < k < 1) \\ &= C \int_0^{\sin^{-1} s} \frac{1}{\sqrt{1 - k^2 \sin^2\theta}} d\theta \ = \ C\, \mathrm{F}(\sin^{-1} s, k^2), \end{aligned} \tag{2.28}$$

where $-1/k, -1, 1, 1/k$ are the coordinates of the points on the real axis of s-plane that correspond to the vertices of the mapped rectangle in the w-plane, $\mathrm{F}(\phi, k^2)$ is the incomplete elliptic integral of the first kind $\mathrm{F}(\phi, k^2) = \int_0^{\phi} (1 - k^2 \sin^2\theta)^{-1/2} d\theta$ and C is

a scaling factor. After the second conformal map, the result is a finite rectangle with vertices $\pm K$ and $\pm K + iK'$, as shown in Fig. 2.3(c), where $K = C\,\mathrm{F}(\pi/2, k^2)$ and $K' = |C\,\mathrm{F}(\sin^{-1}(1/k), k^2) - K|$. The original infinite ground plane $y' = 0$ in z'-plane (purple line) in Fig. 2.3(a) is mapped to the bottom edge of the rectangle in w-plane, the top point contact at $z' = i\frac{\pi}{2}$ is mapped to the center of the top edge of the rectangle ($w = iK'$), and the red and green points on the top of the infinite strip at $z' = \pm d + i\pi/2$ are mapped to the top-left and top-right corners of the rectangle in w-plane. By inverting the scaling and conformal maps discussed above, the potential distribution in the anisotropic infinite strip can be easily calculated by first conducting a numerical simulation of the potential distribution in the isotropic, finite rectangle in the w-plane, and then using the inverse transformations to map the result to the desired anisotropic infinite strip in the z-plane.

2.2.2. Finite element method (FEM) numerical simulation

To simulate the potential distribution in an isotropic, finite rectangle, FEM code based on the open-box Matlab implementation [63] of Courant's P1 triangle elements for the numerical solution of elliptical problems with mixed boundary conditions is used. The rectangle is divided into multiple triangles using DistMesh [7], and the calculation uses the mapped isotropic conductivity tensor and boundary conditions as described in Section 2.2.1. As shown in Fig. 2.4, the mesh generating algorithm is modified to produce high-density triangle meshes near contacts, corner, and edges of the rectangle, and low-density meshes elsewhere, which results in a right balance between accuracy and speed for the following FEM simulation.

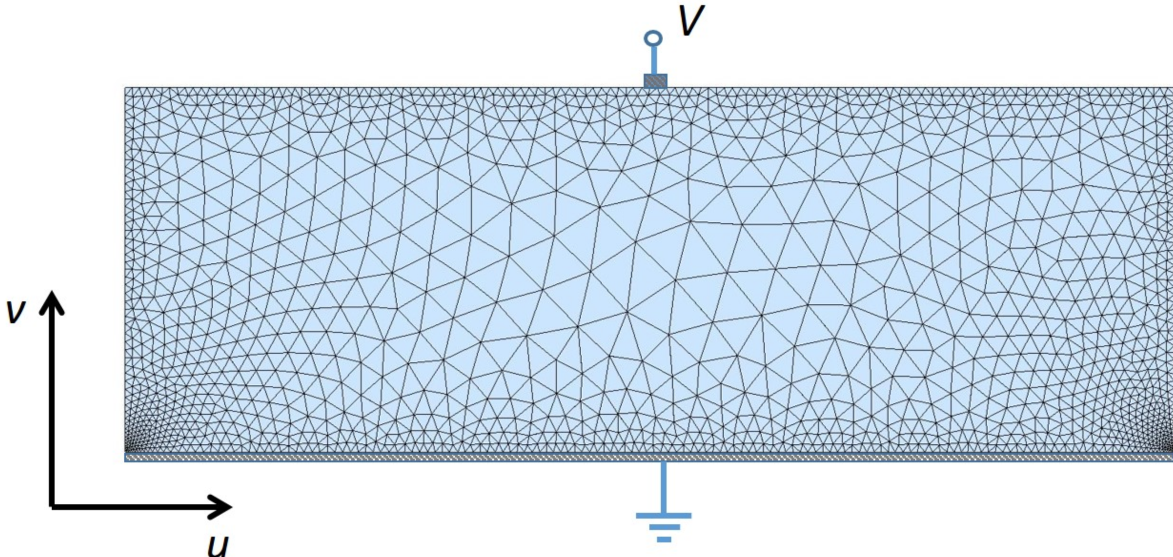

Figure 2.4. Triangle meshes generated in the finite rectangle in w-plane for FEM simulation. The rectangle is divided into small triangle elements using DistMesh [7]. The mesh density is enhanced near the stripline contact and the edges and corners of the rectangle, where the boundary conditions are applied, and a higher resolution is preferred.

FEM: accuracy and consistency

The accuracy of the FEM simulation is studied with a simple diagnostic structure shown in Fig. 2.5. The potential and current flux distribution is simulated in a finite rectangle with top and bottom facet contacts. As shown in Fig. 2.5(a), in a finite rectangle with top edge fixed at potential $\varphi = V$ and bottom edge grounded, the equipotential lines are confirmed to be parallel to the horizontal axis, while the current flux lines are along the vertical axis when the off-diagonal conductivity is zero ($\sigma_{uv} = 0$), *i.e.*, there is no external magnetic field present. The total current flowing through the rectangle can be analytically calculated with $I_{calc} = V\sigma_{vv}$. With FEM simulation, the total current can also be obtained by integrating the calculated current flux density along the top or bottom

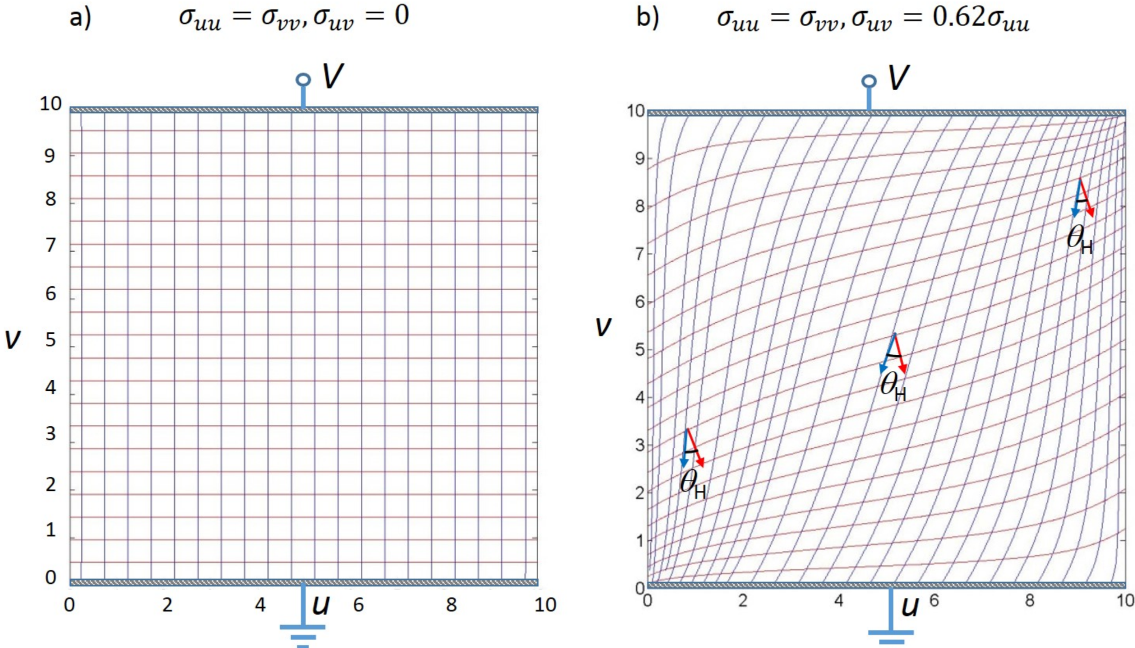

Figure 2.5. The FEM simulated potential distribution (red lines) and current flux density (blue lines) in a finite rectangle with top and bottom facet contacts with (a) zero and (b) non-zero off-diagonal component of the conductivity tensor. A Hall angle $\theta_H = \arctan(\sigma_{uv}/\sigma_{uu})$ is formed between the current flux and potential gradient directions.

edge, which yields a numerically simulated value I_{sim}. Simulations with various σ_{vv} values yield relative error:

$$\left|\frac{I_{sim} - I_{calc}}{I_{calc}}\right| \leq 0.1\%.$$

When $\sigma_{uv} \neq 0$, *i.e.*, an external magnetic field perpendicular to the uv-plane is present, the equipotential lines and current flux lines are no longer orthogonal, as shown in Fig 2.5(b). Instead, the current flux and potential gradient directions (the norm of equipotential lines) will form a Hall angle $\theta_H = \arctan(\sigma_{uv}/\sigma_{uu})$. For example, the Hall angle in Fig 2.5(b) is $\theta_H = \arctan(0.62) \approx 32°$. The potential and current flux distribution

in Fig 2.5(b) is consistent with previous numerical study of rectangular-shaped device in the presence of external magnetic field [64].

2.2.3. Potential distribution results

Figure 2.6 demonstrates the procedure of calculating the potential distribution in an infinite strip with anisotropic conductivity tensor in the presence of a B-field. Suppose the conductivity tensor in the infinite strip at z-plane has $\sigma_{yy}/\sigma_{xx} = 2, \sigma_{xy}/\sigma_{xx} = 1$, as shown in Fig. 2.6(c). Using the maps described in Section 2.2.1, the anisotropic infinite strip can be transformed to a rectangle in w-plane (Fig. 2.6a), with width $W_u = 32.6$ and thickness $t_v = 10$, and also an isotropic conductivity tensor $(\sigma_{vv}/\sigma_{uu} = 1, \sigma_{uv}/\sigma_{uu} = 1/\sqrt{2})$. The electric potential distribution (red lines) in this isotropic rectangle can be readily calculated with an FEM simulation solving Eq. (2.2) under the boundary conditions described by Eq. (2.3) and (2.4) (Fig. 2.6a). Using the inverse transformation of the maps described in last section, the potential distribution can be readily obtained in both s-plane (Fig. 2.6b) and z-plane (Fig. 2.6c), and the current flux density (blue lines) can be calculated with the corresponding conductivity tensors. From Fig. 2.6(c) we can see that in the anisotropic infinite strip, the potential drops at different rate in x and y directions, consistent with the expected conductance anisotropy $\sigma_{yy}/\sigma_{xx} = 2$. In addition both equipotential and current flux lines curve towards the left due to the finite magnetic field indicated by the non-zero Hall conductivity $\sigma_{xy}/\sigma_{xx} = 1$. To better understand the separate effects of the conductivity anisotropy and the finite magnetic field, we separately study the anisotropy ratio σ_{yy}/σ_{xx} and the off-diagonal conductivity ratio σ_{xy}/σ_{xx} in what follows.

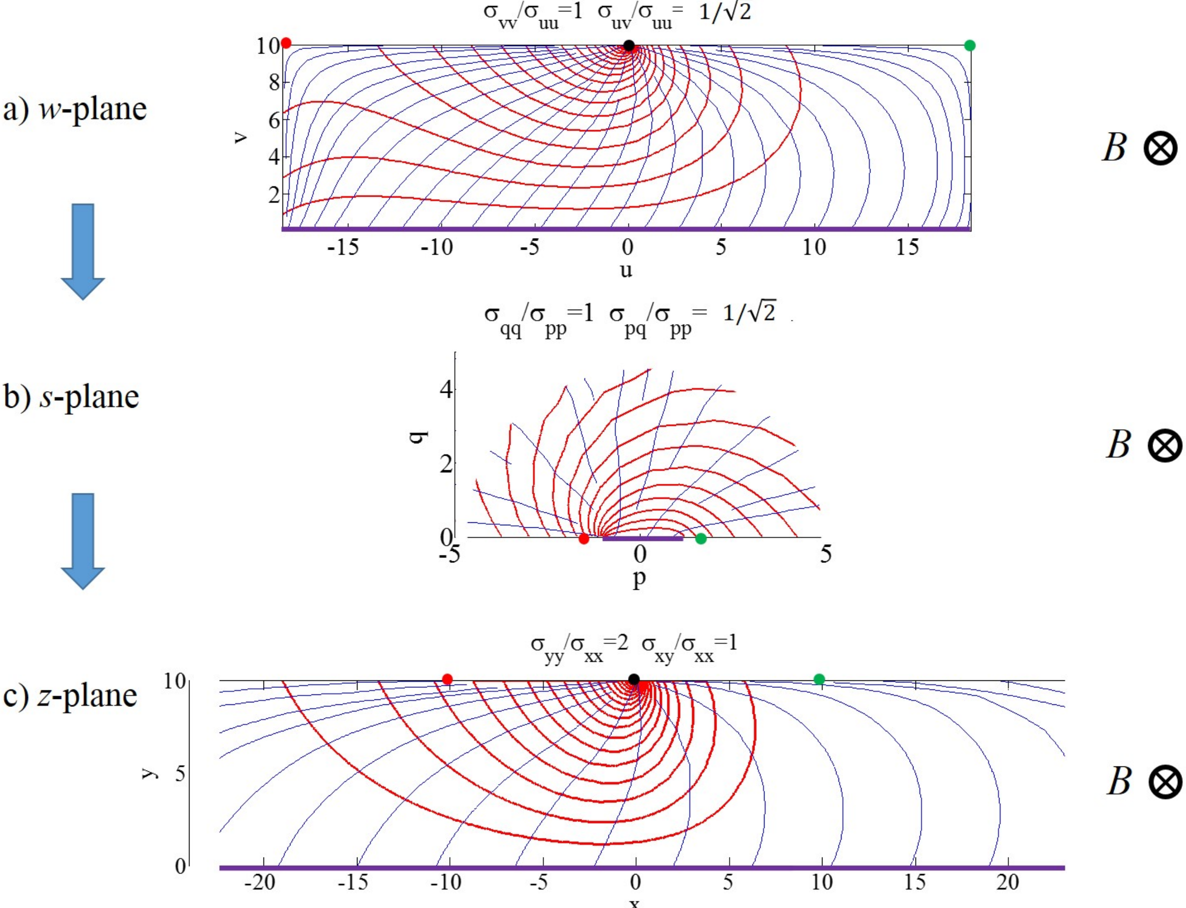

Figure 2.6. (a) The calculated potential distribution (red lines) and current flux density (blue lines) in the finite isotropic rectangle (w-plane) corresponding to $\sigma_{yy}/\sigma_{xx} = 2$ and $\sigma_{xy}/\sigma_{xx} = 1$ in the z-plane coordinates. (b) The potential distribution in the upper-half s-plane is mapped with an inverse Schwarz-Christoffel transformation from the w-plane. (c) The potential distribution in the z-plane is mapped with the inverse scaling transformation from the s-plane. The dots represent the locations of the top stripline contact (black) and corner coordinates in the w-plane (red and green). The purple line represents the ground plane.

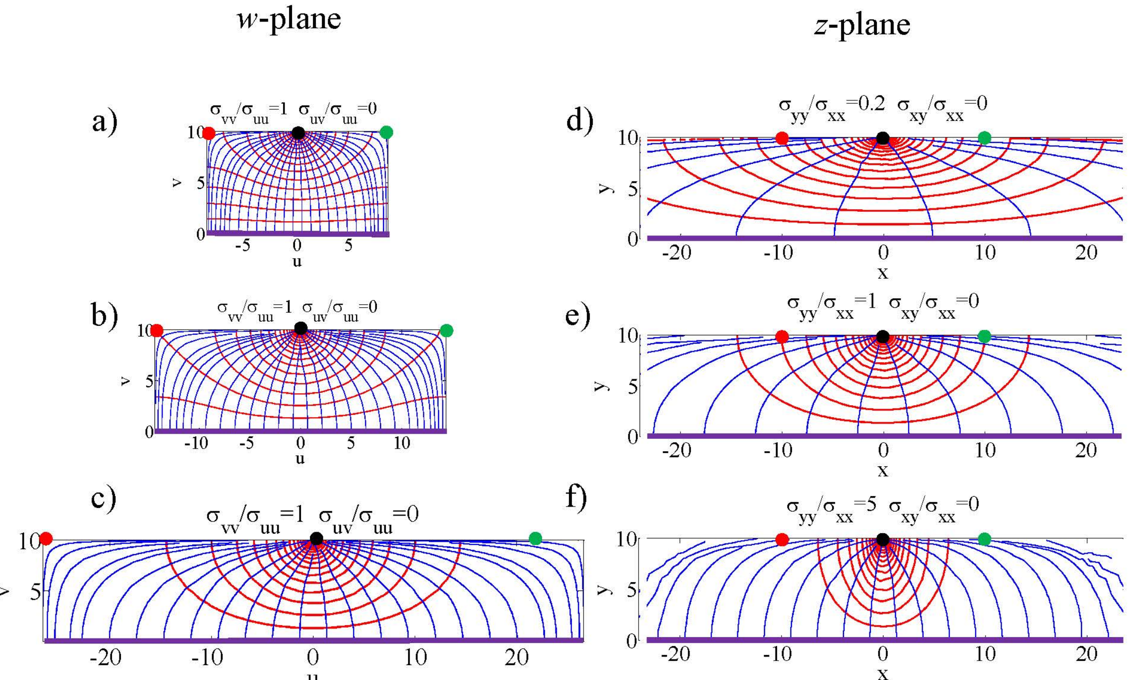

Figure 2.7. The FEM-calculated potential distribution in finite rectangles with isotropic conductivity are mapped to the infinite strip with $\sigma_{xy} = 0$ and anisotropy ratio (a) $A = \sigma_{yy}/\sigma_{xx} = 0.2$, (b) $A = 1$ (isotropic), and (c) $A = 5$. The mapped rectangles have thickness $t_v = 10$ and width $W_u = 17.7, 28.8, 53.5$ respectively. The resultant potential distribution representing the anisotropic infinite strip is shown in (d)-(f). The dots represent the stripline contact (black) and w-plane corner points (red and green), and the purple line represents the ground plane.

We first study the anisotropy ratio under zero magnetic field, whereby $\sigma_{xy} = 0$. The potential distribution of anisotropic infinite strips with anisotropy $A = \sigma_{yy}/\sigma_{xx} = 0.2, 1, 5$ is calculated from the FEM simulation of their mapped rectangles in the w-plane, as shown in Fig. 2.7. The aspect ratio W/t of the mapped rectangle in w-plane depends on

the anisotropy ratio A through the variable $k = \tanh(A^{1/2}\pi/2)$:

$$\frac{W_u}{t_v} = \frac{2\mathrm{F}(\pi/2, k^2)}{\mathrm{Im}[\mathrm{F}(\sin^{-1}(1/k), k^2)]}, \tag{2.29}$$

where $\mathrm{Im}(z)$ gives the imaginary part of a complex number z. As shown in Fig. 2.7(a)-(c), W_u/t_v increases with the anisotropy ratio A. The potential distribution changes dramatically as the conductivity anisotropy changes. For the isotropic case of Figs. 2.7(b) and 2.7(e) ($A = 1$), the equipotential lines start as semi-circles near the top stripline contact and flatten out near the bottom ground plane in Fig. 2.7(e). As the conductivity anisotropy A changes, the equipotential lines deviate from the isotropic case by extending toward the high conductivity direction, *i.e.*, x-direction for $A < 1$ in Fig. 2.7(d) and y-direction for $A > 1$ in Fig. 2.7(f), so the potential changes more slowly in the high conductivity direction. It should be noted that the equipotential lines and current flux lines are perpendicular to each other only in the isotropic case ($A = 1$) under zero magnetic field, whereby the conductivity tensor is effectively reduced to a scalar. We note that for single-carrier materials, under the Drude model, A does not change with magnetic field, whereas for multiple-carrier materials, the anisotropy ratio will become a function of the magnetic field $A(B)$.

The off-diagonal term σ_{xy} breaks the symmetry of the potential distribution about the y-axis under a magnetic field, as seen in Fig. 2.8. Consider an infinite strip with isotropic conductivity ($A = 1$) with subjected to three different magnetic field strengths so that $\sigma_{xy}/\sigma_{xx} = 0.2, 1, 5$ respectively. The potential distribution calculated by FEM for the rectangles in w-plane are shown in Fig. 2.8(a)-2.8(c), and the potential distribution of the original infinite strips in z-plane is shown in Fig. 2.8(d)-2.8(f). Both the equipotential

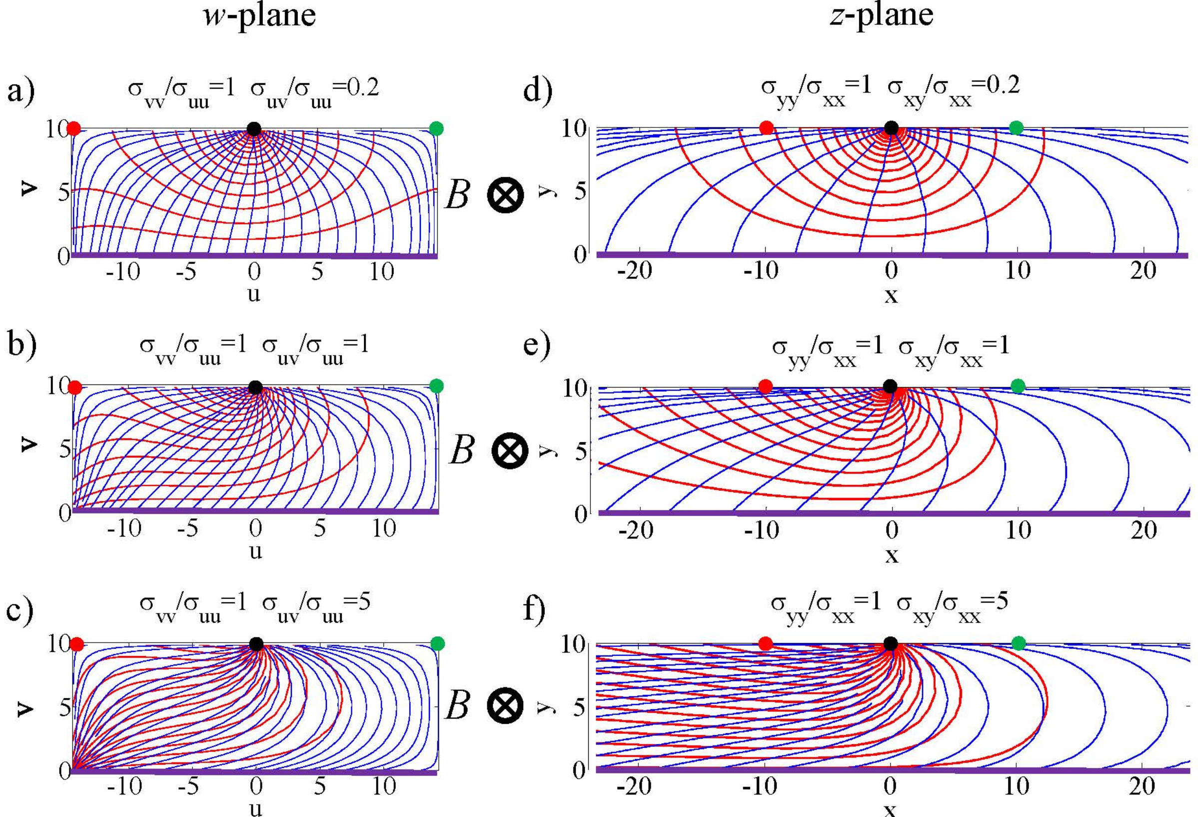

Figure 2.8. The FEM-calculated potential distribution for the case of an infinite strip with isotropic conductivity ($A = 1$) is plotted for various magnetic field strengths represented by σ_{xy}/σ_{xx} = (a) 0.2, (b) 1 and (c) 5. Because all plots are derived for the same conductivity anisotropy ratio $A = 1$, namely the isotropic case, the mapped rectangles have the same thickness $t_v = 10$ and width $W_u = 28.8$. The resultant potential distribution representing the infinite isotropic strip in a finite B-field is shown in (d)-(f).The dots represent the stripline contact (black) and w-plane corner points (red and green), and the purple line represents the ground plane.

and current flux lines are curved toward the bottom left corner of the strip (for an n-type sample assuming electrons dominate the conduction) under the magnetic field in the direction shown in the figure. As the ratio σ_{xy}/σ_{xx} increases, the curvature increases and eventually the current flux will concentrate to a so-called "hot spot" on the bottom left

corner. The voltage difference between the two points represented by red and green dots are $\Delta V = 0.0601V$, $0.2850V$ and $0.7296V$ respectively, and we can see that the voltage ΔV does not increase linearly with σ_{xy}/σ_{xx}, unlike conventional Hall bars. This indicates that there exists a longitudinal component in the resistance between these two symmetric points when the magnetic field exists, and as a result, we cannot directly measure a pure Hall resistance in this isotropic strip without mixing in some longitudinal resistance, due to the ground plane at the bottom shorting out the Hall voltage and causing asymmetric redistributions of the current with increasing B.

Understanding how the potential distribution changes with the conductivity anisotropy ($A = \sigma_{yy}/\sigma_{xx}$) and the non-zero σ_{xy} under external magnetic field is the first step towards developing a possible characterization method to determine the three independent components of the conductivity tensor. Since there are only three independent variables in the 2D anisotropic conductivity tensor (σ_{xx}, σ_{yy} and σ_{xy}), it should be possible to extract the full conductivity tensor by conducting three independent resistance measurements. However, unlike the conventional Hall bar structure whereby pure longitudinal conductivities (σ_{xx} and σ_{yy}) can be easily separated from the Hall conductivity (σ_{xy}), the interrelationship between these independent components here is more complex and requires careful consideration, as described in the next section.

2.3. Triple stripline method: theory

Based on the calculated potential distribution of anisotropic thin films atop a conductive substrate, we propose a novel characterization method to extract the full conductivity tensor, the triple stripline method. This method utilizes a diagnostic device structure

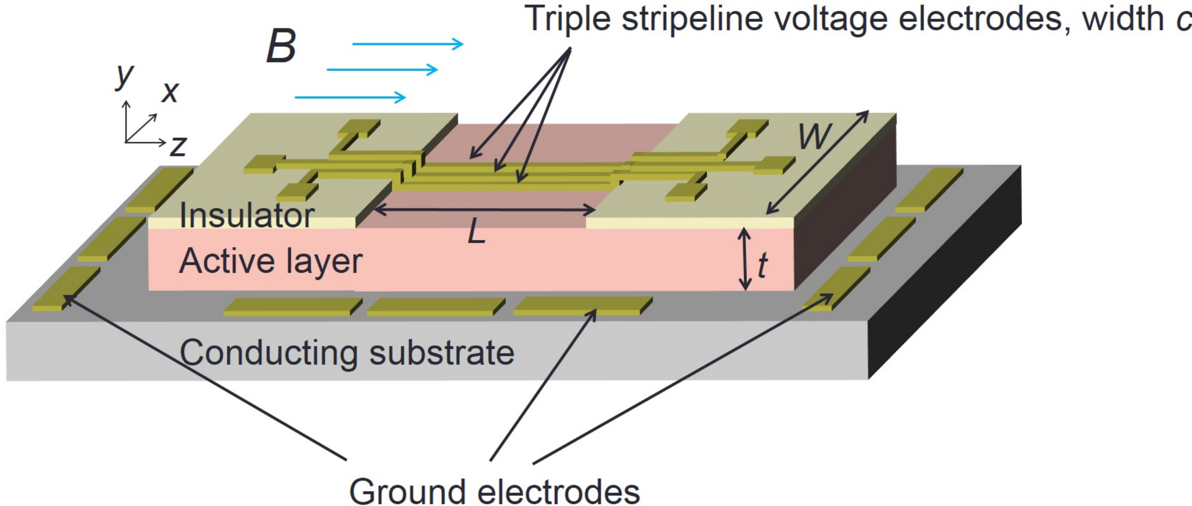

Figure 2.9. The triple stripline device structure for measuring the three independent conductivity components of an anisotropic active layer on a conducting substrate. Three narrow stripline electrodes are deposited on top of the active layer, with a pitch width equal to the active layer thickness t and a width much smaller than t.

(Section 2.3.1) with three narrow stripline contacts on top, as indicated by the name – one stripline serving as a current source and two others serving as voltage probes. The conductivity tensor is extracted by numerically calculating the potential distribution and resistances and comparing the measured resistances with calculation results, as discussed in Section 2.3.2. The device structure can be further adapted to materials with large conductivity anisotropy and materials grown on top of an insulating substrate, as shown in Section 2.3.3.

2.3.1. Device structure and measurement setup

The diagnostic device structure for the triple stripline method consists of an anisotropically resistive thin film layer atop a highly conductive bottom contact layer, with three

narrow stripline contacts on top, as shown in Fig. 2.9. As previously mentioned many optical devices such as photodetectors and emitters consist of a bottom heavily-doped backplane, a central undoped or lightly doped anisotropic superlattice active region and a top heavily-doped surface [29]. By etching away the top layer, and depositing three narrow metal strips as top contacts, theses devices can be readily modified to realize the proposed diagnostic structure. This structure requires that the stripline contact width c is significantly narrower than the thickness of the active layer t, so they can be treated as point contacts in the simulation. Along with the geometric constraints of the single stripline method described previously, the active layer should have a length L that is much larger than t as in Fig. 2.10. At the two ends, the stripline contacts extend over an insulating layer to allow larger contact pads for measurement convenience. The pitch between adjacent striplines is chosen to be equal to the film thickness $P = t$, as shown in Fig. 2.10.

Two sets of measurements are needed for the triple stripline method, as shown in Fig. 2.10. Measurement (I) in Fig. 2.10(a) applies current I from the left-most stripline contact 1 through the active layer to the ground plane contact at the bottom, and measures the potential of the other two stripline contacts 2 and 3 relative to ground (V_2 and V_3). Measurement (II) in Fig. 2.10(b) applies current I from the center stripline contact 1 to the bottom ground plane, and measures the potential of the two side stripline contacts 1 and 3 with respect to ground (V_1 and V_3). It should be noted that there are multiple ground electrodes around the device, so all the measurement are 4-point so that the results are independent of any contact resistances.

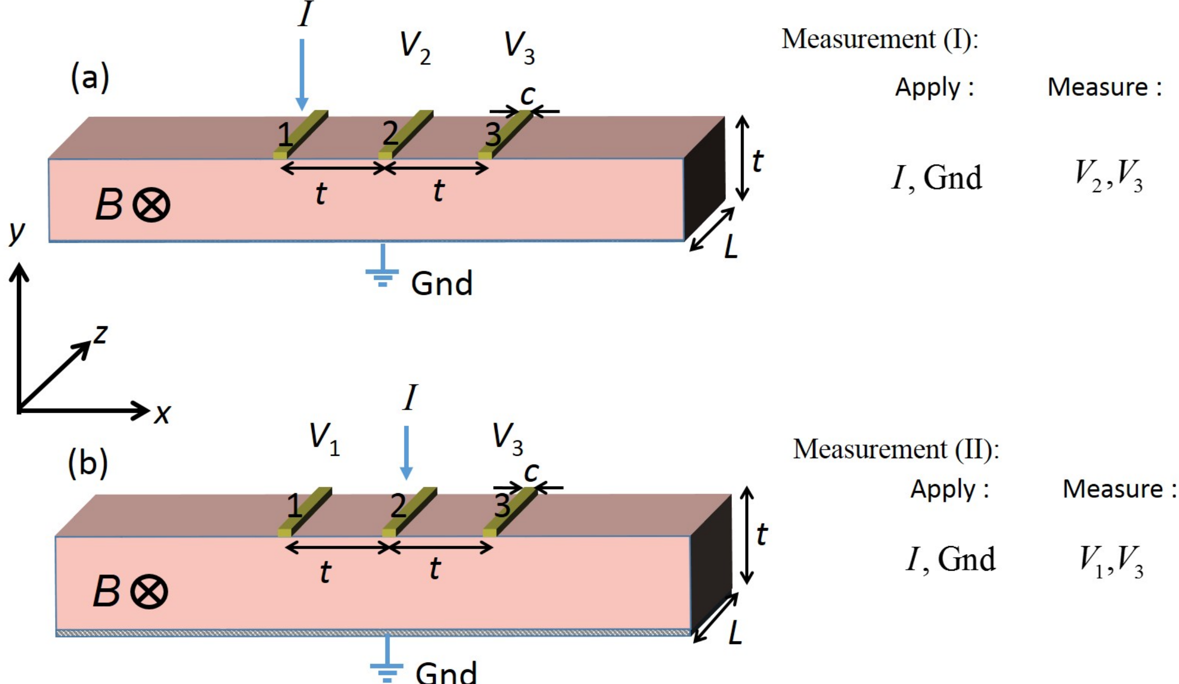

Figure 2.10. Two measurement setups with the triple stripline device. (a) Measurement I: apply current I from the left-most stripline contact 1 and measure four-point voltages V_2, V_3 relative to the ground plane. (b) Measurement II: apply current I from the center stripline contact 2 and measure voltages V_1, V_3 from the two sides relative to the ground plane.

The potential distribution of the device in the two measurements can be calculated with the model and the numerical simulation approach demonstrated in Sections 2.2 and 2.2.3 . For active layer below the striplines far from two ends, the potential and current flux distribution is uniform along z-axis. The method until now has allowed us to deduce the potentials V_i for the various configurations with a known anisotropy ratio and a known Hall angle. Now we need to invert this process by repeating this calculation for a continuum of different anisotropy factors and Hall angles, and then parametrically

plotting the result versus the various V_i voltages to be measured. The result will enable us to extract the conductivity tensor, as described in next section.

2.3.2. Deducing the full 2D conductivity tensor

The 2D conductivity tensor in the x-y plane for thin films with an external magnetic field has only three independent components. With aligned principal axes and external magnetic field $\boldsymbol{B} = B\hat{\boldsymbol{z}}$ the conductivity tensor can be re-written as

$$\boldsymbol{\sigma} = \begin{bmatrix} \sigma_{xx} & \sigma_{xy} \\ -\sigma_{xy} & \sigma_{yy} \end{bmatrix} = \sigma_{xx} \begin{bmatrix} 1 & -\sigma_{xy}/\sigma_{xx} \\ \sigma_{xy}/\sigma_{xx} & \sigma_{yy}/\sigma_{xx} \end{bmatrix} = \sigma_{xx} \begin{bmatrix} 1 & -\tan\theta_H \\ \tan\theta_H & A \end{bmatrix}. \tag{2.30}$$

This tensor has three independent components: the anisotropy ratio $A = \sigma_{yy}/\sigma_{xx}$, the tangent Hall angle $\tan\theta_H = \sigma_{xy}/\sigma_{xx}$ and the longitudinal conductivity amplitude σ_{xx}. The full tensor can therefore be extracted from three independent measurements: V_2/V_3, $(V_2 - V_3)/I$ in measurement I of Fig. 2.10(a), and V_1/V_3 in measurement II of Fig. 2.10(b).

Conductivity tensor components ratios

The first step in identifying the three unknowns in the conductivity tensor is to determine the anisotropy ratio $A = \sigma_{yy}/\sigma_{xx}$ and the tangent Hall angle $\tan\theta_H = \sigma_{xy}/\sigma_{xx}$. From the Laplace equation and boundary conditions governing the potential distribution, the normalized potential distribution only depends on these two ratios, independent of absolute magnitude of the tensor. To study how these two ratios affect the potential distribution, we consider the following two special cases of zero magnetic filed but varying

anisotropy, and of isotropic conduction with varying magnetic field, similar to Section 2.2.3:

I) No external magnetic field ($\sigma_{xy} = 0$)

The potential distribution of the infinite anisotropic strip is symmetric around the top current contact in the absence of a magnetic field. Figure 2.11(a)reproduces the results of Fig. 2.7 (d)-(f) for the varying anisotropy ratio $A = \sigma_{yy}/\sigma_{xx}$. To quantify the effect of anisotropy on potential, we measure the ratio V_2/V_3 with measurement I in Fig. 2.10(a). For small anisotropy ratio $A < 1$, the equipotential lines are horizontally stretched, leading to a low line density along the top edge and thus a small ratio $V_2/V_3 = 2.3$. As the anisotropy ratio A increases, the equipotential lines become horizontally compressed, resulting in a high line density near the current source along the top edge and a large ratio V_2/V_3.

The potential ratio V_2/V_3 exhibits a monotonically increasing dependence on the anisotropy ratio $A = \sigma_{yy}/\sigma_{xx}$, as shown in Fig. 2.11(b). Thus for a given measured potential ratio V_2/V_3, the corresponding anisotropy ratio can be readily extracted from the curve. It has to be noted that for large anisotropy ratios, the magnitudes of V_2 and V_3 become very small and the relative measurement error can be large. But in practice most anisotropic materials have higher in-plane conductivity than that in the out-of-plane direction, *i.e.*, $\sigma_{yy}/\sigma_{xx} < 1$. In this case, the potential ratio $V_2/V_3 \leq 5$ can be measured with a reliable accuracy.

II) Isotropic material ($A = \sigma_{yy}/\sigma_{xx} = 1$)

The off-diagonal tensor components σ_{xy} breaks the symmetry of the normalized equipotential lines around y-axis under a magnetic field. As shown in Fig. 2.12, as the normalized

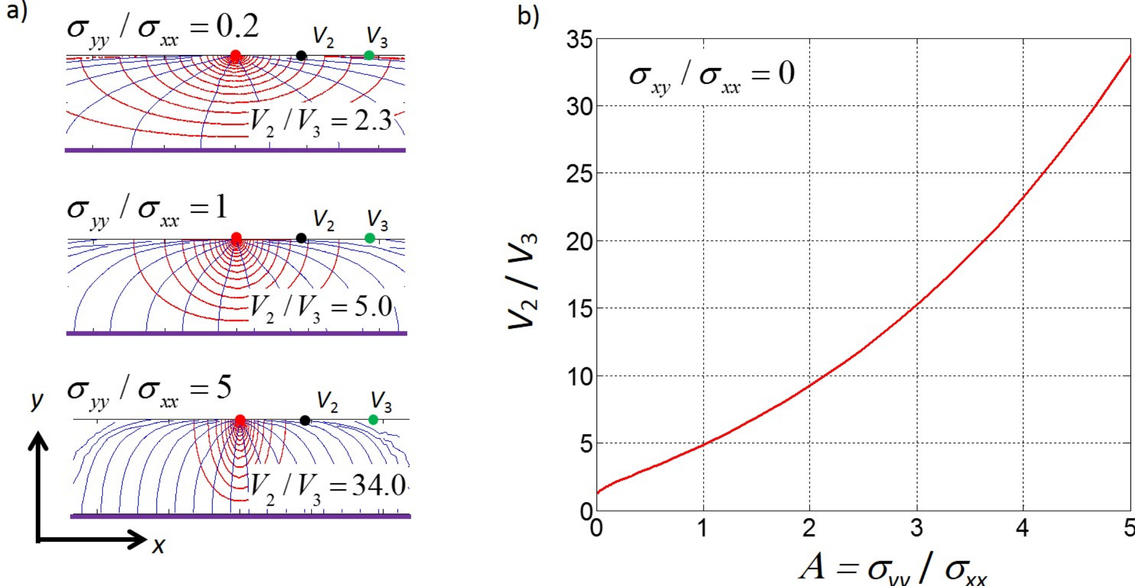

Figure 2.11. (a) The potential distribution of the infinite strip for different conductivity anisotropy ratio $A = \sigma_{yy}/\sigma_{xx}$, when $\sigma_{xy} = 0$ reproduced from Fig. 2.7 (d)-(f). (b) The calculated voltage ratio V_2/V_3 increases monotonically with the anisotropy ratio $A = \sigma_{yy}/\sigma_{xx}$.

Hall conductivity σ_{xy}/σ_{xx} increases, both the equipotential and current flux lines curve towards one side, resulting in an increasing asymmetry. Unlike a conventional Hall bar structure in which the potential distribution asymmetry is evaluated as a potential difference, here we use the ratio V_1/V_3 as measured with the second setup in Fig. 2.10(b) to reflect the "normalized" potential distribution asymmetry.

Similar to case I), the potential ratio V_1/V_3 in the second measurement monotonically increasing with the normalized Hall conductivity σ_{xy}/σ_{xx}, which enables the inverse mapping from the measured V_1/V_3 to σ_{xy}/σ_{xx}. However, the increase in V_1/V_3 with σ_{xy}/σ_{xx} is even steeper than that of V_2/V_3 with respect to σ_{yy}/σ_{xx} in Fig. 2.11. Thus the measurement error will limit the practical application of the inverse mapping to small normalized

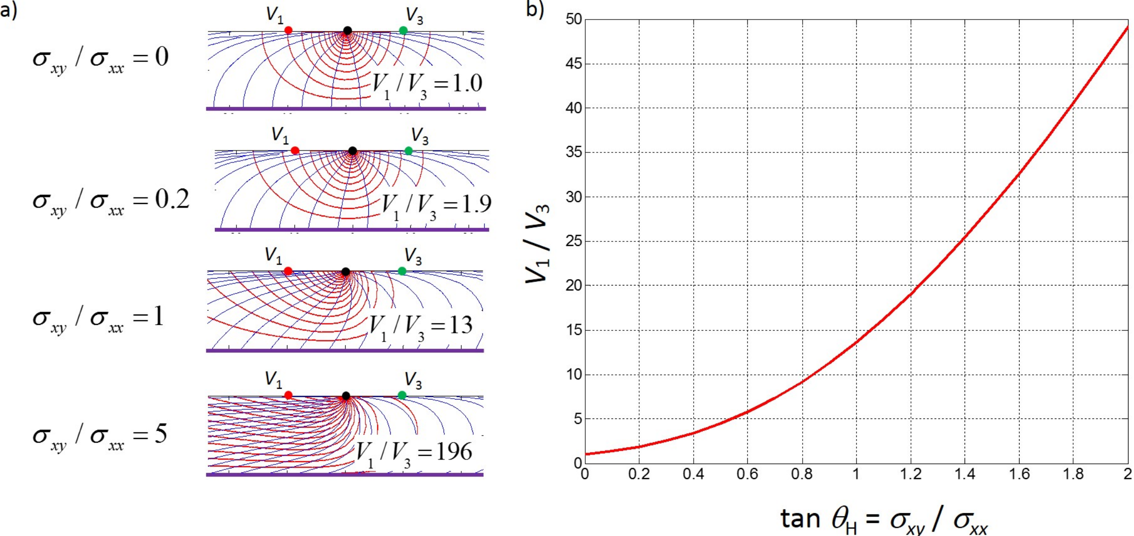

Figure 2.12. (a) The potential distribution of the infinite strip for isotropic conductivities ($A = \sigma_{yy}/\sigma_{xx} = 1$) with varied $\tan\theta_H = \sigma_{xy}/\sigma_{xx}$ ratios, which can be induced by different magnetic field strengths, as reproduced from Fig. 2.8(d)-(f). (b) The calculated voltage ratio V_1/V_3 increases monotonically with the tangent Hall angle $\tan\theta_H = \sigma_{xy}/\sigma_{xx}$.

Hall conductivity, *e.g.* $\sigma_{xy}/\sigma_{xx} \leq 1$. Fortunately, this is the low-magnetic field limit, which is readily accessible. For conductors with one single species of carrier, the tangent Hall angle is $\tan\theta_H = \sigma_{xy}/\sigma_{xx} = \mu B$, whereby μ is the Hall mobility. So the inverse mapping from V_1/V_3 to the normalized Hall conductivity σ_{xy}/σ_{xx} is most useful in the weak field limit, appropriate to the classical Hall regime.

The inverse mapping from the measured potential ratios (V_2/V_3 and V_1/V_3) to the respective conductivity parameters (A and $\tan\theta_H$, respectively) for the two special cases discussed above can be generalized to a two-dimensional parametric mapping to deduce the two conductivity parameters for an arbitrary case. The unique relation between the

potential ratios and the conductivity tensor components ratios can be expressed as:

$$
\begin{aligned}
V_2/V_3 &= f_x(\sigma_{yy}/\sigma_{xx}, \sigma_{xy}/\sigma_{xx}), \\
V_1/V_3 &= f_y(\sigma_{yy}/\sigma_{xx}, \sigma_{xy}/\sigma_{xx})
\end{aligned} \tag{2.31}
$$

in which f_x and f_y are nonlinear functions of the anisotropy ratio $A = \sigma_{yy}/\sigma_{xx}$ and the tangent Hall angle $\tan\theta_H = \sigma_{xy}/\sigma_{xx}$. If the mapping from $(\sigma_{yy}/\sigma_{xx}, \sigma_{xy}/\sigma_{xx})$ to $(V_2/V_3, V_1/V_3)$ can be proven to be a one-to-one mapping, then there should exist an inverse mapping:

$$
\begin{aligned}
\sigma_{yy}/\sigma_{xx} &= F_x(V_2/V_3, V_1/V_3), \\
\sigma_{xy}/\sigma_{xx} &= F_y(V_2/V_3, V_1/V_3)
\end{aligned} \tag{2.32}
$$

Although it is difficult to analytically prove the inverse relation mathematically, the one-to-one mapping can be verified graphically.

Figure 2.13 shows the contour map of the potential ratio V_2/V_3 (solid lines) and V_1/V_3 (dashed lines) plotted on Cartesian coordinates of the tensor components ratios σ_{yy}/σ_{xx} and σ_{xy}/σ_{xx}. Every pair of solid and dashed contour lines only have one intersection in the first quadrant, indicating the mapping between $(\sigma_{yy}/\sigma_{xx}, \sigma_{xy}/\sigma_{xx})$ and $(V_2/V_3, V_1/V_3)$ is an one-to-one mapping. With known measured potential ratios (e.g. $V_2/V_3 = 6$, $V_1/V_3 = 12$), the two corresponding contour lines (blue solid and red dashed lines) can be determined, and their intersection point uniquely indicates the conductivity components ratios ($\sigma_{yy}/\sigma_{xx} = 0.49$ and $\sigma_{xy}/\sigma_{xx} = 0.87$). It can be observed that for most situations the two sets of contour lines have a finite intersection angle, which promises reliable accuracy for this inverse mapping. For the extreme case of small anisotropy ratio

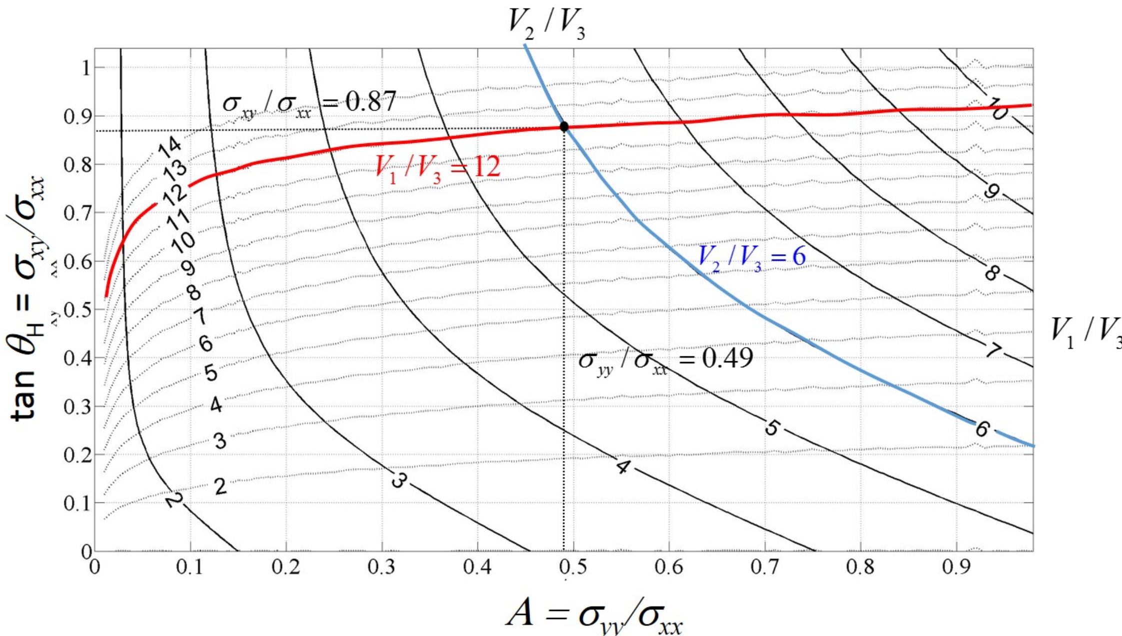

Figure 2.13. Contour map of with iso-voltage-ratio lines V_2/V_3 (measurement I, solid line) and V_1/V_3 (measurement II, dashed line) for the tangent Hall angle $\sigma_{xy}/sigma_{xx}$ and anisotropy ratio σ_{yy}/σ_{xx}. For any pair of measured voltage ratios, *e.g.* $V_2/V_3 = 6$ and $V_1/V_3 = 12$, corresponding contour lines can be located from the map (blue and red), and their intersection uniquely defines the values for σ_{yy}/σ_{xx} and σ_{xy}/σ_{xx}.

$\sigma_{yy}/\sigma_{xx} < 0.05$ the contour lines for V_1/V_3 are crowded and become almost parallel with the contour lines of V_2/V_3 nearby. The characterization of this extreme case will be covered in Section 2.3.3. With this contour map of the potential ratios, the only independent tensor component remaining unknown is the amplitude of σ_{xx}.

Conductivity tensor component amplitude

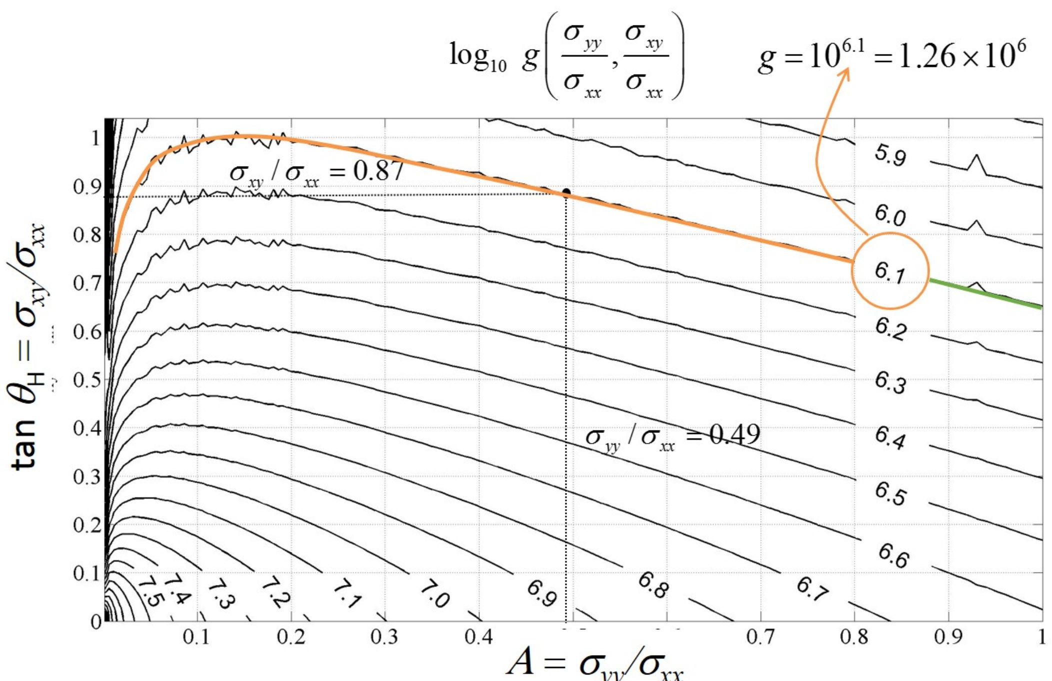

Figure 2.14. Contour map of the factor g as a function of the conductivity component ratios σ_{yy}/σ_{xx} and σ_{xy}/σ_{xx}. Once g is determined, the conductivity component amplitude can be calculated with $\sigma_{xx} = g\left(\frac{\sigma_{yy}}{\sigma_{xx}}, \frac{\sigma_{xy}}{\sigma_{xx}}\right)\frac{I}{V_{23}\cdot L}$, whereby $V_{23} = V_2 - V_3$ in the first measurement.

The conductivity amplitude represented by σ_{xx} can be determined by the potential difference $V_{23} = V_2 - V_3$ in the first measurement. It can be shown that:

$$\sigma_{xx} = g\left(\sigma_{yy}/\sigma_{xx}, \sigma_{xy}/\sigma_{xx}\right)\frac{I}{V_{23}L}, \tag{2.33}$$

whereby $g\left(\sigma_{yy}/\sigma_{xx}, \sigma_{xy}/\sigma_{xx}\right)$ is a unitless scalar. Fig. 2.14 shows the common logarithm of the numerically calculated factor g as a function of σ_{yy}/σ_{xx} and σ_{xy}/σ_{xx}. The range of the factor g for small anisotropy ratio ($\sigma_{yy}/\sigma_{xx} \leq 1$) and weak magnetic field ($\sigma_{xy}/\sigma_{xx} \leq 1$)

limit is $g \sim 10^6$-10^7 when the current I, potential difference V_{23} and stripline length L use SI units. As one example, with the conductivity components ratios $\sigma_{yy}/\sigma_{xx} = 0.49$ and $\sigma_{xy}/\sigma_{xx} = 0.87$ as determined in Fig. 2.13, the corresponding factor g is $g = 10^{6.1} = 1.26 \times 10^6$. It has to be noted that large value of the factor g may amplify the measurement error of the potential difference V_{23}, the current I and the stripline length L. Thus the conductivity tensor component amplitude σ_{xx} is expected to have a larger error compared with the components ratios. It is suggested to use a conventional in-plane planar device as reviewed in Section 1.1 to examine the amplitude of σ_{xx} for consistency check if high accuracy is needed.

As a summary of the triple stripline method characterization procedures, the full conductivity tensor is extracted with two steps. The first step is determining the anisotropy ratio $A = \sigma_{yy}/\sigma_{xx}$ and the tangent Hall angle $\tan\theta_H = \sigma_{xy}/\sigma_{xx}$ from two measurements. Measurement (I) applies the current from the left-most stripline contact 1 and measure the potential ratio of the other two contacts V_2/V_3, and Measurement (II) applies the current from the center stripline contact 2 and measure the potential ratio of the other two contacts V_1/V_3. Then σ_{yy}/σ_{xx} and σ_{xy}/σ_{xx} can be extracted from the parametric plot of the potential ratios V_2/V_3 and V_1/V_3. The second step is determining the conductivity amplitude from the numerically calculated factor g and the measured potential difference $V_{23} = V_2 - V_3$, as well as the current I and stripline length L in the first measurement. For materials with non-equivalent in-plane principal axes x and z, a second triple stripline device can be fabricated with the device rotated around the vertical axis (y) by 90° to

characterize the 2D conductivity tensor in the y-z cross-section. Combining the characterization results from two such devices, the electrical transport properties such as the carrier density and Hall mobility in all three directions can be extracted.

2.3.3. Expansion of triple stripline method

As discussed in the last section, the application of the triple stripline method is limited to materials with small conductivity anisotropy in the weak magnetic field limit, and it considers only the technologicallly relevant case of a highly conductive substrate. In this section, we discuss how to expand the triple stripline method to other regimes. Adjusted structures and measurement setups are proposed to apply this method to thin films with large or small conductivity ratios and thin films with insulating substrates.

Large or small conductivity components ratios

The major bottleneck limiting the application of the triple stripline method to materials with large anisotropy or Hall angles lies in the step of extracting conductivity components ratios σ_{yy}/σ_{xx} and σ_{xy}/σ_{xx} from the appropriate plot. As shown in Fig. 2.15, increasing the two ratios to 10 results in potential ratios V_2/V_3 and V_1/V_3 in the order of 10^3, in which case the amplitudes of the denominator potentials V_2 and V_3 become extremely small, seriously limiting the practical measurement accuracy. To reduce the relative measurement error, it is required to increase the normalized amplitude of V_2 and V_3.

One possible solution to this problem is to reduce the distance between neighboring stripline contacts. As shown in Fig. 2.11(a) and Fig. 2.12(a), as the conductivity ratios increase, the equipotential lines get severely compressed or distorted. To increase the

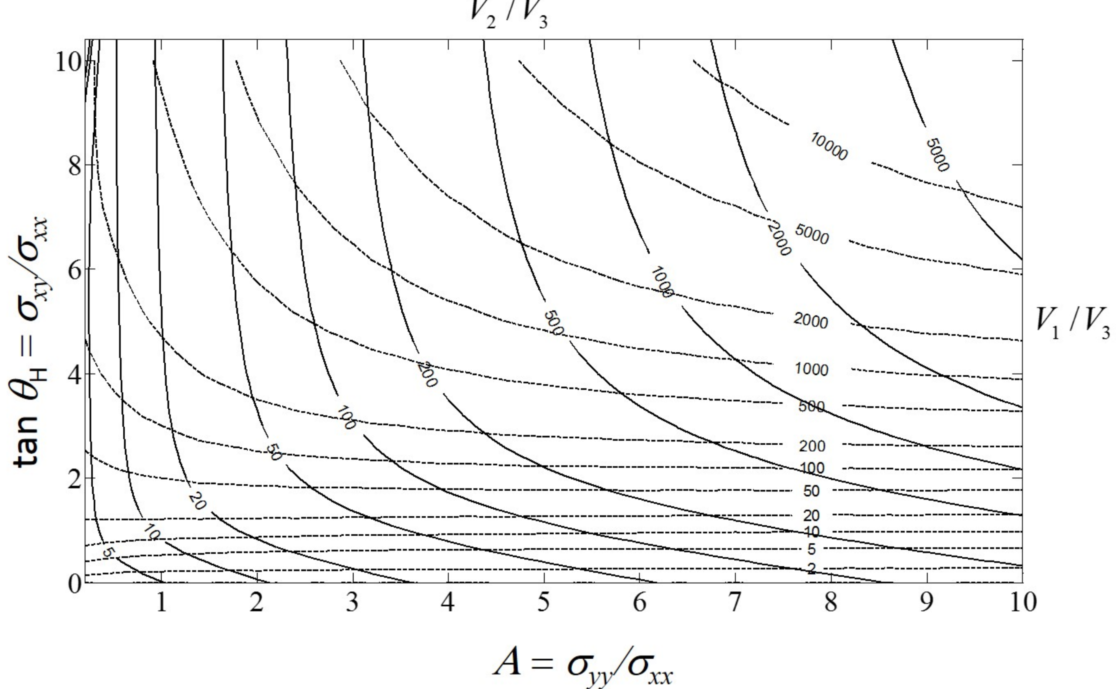

Figure 2.15. Contour map of V_2/V_3 (Measurement I), solid line) and V_1/V_3 (Measurement I), dashed line) as a function of the conductivity anisotropy ratio σ_{yy}/σ_{xx} and the ratio σ_{xy}/σ_{xx}, identical to Fig. 2.13, but for a larger range..

normalized amplitude of V_2 and V_3, the voltage contacts on the top edge should be moved closer to the current contact, *i.e.*, the pitch width, or the distance between neighboring striplines should be reduced. However, to preserve the validity of the infinite strip model, it is required that the pitch width between neighboring striplines to be much larger than the stripline width, which is limited by the fabrication technique of the metal stripline contacts.

Similarly, for extremely small conductivity tensor components ratios, mainly extremely small anisotropy ratio σ_{yy}/σ_{xx}, the equipotential lines are severely stretched in the horizontal direction, resulting in a ratio V_2/V_3 close to 1. To solve this problem, we can

increase the distance between neighboring contacts. Again to maintain the infinite strip model, it is required the stripline pitch width is much smaller than the device width W and stripline length L.

In practice, the potential distribution and ratios will be calculated for specific device structures to compare with experimental measurement results. The contour map of the potential ratios and the factor g can be calculated for triple stripline structure with increased/decreased stripline pitch width as mentioned above, or even devices with non-equal pitch widths between the metal striplines. Then the full conductivity tensor can be extracted with these calculation results and the two measurements as discussed in the last section.

Insulating substrate: Penta stripline method

For an anisotropic active layer grown on top of an insulating substrate, a penta stripline method can be applied instead of the triple stripline method. As shown in Fig. 2.16, the penta stripline device has 5 instead of 3 metal stripline contacts on top surface. The two measurement setups use the side stripline contact as the ground. With the two potential ratios V_2/V_3 from Measurement (I), and V_2/V_4 from Measurement (II), and the amplitude of $V_2 - V_3$ from the first measurement, the full conductivity tensor can be extracted following similar procedures as the triple stripline method. To enhance the accuracy, in the first measurement we can also switch the source current contact and the ground contact, and measure the two voltage stripline contacts on the right half of the device (V_3 and V_4), and then take the average of V_2/V_3 and V_4/V_3.

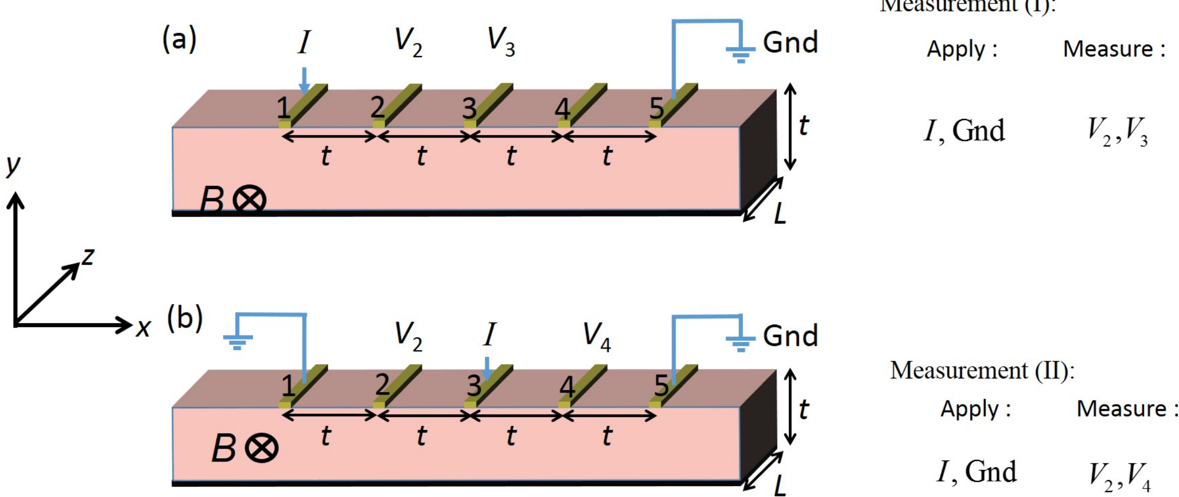

Figure 2.16. Two measurement setups with the penta stripline device. (a) Apply current I between two side stripline contacts on top and measure four-point voltages V_2, V_3 relative to the ground. b) Apply current I from the center stripline contact and ground the two contacts on two sides, measure voltages V_2, V_4 of the stripline contacts between the current source and ground.

2.4. Triple stripline method: device fabrication

The triple stripline method can be applied to any homogeneous, anisotropic materials that have one principle axis of anisotropy perpendicular to the film. Since all the dimensions are relative, the film thickness can range from macroscale to microscale, with the lower limit sets by fabrication techniques. To illustrate the fabrication of the triple stripline device structure, the III-V compound semiconductor GaAs and the GaAs/AlGaAs superlattices are chosen as a representative of isotropic and anisotropic materials, respectively. The growth protocol for the triple stripline devices are designed to achieve varied conductivity anisotropy ratios. Fabrication procedures and challenges will be discussed, while the complete device fabrication is yet to be finished.

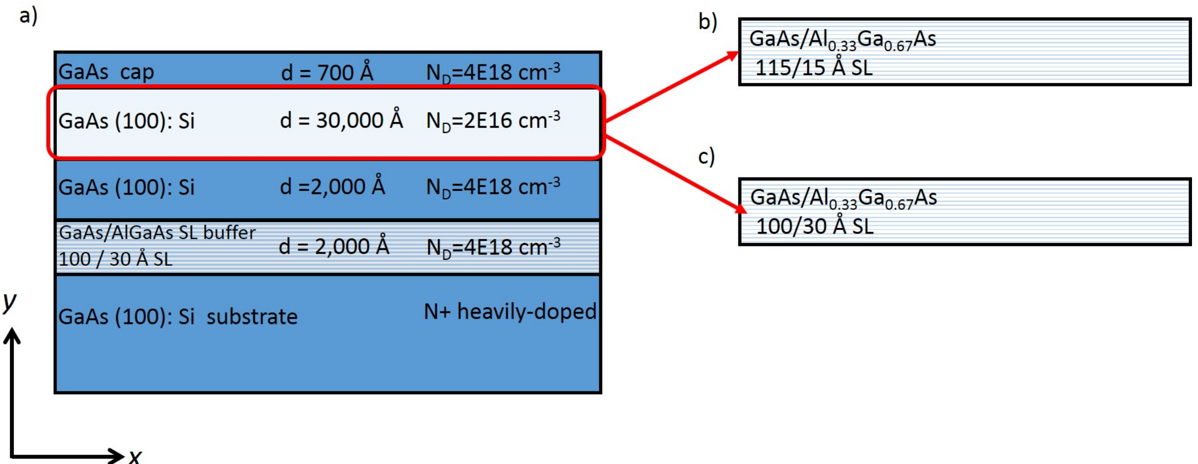

Figure 2.17. The growth protocol of GaAs and GaAs/AlGaAs superlattice based triple stripline devices. The 3 μm thick active layer is lightly doped ($N_D = 2 \times 10^{16}$cm^{-2}) (a) single crystal GaAs with (100) orientation (b) GaAs/$Al_{0.33}Ga_{0.67}As$ (115 / 15 Å) suplerlattice and (c) GaAs/$Al_{0.33}Ga_{0.67}As$ (100 / 30 Å). The three different active layers will provide different conductivity anisotropy ratios.

2.4.1. Growth protocol

Single crystal GaAs with (100) orientation and GaAs/$Al_{0.33}Ga_{0.67}As$ superlattice active layer with thickness $t = 3$ μm are grown on top of highly conductive GaAs substrate with molecular beam epitaxy (MBE). The MBE growth protocols are shown in Fig. 2.17. The active layer is lightly-doped with $N_D = 2 \times 10^{16}$ cm^{-3}, while both the top GaAs cap and the bottom contact layer below the active layer are heavily doped with $N_D = 4 \times 10^{18}$ cm^{-3} to ensure the ohmic contact quality and uniform potential distribution in the ground layer. The thickness $t = 3$ μm is chosen so that the required metal stripline thickness is reasonable for thermal evaporation. A GaAs/AlGaAs superlattice buffer layer is added

between the bottom contact layer and the substrate to reduce the dislocation defect density and provide a smoother growth interface.

Fabrication procedures

There are mainly four fabrication steps, insulation layer SiN sputtering, alignment marks evaporation, the metal contacts fabrication and finally the GaAs cap layer etching. Each step contains several processes, as shown in the list below:

(1) Insulation layer

- E-beam lithography for SiN rectangular agrea and alignment marks (Fig. 2.18a)
- High temperature (T = 180 °C) Si_3N_4 sputtering with t_{SiN} = 60 nm and liftoff

(2) Alignment mark

- Negative photolithography with the alignment mark pattern (Fig. 2.18b)
- Thermal evaporation of Ni/Au = 10/80 nm and liftoff

(3) Metal contacts

- E-beam lithography with the narrow stripline patterns and large contacts (Fig. 2.18c)
- Thermal evporation of Ni/Au = 30/200 nm and liftoff
- Indium contacts soldering to the substrate on scratched corners and annealing at 180 °C for 60 seconds.

(4) GaAs cap layer etching

- Reactive ion etching (RIE) of the heavily doped GaAs cap layer atop the active layer.

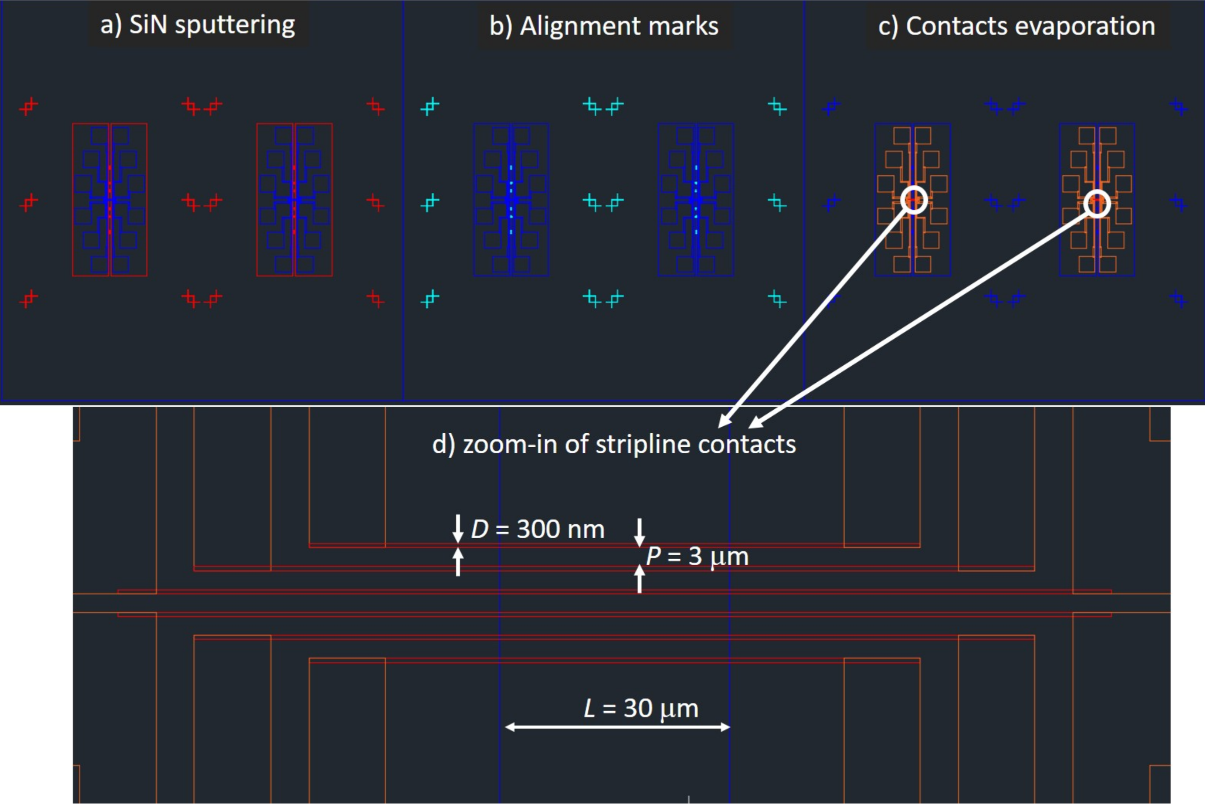

Figure 2.18. E-beam and photolithography mask patterns (a)-(c) and zoom-in for narrow metal stripline evaporation patterns (d).

Figure 2.18 shows the E-beam and photolithography patterns used in the fabrication. The SiN insulating layer are sputtered for two rectangles (Fig. 2.18a) seperated by a gap of L = 30 µm (Fig. 2.18d). Both the patterns for insulating SiN layer sputtering and contacts evaporation (Fig. 2.18c) are fabricated by E-beam lithography. To align the SiN patterns and metal contacts patterns, one additional metal alignment mark layer is fabricated by photolithography (Fig. 2.18b), since SiN is too dim under electron beam for any alignment. The zoom-in view of the narrow metal striplines with width $D = 300$ nm and pitch $P = 3$ µm is shown in Fig. 2.18(d).

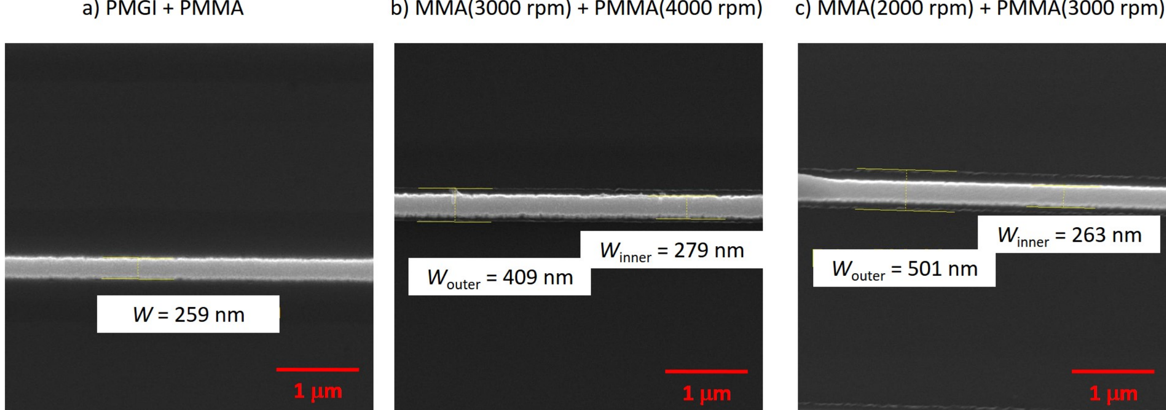

Figure 2.19. SEM images of the metal strip contacts after liftoff with ebeam lithography bilayer resist consisting of : (a) PMGI + PMMA, (b) MMA (3000 rpm) + PMMA (4000 rpm) and (c) MMA (2000 rpm) + PMMA (3000 rpm). The number in the parentheses is the spinning rate, the lower of which leads to the thicker and more stiff resist layer. The ebeam lithography pattern line width is set to be $W = 250$ nm. The latter two resist combinations have different width for different layers of the metalization, which may be attributed to the larger undercut and smaller thickness compared with the first resist combination.

2.4.2. Fabrication challenges and future work

The major challenge in the fabrication procedures is the fabrication of narrow stripline ohmic contacts. One aspect of this challenge is the patterning of narrow metal striplines, including the Ebeam lithography, thermal evaporation and liftoff. Another challenge is the ohmic contact recipe to GaAs and AlGaAs that does not require a high annealing temperature. Although this challenge has been resolved, the fabrication of the final triple stirpline device is still yet to be finished and the experimental measurement will be in the future work.

I) Ebeam lithography and evaporation

The Ebeam lithography patterning and thermal evaporation of the narrow metal striplines require a special bi-layer resist structure. The metal stripline thickness required for the device is around $t_{\mathrm{metal}} \sim 250$ nm, as discussed in Section 2.4.1. The bi-layer resist MMA/PMMA is widely used in e-beam lithography for metal evaporation. However, as a good rule of thumb, it is required that the lower layer of resist (MMA) should be at least twice the thickness of the metal to deposit. Thus it requires $t_{\mathrm{MMA}} >= 2t_{\mathrm{metal}} = 500$ nm, which is beyond the thickness limit of MMA resist film, unless a very low spin rate is used, which results in non-uniform resist. The small thickness of the MMA layer in the MMA/PMMA bi-layer resist and relative large undercut leads to the widening of the metal striplines, as shown in Fig. 2.19(b) and (c). The cause of the widening can be attributed to the fact that metal sources in the boats at two sides of the thermal evaporator (Ni and Ge) have different incident angles compared with the metal source in the center boat (Au). As a result, metal atoms evaporated from two side boats can enter the undercut region of the bi-layer MMA/PMMA resist and create a widened region.

To solve this problem, a thicker and more rigid bi-layer resist PMGI/PMMA is used. The thickness of PMGI is around $t_{\mathrm{PMGI}} \sim 700$ nm $> 2t_{\mathrm{metal}}$. The resulting metal striplines evaporated are shown in Fig. 2.19(a). To determine the optimal dosage for this bi-layer resist, a series of dosage tests are performed. As shown in Fig. 2.20, the optimal dosage for the narrow striplines is dosage = 400 $\mu\mathrm{C/cm}^2$ (Fig. 2.20b), while that for the ears of the striplines at two ends (designed for a good overlapping with the large area contact pads patterned with photolithography) is dosage = 300 $\mu\mathrm{C/cm}^2$. With the PMGI/PMMA bi-layer resist and optimal dosage calibrated in e-beam lithography, uniform narrow metal striplines with a width reasonably close to the designed width can be evaporated.

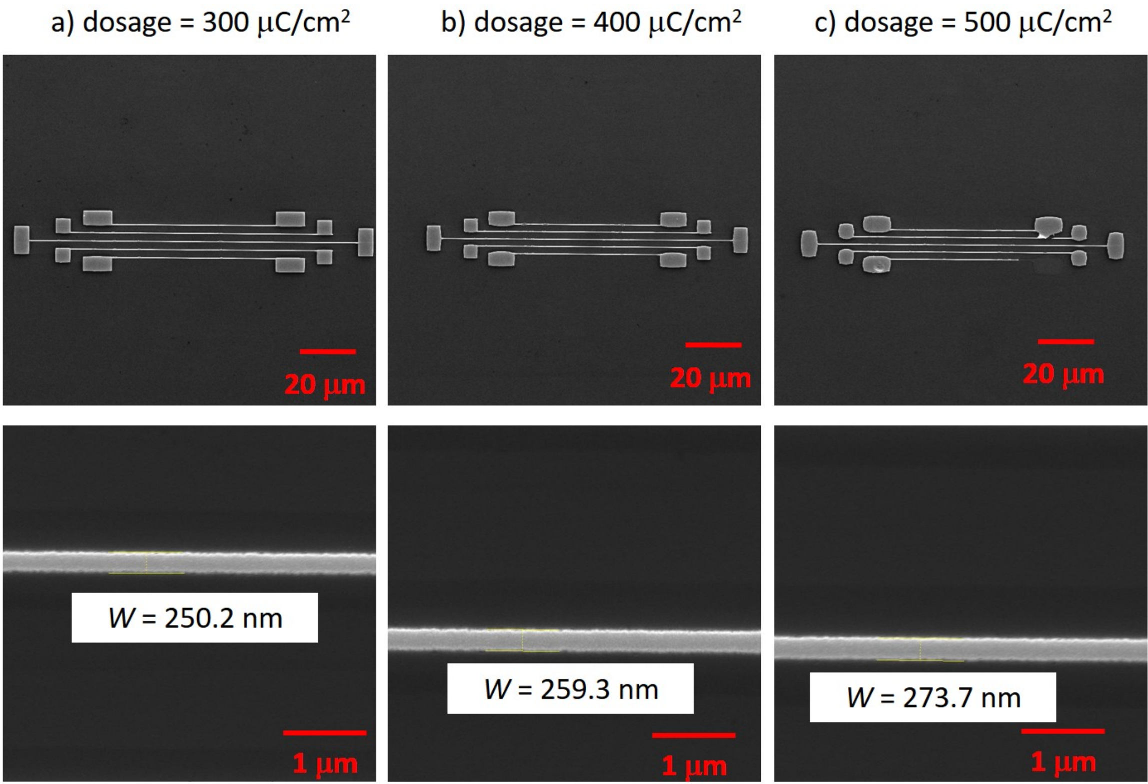

Figure 2.20. Dosage test for PMGI + PMMA bilayer resist. The SEM images of the metal strips after liftoff with various dosages are shown on top. The zoom-in images at bottom show that the width of the metal strips increase with dosage.

II) Non-annealed ohmic contacts

There was great difficulty in creating ohmic contacts with the standard AuGe/Ni recipe. The AuGe/Ni metalization has been widely used for ohmic contacts to n-type GaAs and AlGaAs [65–67]. The ohmic contact recipes based on the AuGe/Ni system require annealing at temperatures higher than 360 °C, which is the melting point of the AuGe eutectic. However, all the metal stripline contacts are measured to be non-ohmic after annealing.

The annealing might have caused the failure of the AuGe/Ni based contacts. Large horizonal and vertical diffusion in high annealing temperature due to the melting of the contact metals and dissolution of GaAs [68] have been reported. The typical lateral edge deterioration after annealing at 440 °C for two minutes is around 0.19 μm, with the worst case observed to be around 0.5 μm [69]. The vertical diffusion depth is around 0.2 μm after annealing [70]. Both the lateral and vertical diffusion distances are comparable to the pitch width of the narrow striplines. Given the small width and thickness of the stripline contacts compared with the pitch width, large area, non-uniform defects below these striplines can be expected.

To avoid the problem of annealing, non-annealed contacts consisting of a small work function metal layer at the bottom and a highly conductive gold layer on top have been attempted, including Ti/Au, Al/Au and Ni/Au. The heavily doped GaAs cap layer on top can potentially form ohmic contacts with metals with small work function, even without annealing. The Ni (30 nm)/ Au(200 nm) contacts are proven to be ohmic for a thick, heavily doped GaAs cap layer with $t_{cap} = 70$ nm. A thinner GaAs cap layer can result in non-ohmic contacts as well, which may be caused by the depletion near the cap surface due to surface-trap-induced mid-gap pinning. With the Ni/Au stripline ohmic contacts, the complete triple stripline devices will be fabricated, and the experimental measurement will be finished in the future work.

III) T-shaped stripline contacts

Another future improvement to the fabrication procedure is to evaporate T-shape stripline contacts with SiN mask layer, as shown in Fig. 2.21. With $W_{\mathrm{top}} = 2.5$ μm $\gg W_{\mathrm{bot}} = 300$ nm, the metal stripline resistance R_{metal} is reduced by a factor of 8. Such a

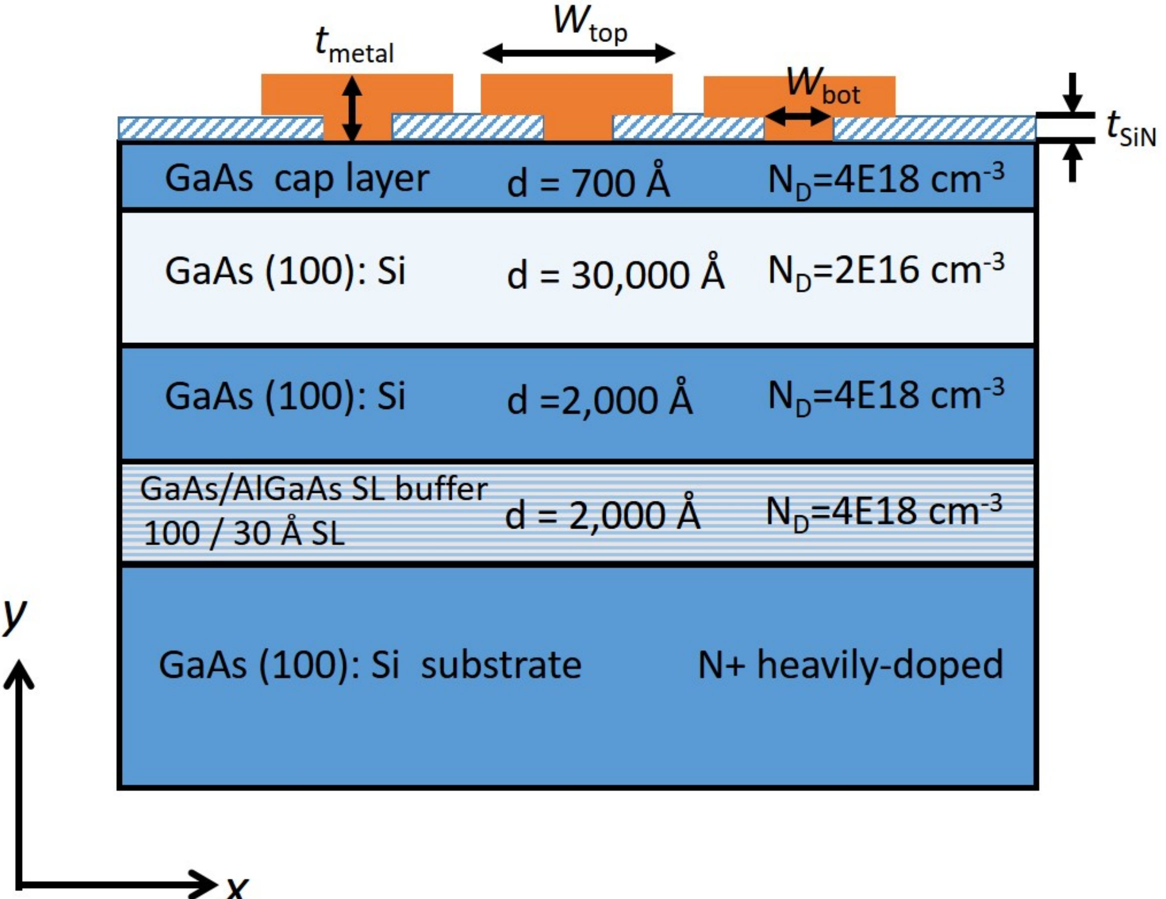

Figure 2.21. Cross-section view of the triple stripline device with T-shape narrow stripline contacts. The metal contacts have narrower bottom width to fit the point contact model, and larger top width to reduce the metal strip resistance and ensure the uniform potential distribution along the strip direction.

T-shape metalization can enhance the quality of the contacts by eliminating any residual resist and can reduce the required metal stripline thickness t_{metal}, which opens up more possibilities for ohmic contact recipes.

CHAPTER 3

Synthesis of anisotropic thin film semiconductors

In this chapter, the synthesis of three artificial thin film semiconductors with anisotropic in-plane electrical conductivities will be introduced, including aligned carbon nanotube stripes, 3D-printed graphene-polymer stripes and ion implantation isolated AlGaAs stripes. Section 3.1 introduces the *p*-type anisotropic thin film formed by aligned carbon nanotube stripes, whereby the aligned conduction channel arrays are fabricated via the evaporation-driven self-assembly (EDSA) methods. Section 3.2 shows aligned graphene-polymer stripes fabricated by the three-dimensional printing technology, which also exhibits anisotropic *p*-type in-plane conduction. Section 3.3 demonstrates the creation of anisotropic conductivity in both *n* and *p*-type bulk crystals such as AlGaAs via ion implantation isolation.

3.1. Aligned carbon nanotube (CNT) stripes

In this section, we demonstrate an approach to fabricate aligned CNT stripe arrays with large in-plane conductivity anisotropy ratio. In principle, one-dimensional (1D) nanostructure such as nanowires (NWs) and nanotubes(NTs) can be aligned to form anisotropic thin film conductors. Theoretically, aligned conduction channel arrays can be fabricated from any material to create a conductivity anisotropy, as long as the aspect ratio of length to width is large enough; thus the 1D nanostructures become the natural candidates for making anisotropic films. Among many different 1D nanostructures that

have been studied, carbon nanotubes (CNTs) are of particular interest due to their high and highly oriented electrical conductivity, mechanical strength, and optical properties. Anisotropic conductivity has been reported for vertically aligned CNT arrays [**71**], which can be potentially used as interconnecting materials. However, CNT films with in-plane conductivity anisotropy had not been heavily studied before this work.

3.1.1. CNT stripe array preparation

Aligned CNT stripe arrays are fabricated with the evaporation-driven self-assembly (EDSA) method [**72**,**73**]. The alignment of CNTs is required to retain the anisotropic conductivity of individual nanotubes when they form a conducting layer. There are many different in-growth or post-growth alignment methods for CNTs, and we decided to adopt the EDSA method since it offers a convenient approach to align electronically monodisperse CNTs into high-density, large area, homogeneous stripe arrays or thin films [**5**]. EDSA utilizes the well-studied "coffee-ring phenomenon", where particles suspended in a droplet tend to aggregate at the edges of the drop, forming a ring-like structure. This pinning of the droplet edge is caused by the frictional force between the substrate and the particle suspension coupled with accelerated evaporation at the contact line. Electronically monodisperse semiconductor SWCNTs sorted by density gradient ultracentrifugation (DGU) [**74**]are dispersed into specific solutions and by changing the surfactant or nanotube concentration [**5**], aligned arrays of isolated stripes with different width and space can be formed (Fig. 3.1). The pitch width (center-to-center stripe distance, P) will increase with stripe width (W) up to $P \sim 40\,\mu\text{m}$, when the stripes converge into a continuous film [**5**].

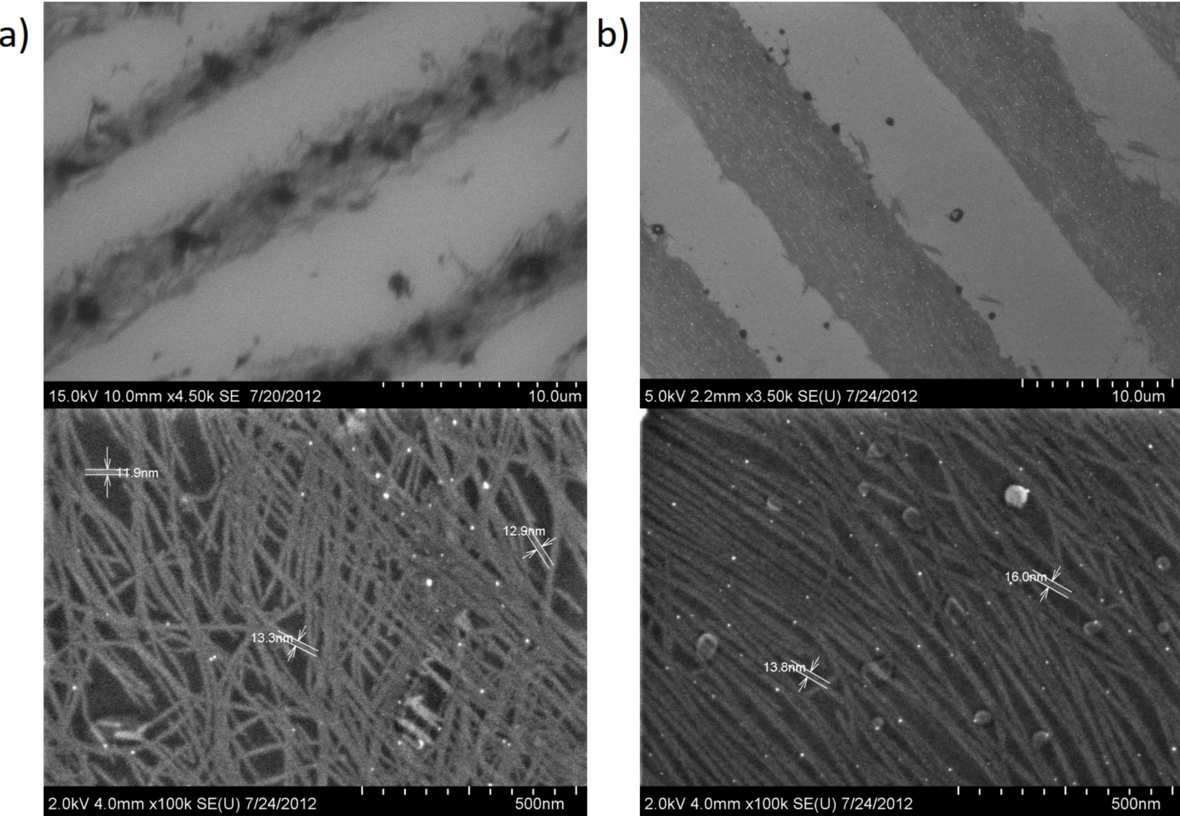

Figure 3.1. Scanning electron microscopy (SEM) images of aligned single-wall carbon nanotube (SWCNT) stripes with stripe width of (a) $W \sim$ 1-3 μm (b) $W \sim$ 5-7 μm. For each panel, the morphology of stripes is shown in the top images. Each stripe consists of a group of aligned SWCNT bundles around 10-15 nm in diameter as shown in the high-contrast SEM images of a single stripe at the bottom. The wider stripe shows better morphological uniformity and alignment.

The morphology and alignment of the semiconducting CNT stripes are studied by scanning electron microscopy (SEM). The CNT stripe width varies from $W = 1$ μm to $W = 20$ μm. Continuous films are not studied here since the conductivity anisotropy will be weakened by misaligned nanotubes forming a percolating network as the film thickness increases [5]. Single SWCNTs with diameter around 1 nm twist together to

form bundles with diameter 10-15 nm, as shown in the SEM images (Fig. 3.1 bottom panels). The bundles are then aligned into parallel stripes. As the stripe gets wider the CNT density increases and the uniformity of the stripes improves, as observed from the top panels of Fig. 3.1. Also, the alignment of CNT bundles are shown to be better for wider stripes (Fig. 3.1 bottom panel comparison). The stripe width to pitch width ratio (W/P) increases almost linearly with stripe width W when $W < 10$ μm (Fig.3.2b), however, it stays around 0.5 for $W = 10$ - 20 μm. When $W > 20$ μm the ratio W/P will increase again and finally saturates to 1 [5] when $W \sim 40$ μm (not shown).

3.1.2. As-grown p-type CNT stripes

Large in-plane conductivity anisotropy is achieved for as-grown p-type CNT stripes. Aligned stripes are deposited on an insulating substrate, and the four-point method was adopted to measure the longitudinal resistance between two adjacent gold pads $R_{||}$ (Fig. 3.2a). The space between these square gold pads is equal to their side length, so with measured $R_{||}$, the average longitudinal bulk conductivity along the stripe direction $\sigma_{||} = 1/R_{||}d$ can be calculated, where the average stripe thickness is $d = 20$ nm as measured with atomic force microscopy (AFM). Similarly, the effective transverse conductivity $\sigma_{\perp}$ is measured, which is almost zero due to the gap between stripes. Thin films formed by these aligned as-grown CNT stripes will only conduct in the longitudinal direction, and stay insulating in the transverse direction.

$\sigma_{||}$ increases monotonically with stripe width from W =1 μm to $W = 20$ μm as shown in Fig. 3.2(b). The increasing trend is partly due to the increasing stripe width to pitch width ratio W/P from around 0.25 to 0.5, but the trend continues between 10 μm and 20

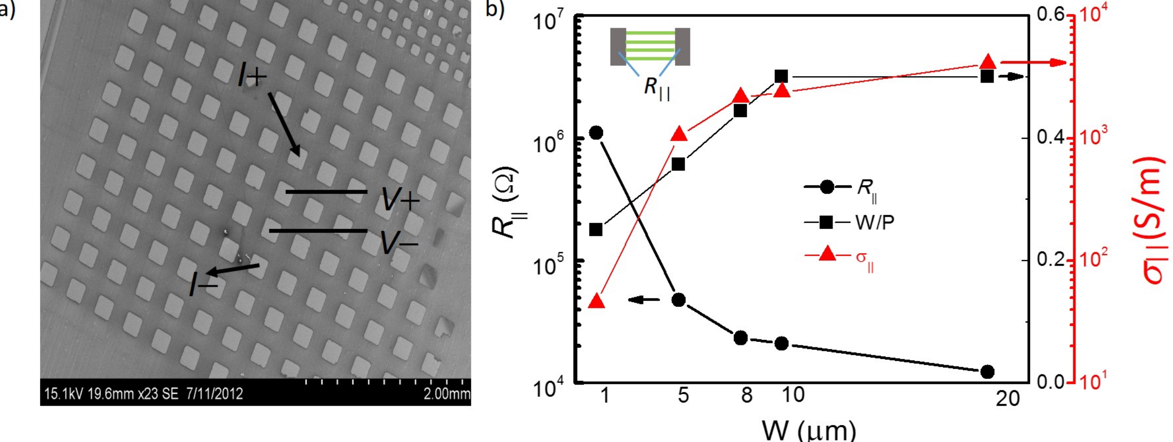

Figure 3.2. (a) Scanning electron microscopy (SEM) images of aligned CNT stripes deposited on a Si substrate with SiO_2 insulating layer. Gold pads are deposited on top of CNT stripes. The 4-probe method is used to measure the longitudinal resistance between two adjacent gold pads: $R_{||} = (V_+ - V_-)/I$. (b) Average longitudinal conductivity $\sigma_{||}$ (triangles) for different width of as-grown p-type CNT stripes. The longitudinal resistance $R_{||}$ (circles) for multiple CNT stripes between two gold pads is measured to be decreasing with increasing stripe width W. The stripe width/pitch ratio W/P (squares) increases almost linearly when $W < 10$ μm, and stays around 0.5 for 10 μm $< W <$ 20 μm.

μm where the ratio stays around 0.5, indicating that the better morphological uniformity and alignment of wider stripes also help to enhance $\sigma_{||}$. Note how the coverage fraction W/P seems to saturate near 50% in the limit of wider stripes. The measured conductivity of $\sigma_{||} = 10^3$ - 10^4 S/m agrees with that of 148 nm diameter SWCNT bundle ($\sigma_{||} \sim 1 \times 10^3$ S/m) [75] and long SWCNT strands ($\sigma_{||} \sim 3 \times 10^3$ S/m) [76]. Since large $\sigma_{||}$ is normally preferred for electronic and thermoelectric devices, wider stripes or even continuous thin films are the better choice from the aspect of electrical conductivity. However, a finite

gap between adjacent stripes is still needed to ensure the insulation in the transverse direction.

3.1.3. *n*-type CNT stripe fabrication attempts

Unlike the as-grown *p*-type CNT stripe arrays, *n*-type CNT stripes require additional processing. The as-grown SWCNTs are *p*-type due to oxygen doping in air. To obtain the *n*-type aligned SWCNT arrays, both gate-field modulation and chemical/electrochemical doping have been attempted. However, air-stable *n*-type CNT arrays are proved not achievable with existing technologies.

I) Gate-field modulation

Gate-field modulation can tune the Fermi level in carbon nanotubes and change the electron/hole density of the CNT conducting channel. It has been reported that *n*-type conductance was sometimes observed in a *p*-type semiconducting SWCNT field effect transistor at large positive gate voltages, especially in large-diameter tubes [77,78]. Also the gate-field modulation of the Seebeck coefficient of an individual semiconductor SWCNT, with a peak $S \sim 260\ \mu V/K$ at room temperature, has been reported [79]. So we decided to implement gate-field modulation on the as-grown *p*-type SWCNT stripes as an attempt to fabricate *n*-type CNT stripes.

The device structure (Fig. 3.3 inset) used for gate-field modulation is similar to a CNT field effect transistor. As-grown *p*-type SWCNTs are aligned into stripes on SiO_2 insulating layer, and gold pads are deposited on top of SWCNT stripes as source, drain contacts. The channel direction is along the stripe direction. The heavily doped silicon substrate served as a back-gate.

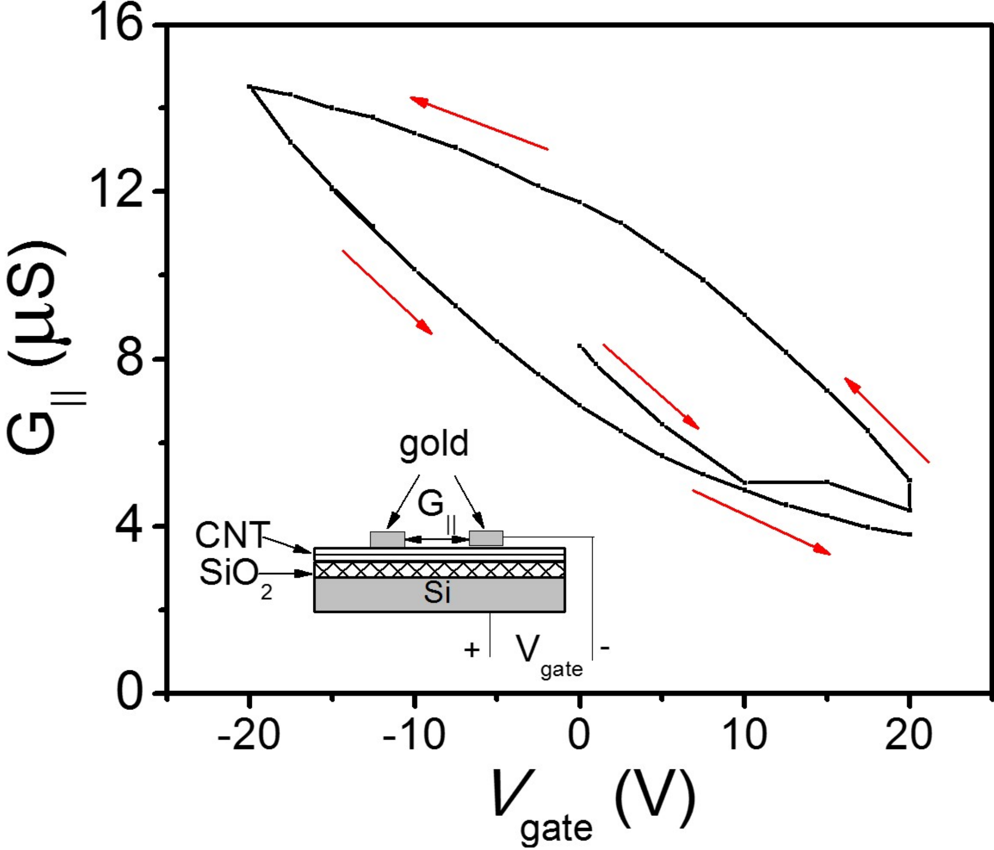

Figure 3.3. Longitudinal conductance $G_{||}$ hysteresis versus gate voltage from -20 V to +20 V. $G_{||}$ is determined by taking an $I-V$ curve at each V_g value plotted above. The device structure is similar to a back-gated CNT-based field-effect transistor, as shown in the inset. The red arrows depict the sweep directions. For V_g up to +20 V, the p-CNT channel is still not pinched off, as indicated by non-zero $G_{||}$, which may be caused by the much larger thickness of the CNT stripes compared with the diameter of a single CNT. The hysteresis is attributed to the injection and trapping/de-trapping of carriers in the SiO_2 at large V_g [8].

The p-type conductance is modulated by nearly a factor of 4 when gate voltage sweeps from -20 V to $+$ 20 V (Fig. 3.3). The hysteresis of $G_{||}$ in the gate sweep may be due to the injection and trapping/de-trapping of carriers in the SiO_2 layer at large gate voltages [8].

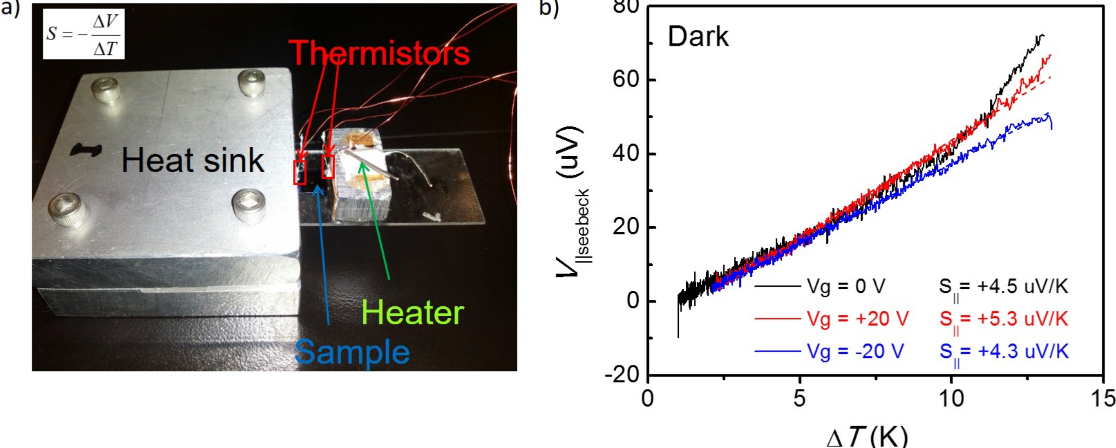

Figure 3.4. (a) Microprobe Seebeck measurement set-up compatible with probe-station measurement. (b) Average longitudinal Seebeck coefficient of 20 μm wide aligned p-type SWCNT stripes under different gate voltages. The results show that $S_{||}$ does not depend on gate voltage in the range of −20 V to 20 V.

Higher gate voltage has been tested but irreversible damage to the 100 nm thick SiO_2 insulting layer was caused. The p-type conducting channel does not pinch off at large positive gate bias up to + 20 V, and that may be due to the fact that the stripe thickness is 10 times greater than the diameter of individual nanotubes, resulting in a much larger threshold voltage. To get n-type conductance, even larger gate voltage is needed. That requires a much thicker SiO_2 layer, which reduces the gate field strength. As a result, gate field modulation seems not to be a good option for tuning the p-type SWCNT stripes to n-type, unless thinner aligned CNT stripes are fabricated, which might be realized by adjusting the surfactant and CNT concentration in EDSA.

The effect of gate-field modulation is also illustrated by the longitudinal Seebeck measurement at different gate voltages as shown in Fig. 3.4(b). The average longitudinal

Seebeck coefficient $S_{||}$ of the SWCNT stripes with stripe width around 5~7 μm is measured with a home-made thin film Seebeck measurement module which is compatible with probe stations (Fig. 3.4a). A temperature difference up to 15 K is applied to the two ends of the stripe, and the slope of the longitudinal Seebeck voltage with respect to temperature difference represents $S_{||}$ at room temperature (Fig. 3.4b). The positive sign of $S_{||}$ confirms the *p*-type nature of the as-grown SWCNTs. No obvious change of $S_{||}$ is observed when gate voltage sweeps from -20 V to + 20 V, indicating that the dominating carrier type of the conducting channel remains *p*-type.

II) Post-alignment chemical and electrochemical doping

In addition to the gate-field modulation, other doping schemes which require post-alignment chemical or electrochemical treatment have also been attempted. Typical *n*-type chemical doping of CNTs with alkali metals is achieved under a vacuum environment, but such chemically doped CNTs are unstable in air. There are several chemical or electrochemical methods demonstrated for the production of air-stable *n*-type CNTs, including physical adsorption of polymers containing electron-donating groups such as poly(ethyleneimine)(PEI) [80–82], use of metal contacts with low work functions [83], application of viologens for a direct redox reactions [84], and deposition of a high-κ oxide passivation layer to prevent oxygen doping [85]. Considering the solution used for alignment might affect the doping efficiency, post-alignment treatment is preferred. For post-alignment treating the adsorption of PEI may be limited to the top surface of CNT stripes and the low work function metal contacts are also only in touch with the top surface; thus we adopt the latter two methods to fabricate *n*-dope aligned CNT stripes.

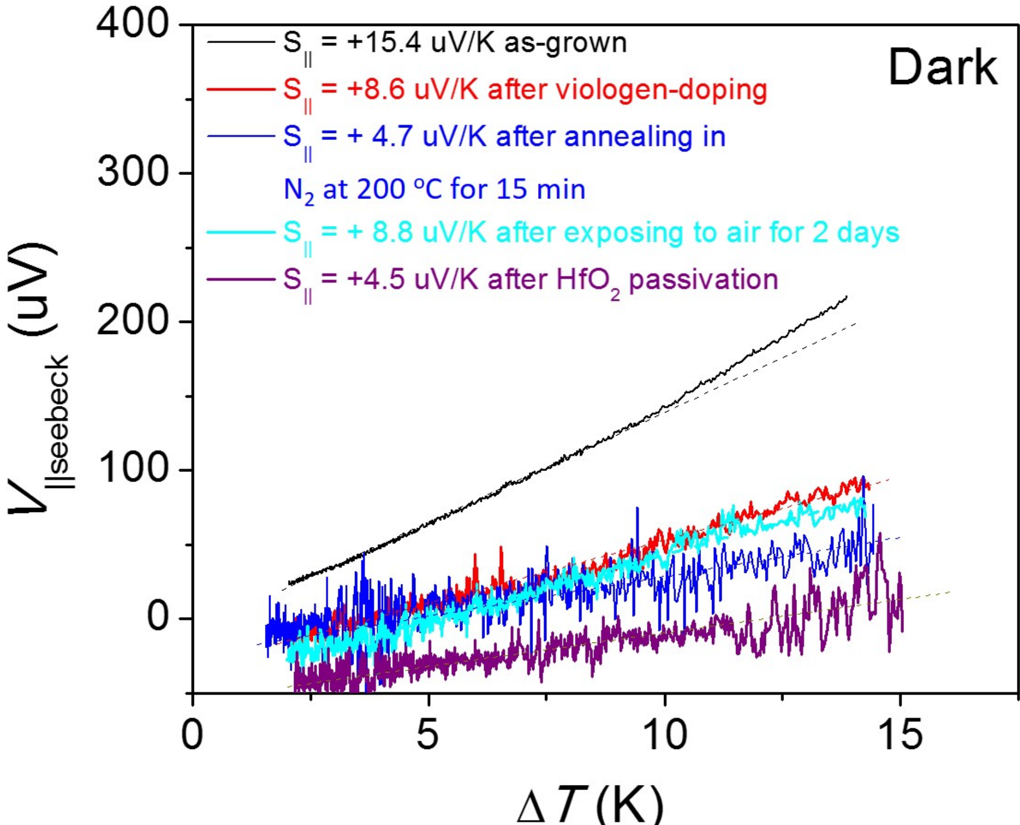

Figure 3.5. Longitudinal Seebeck coefficient $S_{||}$ measurement for nominally n-doped aligned CNT stripes of width around 5-7 μm. The as-grown CNT stripes (black) show p-type Seebeck coefficient + 15.4 μV/K, which decreases after viologen-doping (red) and decreases further after annealing (blue) since the annealing assists the dopant diffusion and oxygen desorption. However, the Seebeck coefficient remains p-type. After exposing to air for 48 hours the Seebeck coefficient recovers to the value before annealing (cyan), indicating the original "n-doping" effect was air-stable within this time scale while the annealing effect disappeared. Another attempt of n-doping with HfO_2 dissipation layer (purple) shows similar reduced p-type $S_{||}$.

Chemical doping of aligned SWCNT stripes with viologens via direct redox reactions reduces the p-type Seebeck coefficient of as-grown CNT stripes, but cannot produce air-stable n-type conduction. Neutral viologen solution is separated from charged viologen solutions by using a reducing agent of sodium borohydride, and then the solution is dropped onto the aligned as-grown SWCNT stripes to donate the electrons to CNTs. This method has been demonstrated to successfully transform CNT-thin film transistors (CNT-TFTs) from p-type to n-type, with remarkable stability sustained in both air and water [**84**]. As shown in Fig. 3.5, the longitudinal Seebeck coefficient of the SWCNT stripes drops from $+15.4\,\mu V/K$ to $+8.6\,\mu V/K$ after viologen doping, indicating that part of the SWCNTs are successfully transformed to n-type, while the overall conduction is still dominated by the remaining p-type CNTs. This might be due to the relative large stripe thickness ($\sim$ 20 nm) and the large density of the CNTs in our aligned stripes compared with the random network of CNTs grown by water plasma chemical vapor deposition (CVD) as reported [**84**].

Another electrochemical n-doping approach with a HfO_2 dissipation layer deposited onto CNT stripes using atomic layer deposition (ALD) is also tested. This method should work in principle in two aspects to converting the pristine p-type CNTs to n-type. First, the annealing in the vacuum chamber during the ALD process should desorb the oxygen atoms near the nanotube surface, making the nanotube more intrinsic. This effect is demonstrated by the drop of longitudinal Seebeck coefficient from $+8.6\,\mu\mathrm{V/K}$ to $+4.7\,\mu\mathrm{V/K}$ after annealing and restoration to $+8.8\,\mu\mathrm{V/K}$ after exposing to air for two days (Fig. 3.5). The Seebeck coefficient does not drop further, which might be because the desorption of oxygen atoms is not complete due to the relatively high density of the CNTs

in the stripes. Second, the deposited HfO_2 layer should prevent the oxygen absorption and the positive fixed charges near the CNT/HfO_2 interface, which are introduced by the deficiency of oxygen atoms in HfO_2, should bend the energy band of electrons in CNTs downward and function as an inherent positive gate voltage, shifting the conduction at zero gate bias toward n-type. However, similar to the gate-field modulation, the effect of the positive fixed charge in the HfO_2 layer is not obvious, with longitudinal Seebeck coefficient only dropping by 0.2 μV/K after HfO_2 doping (Fig. 3.5 blue and purple curve comparison).

The post-alignment doping attempts fail to transform all the SWCNT stripes from p-type to n-type, which may be caused by the dense structure of the twisted CNT bundles in the relatively thick SWCNT stripes. The diffusion of viologen in chemical doping and the electrical modulation by gate voltage or the positive fixed charges in the oxide layer are both limited to the CNTs near the top surface of the stripes. Pre-alignment doping might prove to be a better option for n-type doping of aligned CNT stripes or thin films. However, the stability of the doping during the solution-based alignment procedures will be a challenge.

In summary, we have achieved functioning p-type as-grown SWCNT stripe array, with zero transverse conductivity $\sigma_{\perp} \sim 0$ and average longitudinal conductivity up to $\sigma_{\parallel} \sim 4 \times 10^3$ S/m. However, attempts for n-type air-stable stripes fabrication including gate-field modulation, chemical doping, and electrochemical doping after alignment are not successful. p-type CNT thin films formed by aligned stripes fabricated via EDSA can have extremely large in-plane conductivity anisotropy ratio, and can be combined with other n-type anisotropic thin film semiconductors to form advanced device structures.

3.2. 3D-printed graphene-polymer stripes

Three-dimensional printed graphene (3DG), is a combination of 3D polymer printing which serves as a matrix, and interspersed graphene flakes. 3DG has recently invoked new interests in both acdemia [86–88] and industry. The direct writing technique of 3D printing uses viscoelastic liquid material ink made of molten or water solution [86, 87] of graphene/polymer mixture, which quickly solidifies after extrusion and can be deposited layer by layer to form 3D objects. However, the polymer component can deteriorate the desired intrinsic properties of graphene. High graphene content ink (60 vol%) [87] has shown better electrical performance compared with other graphene [86, 88] or carbon-based 3D conductive ink [89, 90], and is promising for flexible electronics and 3D electronics.

This section studies the anisotropic electrical transport properties of aligned 3DG stripes. The electrical conductivity of the high content 3DG has been previously characterized at room temperature for different particle loadings, annealing temperatures, tip diameters, strain and bending cycles [87]. The results fit well with the shear-induced flake alignment model, indicating that each printed fiber can have anisotropic properties between the directions along and transverse to the fiber. Since each layer is formed by multiple fibers stitching together, the thin film is expected to exhibit overall anisotropic conductivity. In this Section, transport properties such as the conduction mechanism, the carrier type, and the temperature dependence are studied to help achieve a better understanding and further optimization of the electrical properties of 3DG.

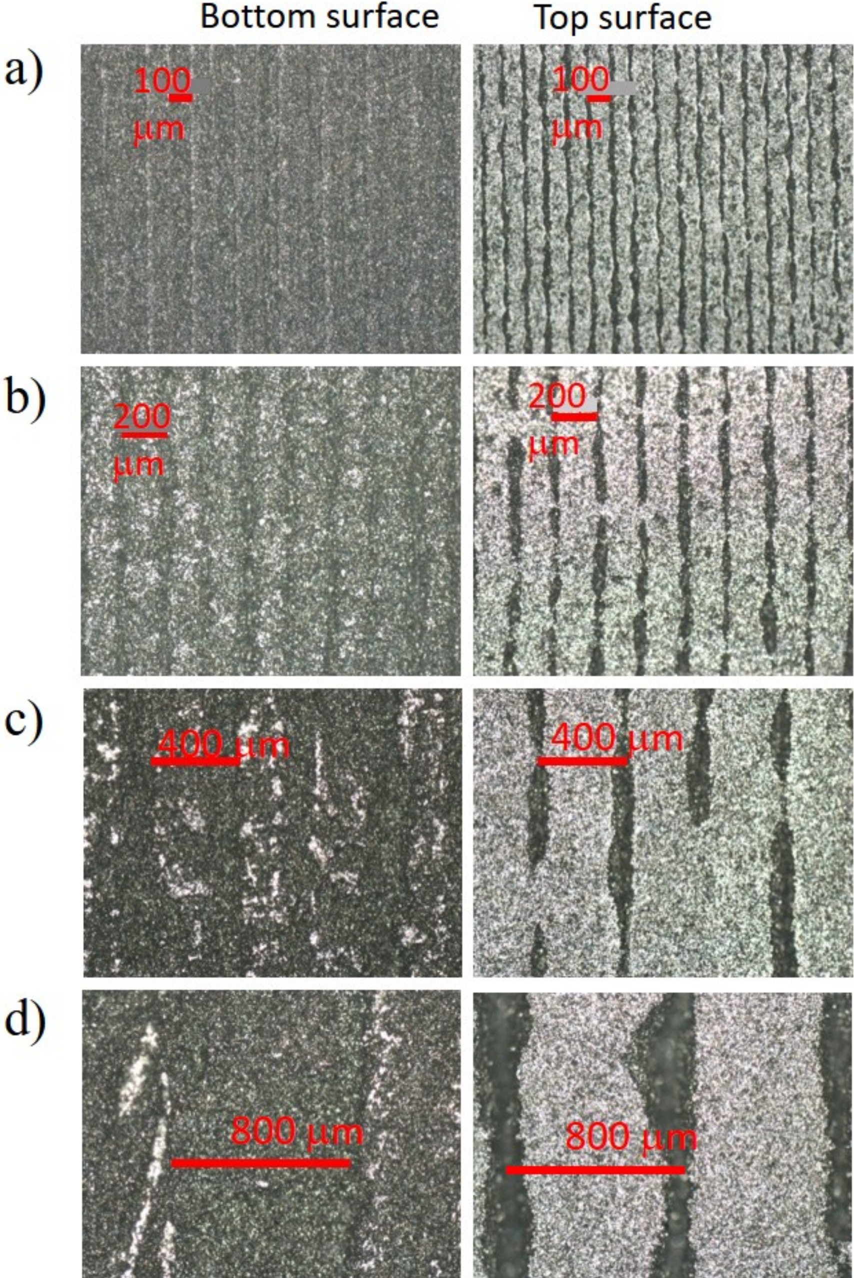

Figure 3.6. The bottom and top surfaces of 3DG thin films printed with nozzle diameter (a) $D = 100$ μm, (b) $D = 200$ μm, (c) $D = 400$ μm and (d) $D = 800$ μm. The stripe width of the printed film is roughly equal to the nozzle diameter. The top surface is corrugated, and the width of the grooves between adjacent stripes increases with the nozzle diameter D.

3.2.1. Aligned 3DG stripes preparation

Single-layer thin films of aligned 3DG stripes are printed using the three-dimensional printing technology with various nozzle diameters. The 3DG ink with 60 vol% graphene used in this study is the same as the one in Ref. [87]. Aligned fibers are printed and closely stitched together to form a single layer thin film with nozzle diameters $D = 100, 200, 400$ and 800 μm. As shown in Fig. 3.6, the stripe width is roughly consistent with the nozzle diameter.

Different surface roughnesses are observed for the top and bottom surfaces of the printed 3DG thin films. The bottom surfaces are relatively smooth, with the adjacent stripes closely stitched together to form a continuous flat surface, as shown in the left column of Fig. 3.6. The top surfaces, on the contrary, have gaps between neighboring stripes, as shown in the right column, and thus have a larger roughness. Figure 3.7 compares the top and bottom surface roughness profiles. The depth of the deepest valley R_v of the top surface is much larger than that of the bottom surface. However, it is still within 25% of the film thickness t, which is consistent with the fact that the gaps do not penetrate the thin films.

The roughness difference of top and bottom surfaces can be attributed to ink spreading before it dries. The bottom interface of the thin films should be in direct contact with the glass slide substrate during the printing. The ink spreads horizontally before solidifying, resulting in a film thickness t less than 50% of the nozzle diameter (Fig. 3.7), and also a relatively smooth bottom surface. The spreading of the 3DG ink will reduce the anisotropy of the 3DG stripe arrays. In the extreme case, the ink spreads fast enough to form a continuous, isotropic thin film, and the stripes will not be able to be observed. The fact

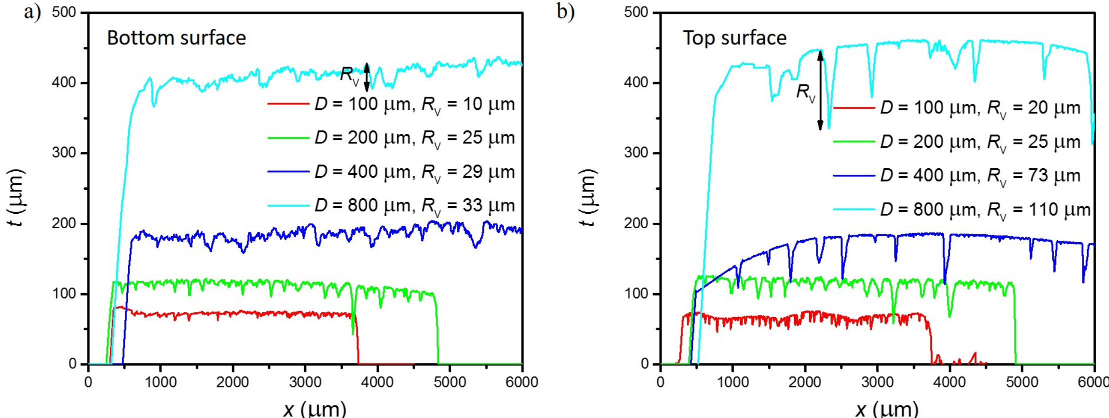

Figure 3.7. The (a) bottom and (b) top surface profile of 3DG films printed with nozzle diameters D = 100, 200, 400 and 800 µm. The film thickness t is typically around half of D, due to the ink spreading before drying up. The top surface shows a much larger roughness compared with the bottom surface, as indicated by the depth of the deepest valley R_v in the figure legend.

that the stripes can be clearly observed and that the top surfaces have gaps, indicate the extent of the ink spreading.

3.2.2. Characterization method

To measure the conductivity anisotropy and magneto-transport properties of these thin films, square samples with dimension 5×5 mm^2 are cut, and eight silver paste contacts are placed at the corners and center of edges. The silver paste contacts are made in a way that the edge of the thin film is entirely covered in the vertical direction to minimize measurement error. The samples are measured with lock-in amplifiers in a cryostat that provides the capabilities of temperature sweep ($T = 2 \sim 300$ K) and magnetic field sweep ($B = 0 \sim 5$ T).

Configuration	$A_R = R_{AD,BC}/R_{AB,DC}$	$A_\rho = \rho_{yy} / \rho_{xx}$
a)	9.903	2.03
b)	68.14	2.05
c)	65.06	2.02
d)	1.163	N/A
e)	0.506	1.86
f)	0.691	2.11

Figure 3.8. The anisotropic van der Pauw measurement contact configurations and results for the 3DG film printed with nozzle diameter $D = 100$ μm, measured at $T = 300$ K. The resistance anisotropy $A_R = R_{AD,BC}/R_{AB,DC}$ is measured for different combinations of the four contacts, and the resistivity anisotropy $A_\rho = \rho_{yy}/\rho_{xx}$ is calculated via anisotropic scaling and conformal mapping. The consistency in A_ρ of different configurations indicate the validity of the anisotropic van der Pauw method. Note for four edge center contacts in (d), $A_R = 1$ is expected independent of A_ρ. The deviation from 1 can be partially attributed to the contact displacement.

The resistivity or conductivity anisotropy of the 3DG thin films is measured with the anisotropic van der Pauw method [91]. The 3DG films have known principal axes of the anisotropic conductivities, *i.e.*, the longitudinal direction x along the stripes, and the transverse direction y perpendicular to the stripes, thus the in-plane resistivity can be

represented by a diagonalized tensor

$$\boldsymbol{\rho} = \begin{bmatrix} \rho_{xx} & 0 \\ 0 & \rho_{yy} \end{bmatrix}. \tag{3.1}$$

With known resistivity anisotropy $A_\rho = \rho_{yy}/\rho_{xx}$, the anisotropic, square sample can be scaled with a coordinate transformation to an isotropic, rectangular equivalent sample, which can be further transformed into the upper half plane with a conformal map, as shown in Section 2.2.1. Thus any four point contacts A, B, C, D on the sample periphery used for the conventional van der Pauw method will be mapped into four positions on the real axis of the upper half plane, from which the corresponding four-point resistance ratio can be readily calculated. Inverting this process, the resistivity anisotropy and the resistivity tensor components can be extracted from the measured van der Pauw resistance anisotropy.

The consistency of the resistance anisotropy is checked with the anisotropic van der Pauw method , using various combinations of contact configurations. Strictly speaking, the van der Pauw method can only be used for homogeneous and uniform resistive layers. The 3DG films are not perfectly uniform electrically conducting layers due to contact resistance between adjacent stripes and different width and depth of the gap between stripes. But as long as the number of strips is large within the area that is measured, the layer can be effectively approximated as an homogenoeus anisotropic conductor. Fig. 3.8 shows that the resistivity anisotropy A_ρ extracted from the van der Pauw resistance anisotropy A_R measured with different contact configurations are highly consistent. Note for Fig. 3.8(d), the resistance ratio is expected to be $A_R = 1$ regardless of the resistivity

anisotropy A_ρ, and achieves this value to within 16%. However this orientation cannot be used to deduce A_ρ. The deviations in the measured A_R values may be attributed to the finite size of the contacts, as well as geometric displacement of the point contacts away from the edge centers.

3.2.3. Results and discussion

Conductivity anisotropy and temperature dependence

The anisotropic resistivity of the 3DG thin film samples is measured in a temperature range from T = 300 K down to 4 K (Fig. 3.9a). The measured room temperature resistivity along the fiber direction (x-direction) is $\rho_{xx} \sim$ 0.2 - 0.3 Ω·cm, consistent with the longitudinal resistivity measured with open-mesh cylinders [**87**]. For all samples, the longitudinal resistivity along the x-direction (ρ_{xx}) is smaller than the transverse resistivity in the y-direction (ρ_{yy}), which is also consistent with the shear-induced flake alignment description demonstrated in Ref. [**87**]. The reorientation and alignment of the graphene flakes along the direction of flow, *i.e.*, x-direction, leads to fewer graphene/polymer junctions on the conduction path compared with the transverse direction, and thus smaller resistivity in the longitudinal direction than the transverse direction.

The resistivity anisotropy ratio $A = \rho_{yy}/\rho_{xx}$ shows negligible temperature dependence. As shown in Fig. 3.9(b), the resistivity anisotropy ratios are almost constant ranging from $A_\rho \sim$ 1.8 - 2.3 for varied nozzle diameters. One exception is the 3DG film printed with the nozzle diameter D = 800 μm, which has a 20% decrease in the transverse resistivity ρ_{yy} as the temperature decreases from 300 K to 140 K, while the longitudinal resistivity ρ_{xx} maintains a nearly constant value. This behavior may be attributed to the wide and deep

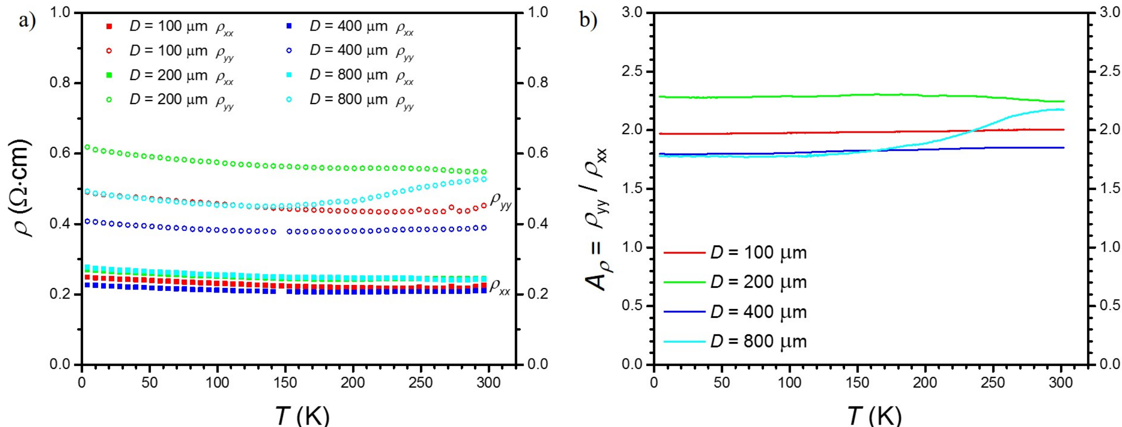

Figure 3.9. The temperature dependence of (a) the anisotropic resistivity components ρ_{xx}, ρ_{yy} and (b) their ratio $A_\rho = \rho_{yy}/\rho_{xx}$ for 3DG thin films printed with different nozzle diameter D. Both ρ_{xx} and ρ_{yy} slightly increase as the temperature decreases from $T = 300$ K to 4 K, except for ρ_{yy} for the thin film with nozzle diameter $D = 800$ μm, which reduces by about 15% when the temperature decreases from $T = 300$ K to 140 K. The resistivity anisotropy ratio is robustly temperature independent for most samples, with the exception described above for the $D = 800$ μm at higher temperatures.

gaps between stripes for the $D = 800$ μm sample. As the temperature decreases, the film may contract, possibly, reducing the gap width and enhancing the transverse conductivity, while the longitudinal direction is not much affected. For other samples that have smaller gap width and depth, or for the $D = 800$ μm sample at a temperature below 140 K, the small gap may be not blocking the transverse conduction, thus ρ_{yy} exhibits similar temperature dependence to ρ_{xx}.

There is no clear relation between the nozzle diameter D and the resistivity anisotropy $A_\rho = \rho_{yy}/\rho_{xx}$. As shown in Fig. 3.9 (b), the $D = 200$ μm sample has the maximum resistivity anisotropy $A_\rho = 2.3$, while the $D = 400$ and $D = 800$ μm samples share the same minimum resistivity anisotropy $A_\rho = 1.8$. This seems to contradict the shear-induced

alignment model, which predicts that the graphene flakes are aligned near the tip wall and not aligned near the center; the volume ratio of the aligned graphene/polymer flakes would be expected to decrease with increasing nozzle diameter, leading to a decreasing resistivity anisotropy ratio. The inconsistency may be attributed to the ink spreading and the gap formed between stripes, as well as possible use of different pressures and flow rates for the different nozzle diameters.

The resistivities of the printed 3DG films show unconventional behavior with only weak temperature dependence. As shown in Fig. 3.9(a), the resistivity increases by less than 15% when temperature decreases from 300 K to 4 K. To better understand the temperature dependence, the corresponding anisotropic conductivities $\sigma_{xx} = 1/\rho_{xx}$ and $\sigma_{yy} = 1/\rho_{yy}$ are calculated and fitted with different models. According to the fitting, the electrical conductivity of printed 3DG films cannot be explained by the thermally activated conductivity or the variable range hopping conductivity [**92**]. Instead, the vast amount of interconnects among graphene flakes, separated by the dielectric barrier in the graphene/polymer composite, may lead to a conductivity that is mainly stipulated by the fluctuation-induced tunneling of charge carriers through the contact junctions [**93**].

Fluctuation-induced tunneling conduction is a conduction mechanism present in disordered systems formed by large conducting regions separated by small insulating barriers [**93**]. In these systems, the overall conduction is dominated by the charge transfer across the insulating gaps. Thermal fluctuations can cause excess or deficit charge to build up on the junction faces, creating a strong local electric field due to the small junction width of the conducting regions at the junction. The thermal fluctuation and associated

local electric field change will affect the tunneling conductivity through the potential barrier at the junction and introduce a temperature dependence that deviates from both the simple activation model and the variable range hopping model.

With an approximated parabolic potential barrier [**94**], the conductivity dependence on the temperature of 3DG films can be expressed as [**93**]:

$$\sigma = \sigma_0 \exp\left(-\frac{T_1}{T + T_0}\right), \tag{3.2}$$

where σ_0 is a parameter that depends only weakly on temperature, and T_1 and T_0 are material dependent characteristic temperatures defined as [**95**, **96**]:

$$T_1 = \frac{8\varepsilon_0}{e^2 k_B}\left(\frac{AV_0^2}{w}\right), \tag{3.3}$$

and

$$T_0 = \frac{16\varepsilon_0 \hbar}{\pi(2m)^{1/2} e^2 k_B}\left(\frac{AV_0^{3/2}}{w^2}\right), \tag{3.4}$$

where ε_0 is the vacuum permittivity, $2\pi\hbar$ the Planck's constant, m the carrier mass, e the electron charge, A the surface area of the tunneling junction, w the potential barrier width and V_0 the potential barrier height. When the carrier mass m and potential barrier height V_0 are known, the potential barrier width w can be calculated from the ratio of T_0 and T_1:

$$w = \frac{T_1}{T_0}\frac{2}{\pi\chi}. \tag{3.5}$$

Here χ is the tunneling constant defined by $\chi = \sqrt{2mV_0}/\hbar$.

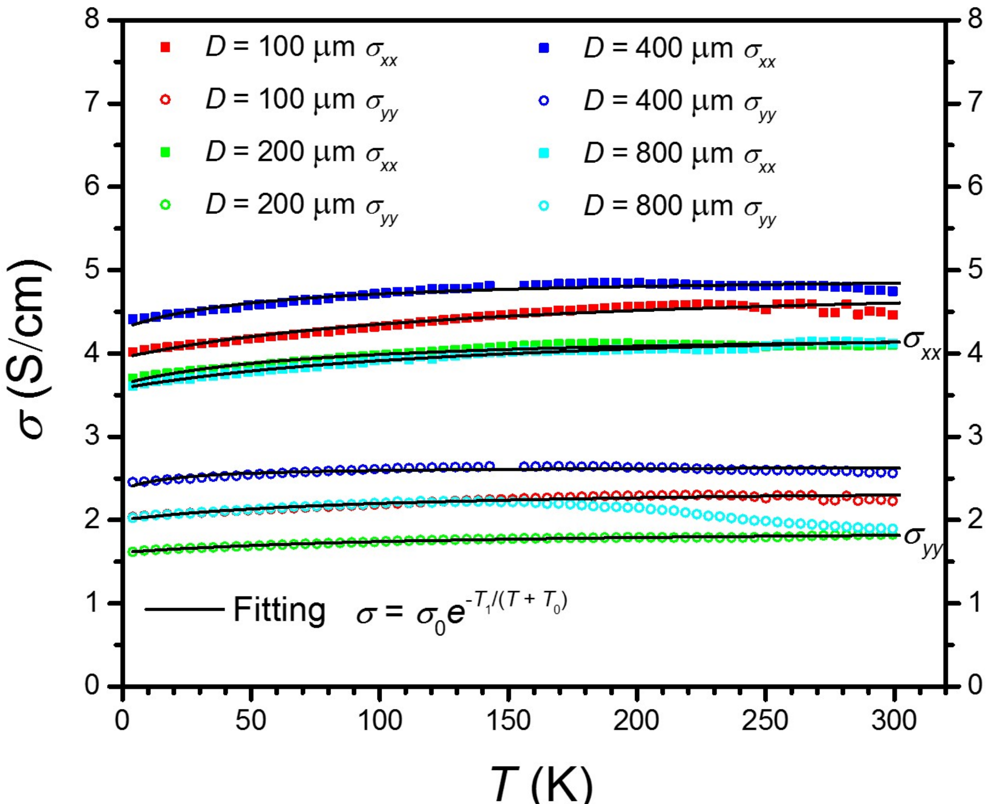

Figure 3.10. The anisotropic conductivities versus temperature fitted by fluctuation-induced tunneling model for 3DG thin films printed with different nozzle diameter D. The median value of the tunneling junction width w is proportional to the ratio T_1/T_0. Note for the $D = 800$ μm sample, only the lower half of the temperature range ($T = 4$ K to 140 K) is fitted.

Figure 3.10 shows that the anisotropic conductivities for samples printed with varied nozzle diameters are well fitted by the fluctuation-induced tunneling conduction model, with the three fitting parameters σ_0, T_1 and T_0 listed in Table 3.1. Since we do not have the data to observe the distribution of tunneling junction parameters, the fitted parameters should be interpreted as an indicative of the median values of these parameters.

According to Eq. (3.5), the median value of the junction width w is proportional to the ratio T_1/T_0. Table 3.1 shows that the fitted ratio T_1/T_0 for longitudinal and transverse conductivities of each sample are consistent. The similar ratio indicates the samples have similar median junction width in the longitudinal and transverse directions, which is physically reasonable and can be regarded as supporting evidence of the fluctuation-induced tunneling conduction in the measured 3DG films. More information about the hole effective mass in the majority graphene and the molecular orbital energies of the minority polylactide-co-glycolide of the liquid ink used are needed to determine the accurate values of the junction width.

Table 3.1. The fluctuation-induced tunneling model fitting parameters for the temperature dependent anisotropic conductivities in Fig. 3.10.

		σ_0 (S/cm)	T_0 (K)	T_1 (K)	T_1/T_0
$D = 100$ µm	σ_{xx}	4.91	124	27.0	0.22
	σ_{yy}	2.40	94.6	17.3	0.18
$D = 200$ µm	σ_{xx}	4.26	72.0	11.5	0.12
	σ_{yy}	1.90	111	18.5	0.17
$D = 400$ µm	σ_{xx}	4.95	51.9	7.26	0.14
	σ_{yy}	2.64	19.5	2.16	0.11
$D = 800$ µm	σ_{xx}	4.42	137	28.8	0.21
	σ_{yy}	2.37	92.2	15.3	0.17

Magnetotransport properties

Mixed n- and p-type conduction with p-type dominating is observed in the printed 3DG films in the magnetotransport characterization. The Hall effect and the magnetoresistance measurement have been performed in a continuously varying magnetic field perpendicular to the thin film surface, with the maximum field strength up to $B_{\max} = 5$ T. Electric

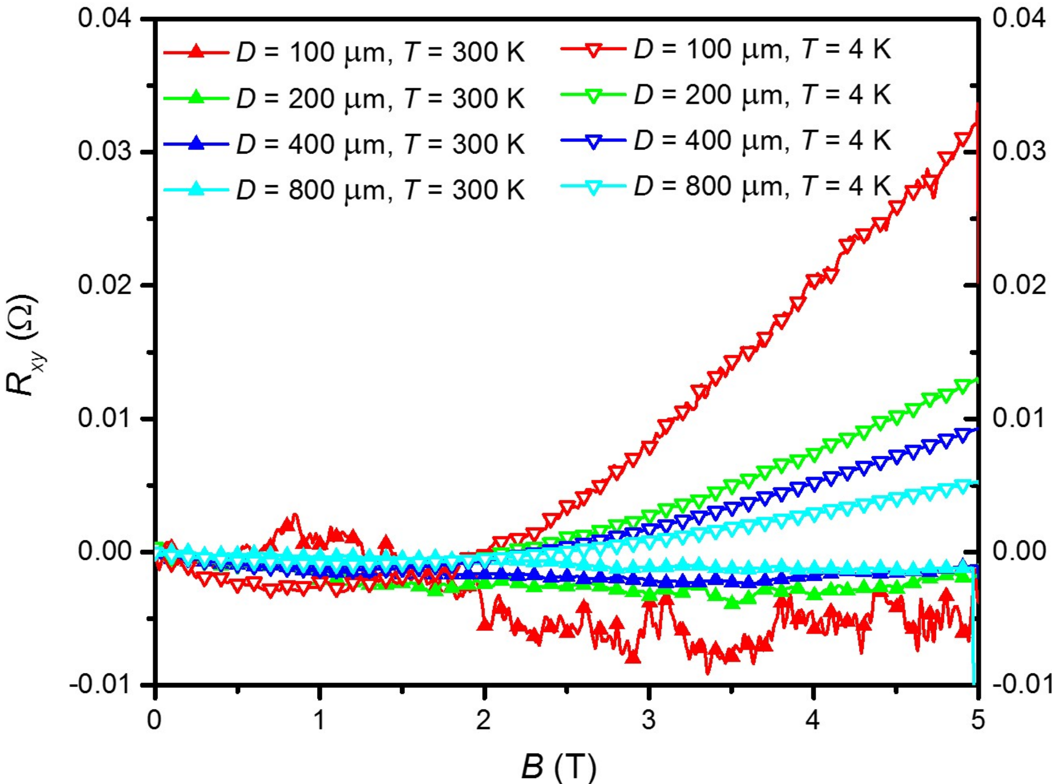

Figure 3.11. The Hall resistance R_{xy} measured at $T = 300$ K and $T = 4$ K for 3DG films printed with varied nozzle diameter D. At 300 K, R_{xy} is smaller than the noise level due to the high carrier concentration. At 4 K, the overall positive slope of R_{xy} at large B indicates that p-type conduction dominates the electrical conduction of the 3DG films. However, the concavity at weak magnetic field can be evidence that n-type conduction of electrons also contribute to the total conduction. The larger amplitude of Hall resistance for thinner films with smaller D is mainly due to their smaller thickness.

transport properties including the predominant charge carrier type, carrier concentration, and mobility can, in principle, be extracted from the magnetotransport measurement results.

Figure 3.11 shows the Hall resistance R_{xy} dependence on the magnetic field strength at $T = 300$ K and $T = 4$ K for 3DG films printed with varied nozzle diameter D. At $T = 4$ K, all the curves are almost linear in the strong magnetic field ($B > 2.5$ T) with a positive slope, indicating that p-type conduction of holes dominates the overall electrical conduction. However, the concavity and negative R_{xy} in weak magnetic field ($B < 2$ T) reveals that there also exists mixed n-type conduction contributed by electrons, causing non-linear R_{xy} as B varies. The upper B-field bound for the concavity varies with the mobility of the minority n-type carriers and majority p-type carriers. At $T = 300$ K, the concavity covers the entire range of $B = 0$ - 5 T, and thus no slope or carrier density can be extracted.

Figure 3.12 shows the magnetoresistance along longitudinal (R_{xx}) and transverse directions (R_{yy}) for all samples measured at $T = 300$ K and $T = 4$ K. Both R_{xx} and R_{yy} slightly increases with B-field in a quasi-parabolic trend. The anisotropic resistance ratio R_{yy}/R_{xx} slightly decreases by 1 - 2% as B increases from 0 to 5 T. Note the resistance anisotropy A_R is different from the resistivity anisotropy $A_\rho = \rho_{yy}/\rho_{xx}$.

The mixed conduction of holes and electrons has been analyzed with the multi-carrier model [**97**] and Fourier-domain mobility spectrum analysis (FMSA) [**98**]. However, these Drude model based analysis technique cannot provide a proper fitting to all the conductivity tensor components, revealing their limitation in disordered systems whereby fluctuation-induced tunneling conduction dominates the overall conduction. A further theoretical study is needed to understand the Hall effect and magnetoresistance in such disordered systems with mixed conduction.

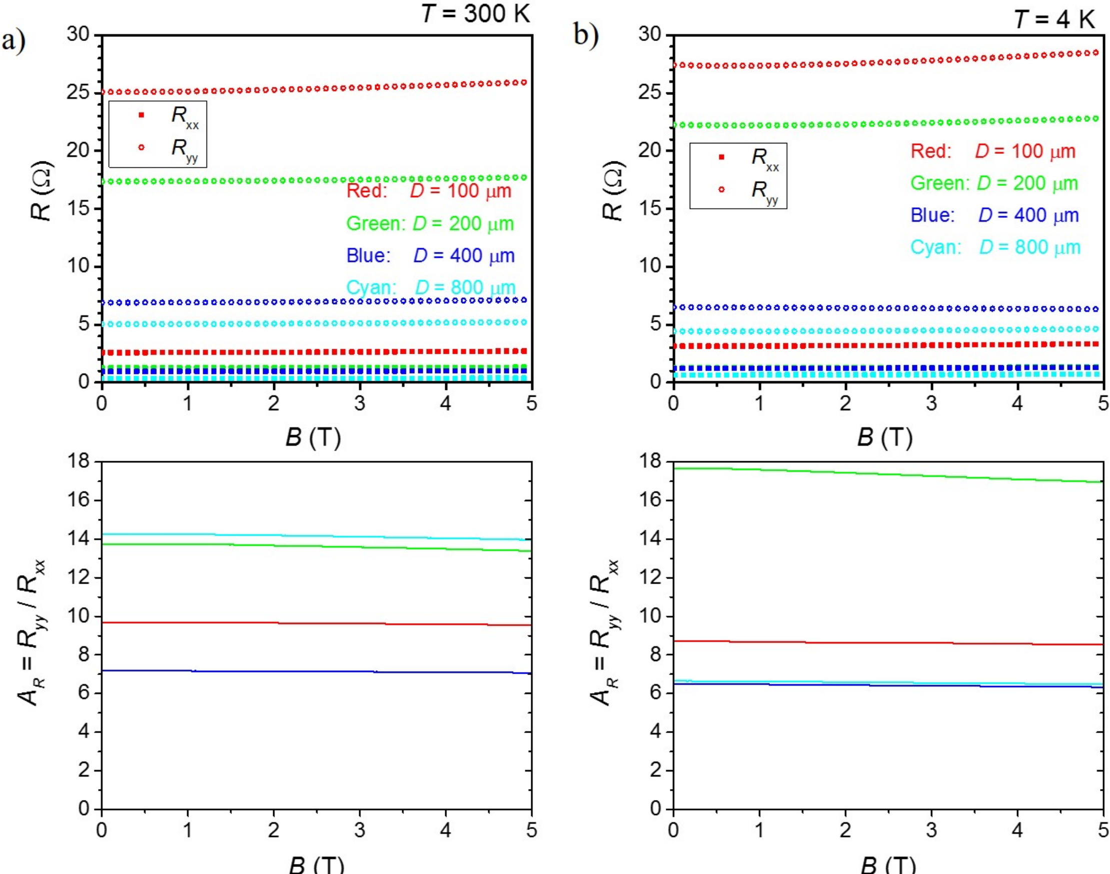

Figure 3.12. The magnetoresistance (top panels) along the longitudinal (R_{xx}, solid squares) and transverse directions (R_{yy}, open circles) for 3DG thin films printed with various nozzle diameters D and the measured resistance anisotropy $A_R = R_{yy}/R_{xx}$ (solid lines, bottom panels) at (a) $T = 300$ K and (b) $T = 4$ K. A_R only decreases by 1 - 2% as the magnetic field B increases from 0 T to 5 T. Note A_R is different from the resistivity anisotropy $A_\rho = \rho_{yy}/\rho_{xx}$.

A crude estimation of the effective hole density and mobility are obtained from the positive slope of R_{xy} in the strong magnetic field near $B = 5$ T and the conductivities at zero magnetic field. As shown in Table 3.2, the effective hole concentration is estimated to be around $6.5 \sim 9.5 \times 10^{19}$ cm^{-3} at $T = 4$ K. The corresponding hole mobilities in the

longitudinal and transverse directions for single-layer 3DG films exhibit a small amplitude in the order of 1 cm^2/Vs.

Table 3.2. The low temperature ($T = 4$ K) hole density p and anisotropic mobilities μ_x, μ_y estimated from the slope of R_{xy} near $B = 5$ T.

D (μm)	t (μm)	p (cm^{-3})	μ_x ($cm^2/V{\cdot}s$)	μ_y ($cm^2/V{\cdot}s$)
100	70	7.7E18	3.3	1.7
200	130	9.5E18	2.4	1.1
400	190	8.4E18	3.3	1.8
800	420	6.5E18	3.5	1.9

In summary, the conductivity of the 3DG films shows semiconductor behavior with a weak temperature dependence, which can be well fit by a fluctuation-induced tunneling conduction model. All the 3DG films printed with nozzle diameters $D = 100, 200, 400$ and 800 μm exhibit higher conductivity in the longitudinal direction than the transverse direction. The conductivity anisotropy ratio is measured to be temperature-independent, in the range of $A_\rho \sim= 1.8$ - 2.3, and appears to be independent of the nozzle diameter. The magnetotransport measurement reveals mixed conduction of electrons and holes with p-type conduction from holes dominating at high B. However, the classic Drude model-based parallel conduction analysis technique cannot explain the data well, so a further theoretical study on the disordered systems with fluctuation induced tunneling conduction dominating is needed to fully understand the magnetotransport of the 3DG thin films.

3.3. Ion implantation-induced anisotropy in semiconducting layers

This section demonstrates the synthesis of anisotropically conducting AlGaAs thin films with both n- and p-type conduction, by defining micron-scale parallel conduction

channel arrays using ion implantation isolation. Unlike CNTs and graphene-polymer composites which are *p*-type as-grown and difficult to maintain as *n*-type in air, bulk semiconductors can be conveniently doped to either *p*- or *n*-type, and the doping is stable in air, making them better candidates for *n*-type anisotropic conductors. AlGaAs is chosen as a representative of the conventional bulk semiconductors due to its moderately large Seebeck coefficient [**99**] for both *n* and *p* type materials, which are intended for thermoelectric applications that will be introduced in the next chapter.

The ion-implantation isolation technique is adopted to define the micron-scale conduction channel arrays that can achieve a large in-plane conductivity anisotropy. Ion implantation is an essential process for modern compound semiconductor devices and circuits, and has been proven to be an efficient and practical approach to isolate closely spaced devices [**100**] with selective masking of the semiconductor surface. The isolation results when free carriers are trapped by deep level centers formed by the implantation process. The conduction channels separated by implanted isolation regions will conduct only along the channel direction and are highly insulating in the direction transverse to the implanted channels. We fabricate 10 μm-wide proton-implanted channels separated by 10 um-wide conduction channels with an overall 20 μm pitch [**101**, **102**]. A conductivity anisotropy ratio up to 10^4 and a low longitudinal resistivity along the channel direction have been observed, leading to an AlGaAs thin film with significant in-plane conductivity anisotropy that can be doped either *n*-type or *p*-type. The work in this section is published has been SPIE conference proceedings [**103**].

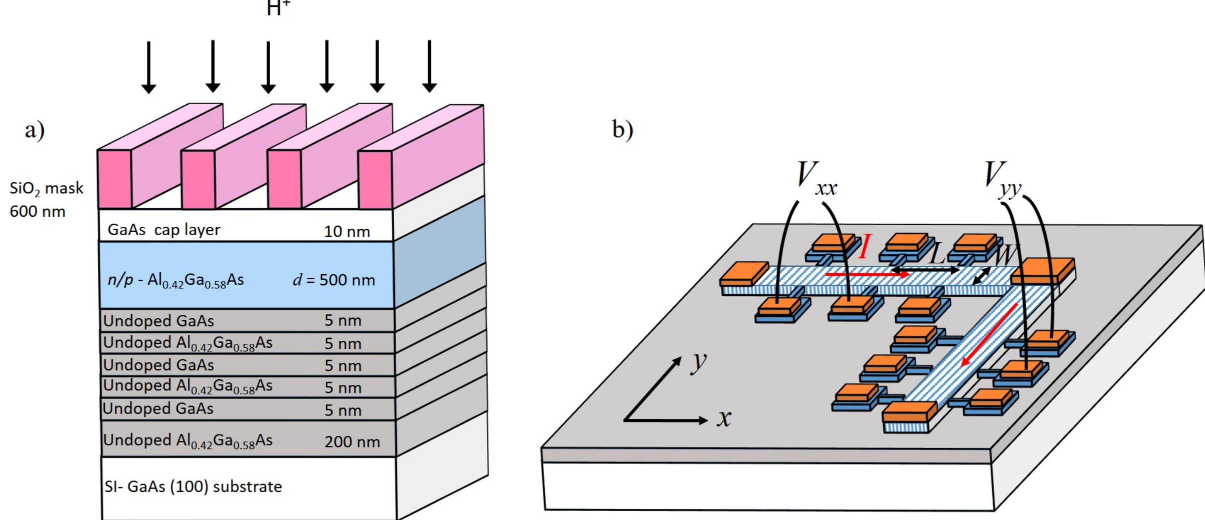

Figure 3.13. (a) Schematic of the $Al_{0.42}Ga_{0.58}As$ thin film and proton ion implantation. The doped $Al_{0.42}Ga_{0.58}As$ thin film is electrically isolated from the substrate with the GaAs/$Al_{0.42}Ga_{0.58}As$ superlattices. The SiO_2 mask layer is patterned into stripes by photolithography and wet etching, and defines the protected and damaged regions of $Al_{0.42}Ga_{0.58}As$ in proton (H^+) implantation. The strip width and separation between strips are both 10 μm. (b) The etched L-shaped Hall bar of ion-implanted $Al_{0.42}Ga_{0.58}As$ and resistance measurement set-up. An AC current I is sent through the Hall bar and the voltage drops V_{xx} and V_{yy} can be measured with the voltage contacts on the side, from which the transverse ($\rho_{\perp}$) and parallel ($\rho_{\parallel}$) resistivities to the ion-implanted strip direction can be determined.

3.3.1. Method

The synthesis consists of the thin film growth and the ion implantation isolation. The $Al_xGa_{1-x}As$ thin films are fabricated by molecular beam epitaxy (MBE) on a semi-insulating GaAs (100) substrate, undoped $Al_xGa_{1-x}As$ buffer layer and GaAs/$Al_xGa_{1-x}As$ superlattice electrical isolation layer, as shown in Fig. 3.13(a). The stoichiometric aluminum fraction $x = 0.42$ is chosen to maximize the Seebeck coefficient by approaching the 8-fold degeneracy among the Γ, X, and L valleys [99]. The $Al_{0.42}Ga_{0.58}As$ layer is then

doped with silicon ($N_D = 5 \times 10^{16}$ cm^{-3}) or carbon ($N_A = 1.5 \times 10^{18}$ cm^{-3}) to create the n-type or p-type layers, respectively. A thin GaAs cap layer is grown on the top surface to prevent oxidation in air. After the sample growth, a thick SiO_2-mask layer is grown by plasma-enhanced chemical vapor deposition (PECVD) and patterned into narrow parallel strips with photolithography and wet etching, whereby the strip width and separation are both 10 μm, leading to a 20 μm wide pitch. Proton implantation with energy $E = 50$ keV and dosage $D = 5 \times 10^{15}$ cm^{-2} is used to damage the crystal structure of the unprotected regions between neighboring SiO_2 strips, aiming to increase the resistivity transverse to the strip direction while preserving low resistivity along the strip direction.

After proton implantation and removal of the SiO_2-mask layer, $Al_{0.42}Ga_{0.58}As$ thin films are mesa etched into the L-shaped Hall bar pattern for resistivity characterization, as shown in Fig. 3.13(b). Metalization contacts are fabricated by thermal evaporation of Ni(5 nm)/Ge(25 nm)/Au(100 nm)/Ni(20 nm)/Au(100 nm) [**65**] or e-beam evaporation of Pt(5 nm)/Ti(5 nm)/Pt(30 nm)/Au(120 nm) [**104**] contacts for n-type or p-type AlGaAs, respectively. The n-type contacts are annealed at 430 °C for 5 minutes in 5% H_2: N_2 forming gas to ensure the ohmicity, while the p-type contacts are already ohmic as-deposited provided that the contacting area is protected by the SiO_2 mask layer during the proton implantation. To eliminate the effect of contact resistances, an AC four-point measurement is performed by applying an AC current I through the L-shaped Hall bar and measuring the voltage drop along (V_{yy}) and transverse (V_{xx}) to the implanted array of channels. The resistivity in two directions can be determined by $\rho_{\parallel} = GdV_{yy}/I$ and $\rho_{\perp} = GdV_{xx}/I$, where d is the thickness of the AlGaAs layer and $G = W/L$ the geometrical correction factor.

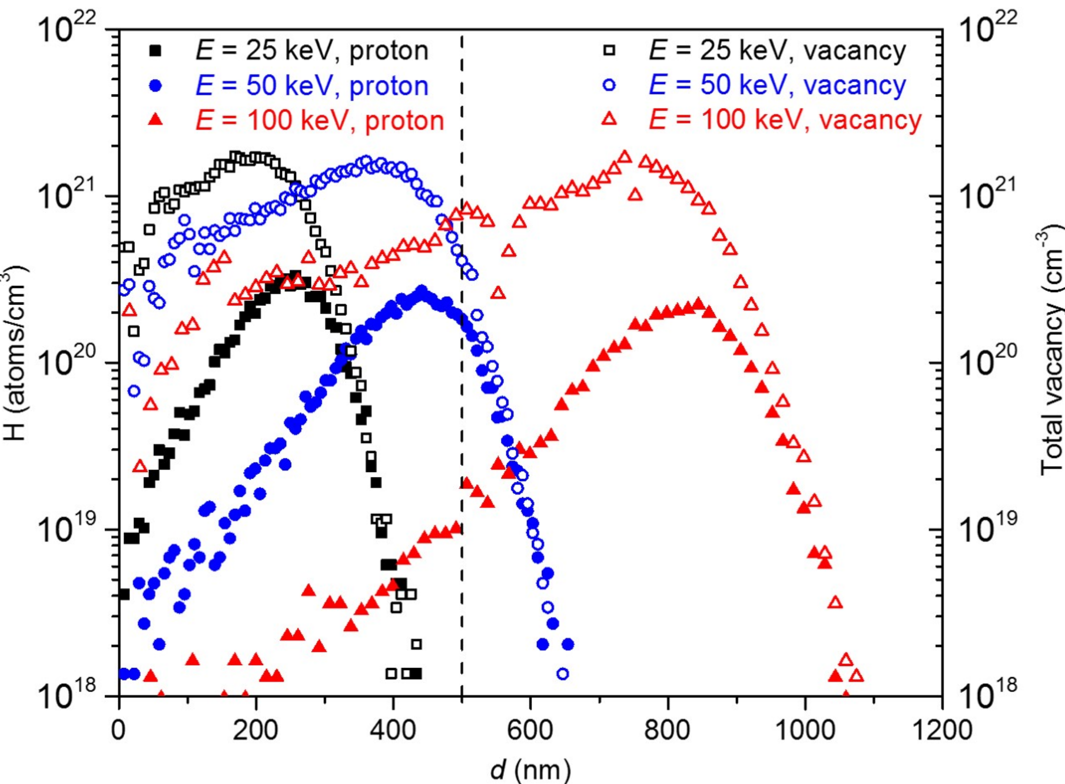

Figure 3.14. SRIM [9] simulated proton and vacancy defect profile for different proton energies when the $Al_{0.42}Ga_{0.58}As$ layer is 500 nm thick. The dosage used for this simulation is $D = 5 \times 10^{15}$ cm^{-2}.

3.3.2. Results and analysis

Proton implantation dosage and energy

The proton implantation dosage is chosen to maximize the resistivity of the isolation regions. Typically as the dosage increases, the implanted material resistivity will first increase, then saturate when the conduction is shorted by the highly resistive but nonetheless parallel conducting semi-insulating substrate, and then the resistivity will

again decrease when the defect concentration is high enough to permit hopping conduction [101, 102]. The optimal dosage within the resistance saturation plateau is proportional to the carrier concentration in the doped layer of interest [101]. The dosage $D = 5 \times 10^{15}$ cm^{-2} in this experiment is scaled from the reported optimal dosage by Lippen et al. [101] based on the carrier concentration and film thickness changes.

The stopping and range of ions in matter (SRIM) simulation [9] is used to determine the optimal proton implantation energy. The protons are known to create point defects including vacancies and interstitials in AlGaAs due to the low stopping power for protons. As shown in Fig. 3.14, the depths of the vacancy peak and proton peak are predicted to increase with proton energy while the peak amplitude remains almost the same. To maximize the transverse resistivity of the $Al_{0.42}Ga_{0.58}As$ layer, the largest average vacancy and proton density between $d = 0$ and $d = 500$ nm is needed. On the other hand, it is beneficial to minimize the defect density beyond $d = 500$ nm to avoid damaging the underlying layer and thus enable the fabrication of a multi-layer artificial anisotropic thin film. The optimal proton energy satisfying these two criteria is around $E = 50$ keV as observed from Fig. 3.14.

Proton distribution profile

The theoretical SRIM simulation of the proton distribution is compared to the experimental results measured by secondary ion mass spectrometry (SIMS) in Fig. 3.15. Two different samples are fabricated : a) as-grown p-type $Al_{0.42}Ga_{0.58}As$ ($N_A = 1.5 \times 10^{18}$ cm^{-3}) and b) annealed (430 °C, 5 minutes) n-type $Al_{0.42}Ga_{0.58}As$ ($N_D = 5 \times 10^{16}$ cm^{-3}). Since the doping density is much lower than the proton and vacancy peak density, the doping is not expected to affect the proton or vacancy distribution significantly. The

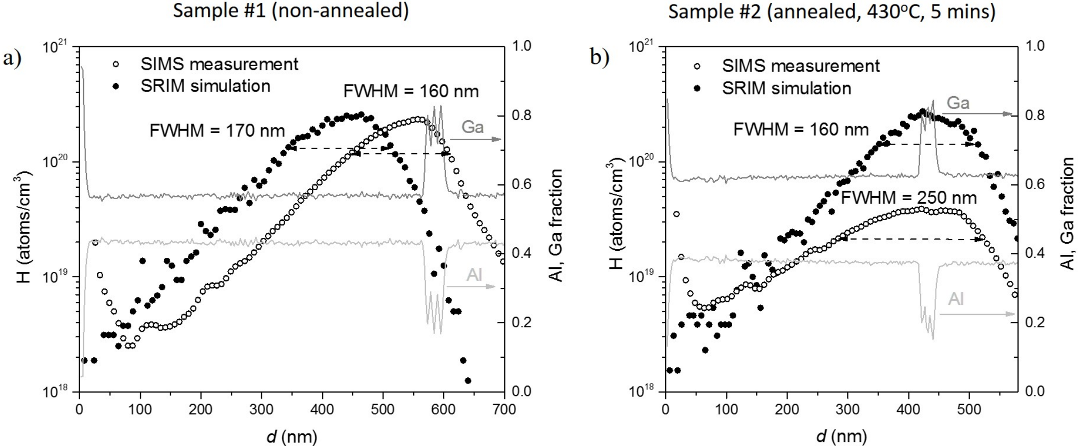

Figure 3.15. The SRIM simulation of the implanted proton distribution compared to SIMS measurement of (a) As-grown p-type doped $Al_{0.42}Ga_{0.58}As$ and (b) annealed n-type doped $Al_{0.42}Ga_{0.58}As$. The measured Al and Ga fraction peaks/valleys indicate the depth of the $GaAs/Al_{0.42}Ga_{0.58}As$ superlattice barrier below the doped $Al_{0.42}Ga_{0.58}As$ layer. The peak proton density agrees with simulation for the as-grown sample, and is smaller for the annealed one. Integration of the proton density over depth indicates that more than 50% of the implanted protons diffused towards the surface and more than 30% diffused out of the sample.

depth of the measured Ga and Al fraction peaks and valleys indicate deviations from the nominal thickness for the $Al_{0.42}Ga_{0.58}As$ layer, resulting in $d_p = 565$ nm and $d_n = 416$ nm, for the p- and n-type layers, respectively. From Fig. 3.15(a) we observe that the SIMS measured proton peak density and full-width at half-maximum (FWHM) agree well with the SRIM simulation results. The SIMS measured peak location is 100 nm deeper than the simulation, which may be caused by a small shift in the actual implantation energy.

The post-implantation anneal causes protons to spatially redistribute, resulting in a more dispersed and lower peak. As shown in Fig. 3.15(b), the measured proton peak density after anneal is only around 1/7 of the simulated value, and the measured FWHM

= 252 nm is 56% wider than the simulated 162 nm. The hydrogen peaks near the surface (d < 75 nm) are due to the hydrogen atoms adsorbed on the surface being driven into the sample by ion beams during SIMS, so only the hydrogen detected for $d > 75$ nm is due to proton implantation. The sheet density of implanted protons can be obtained by integrating the SIMS hydrogen density with depth for $d > 75$ nm, which is $H_{2D,\ \text{as-grown}} = 4.49 \times 10^{15}$ cm^{-2} for the as-grown sample a) and $H_{2D,\ \text{annealed}} = 1.87 \times 10^{15}$ cm^{-2} for the annealed sample b), respectively. We observe that the pre-anneal sheet density is close to the implantation dosage $D = 5 \times 10^{15}$ cm^{-2}, while after annealing only around 42% of implanted protons remain in depth $d > 75$ nm, with the remainder likely having diffused towards and even out of the surface. In spite of the large exodus of hydrogen ions from the implantation volume, there remains a large post-anneal resistance enhancement in the implanted regions, implying that the implantation process is sufficiently effective in increasing resistivity that the diffusion of H atoms and possibly even healing of some of the vacancy defects are nonetheless insufficient to restore the conductivity of the implanted regions.

Conductivity anisotropy

Table 3.3. The post-anneal resistivity and anisotropy ratio at $T = 300$ K.

	$\rho_\parallel$ ($\Omega\cdot$m)	$\rho_\perp$ ($\Omega\cdot$m)	$\rho_\perp/\rho_\parallel$
p-$Al_{0.42}Ga_{0.58}As$	3.0×10^{-3}	> 150	$> 5 \times 10^4$
n-$Al_{0.42}Ga_{0.58}As$	2.0×10^{-2}	> 200	$> 1 \times 10^4$

The post-anneal resistivity for the longitudinal (parallel to the channel arrays) and transverse (perpendicular to the channel arrays) directions at room temperature are shown in Table. 3.3. For the transverse direction, the sheet resistance may not represent the

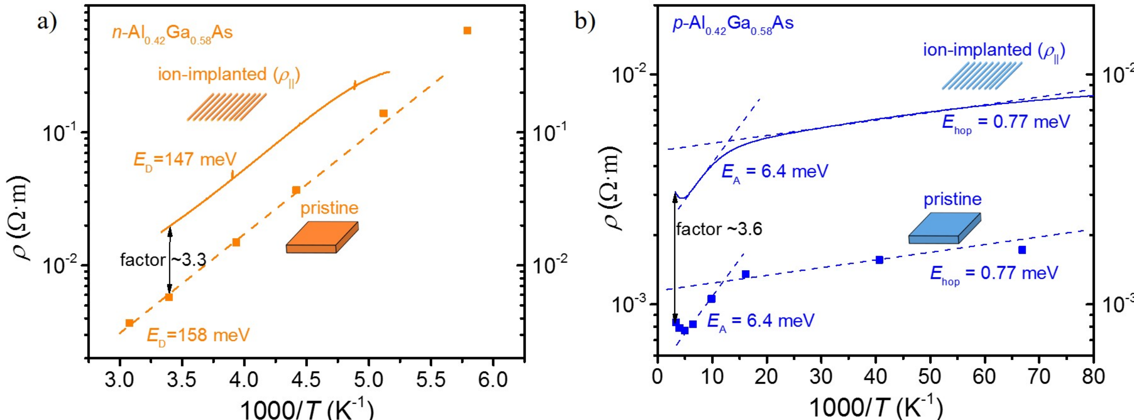

Figure 3.16. The temperature-dependent resistivity of pristine and ion-implanted (a) n-type and (b) p-type $Al_{0.42}Ga_{0.58}As$. For the ion-implanted samples, only the longitudinal resistivity along the conduction channel direction ($\rho_{\|}$) is plotted, the transverse resistivity ($\rho_{\perp}$) is at least four orders larger and cannot be accurately determined due to parallel conduction through the highly insulating substrate. The temperature ranges span from room temperature to the lowest temperature where contacts fail, which is around 200 K for n-type and lower than 10 K for p-type. The room temperature longitudinal resistivity increases only by a factor of 3.3 and 3.6 at room temperature after proton implantation and annealing, indicating that extreme conductance anisotropies can be realized by ion-implantation isolation.

conduction within the implanted AlGaAs layer, but instead is consistent with parallel conduction through the semi-insulating GaAs substrate, thus leading to a non-uniform resistance when choosing different voltage contact pairs. Here only the minimum value of the corresponding transverse resistivity is listed. The results show that the proton-implanted AlGaAs thin film has a reasonably small resistivity along the strip direction and orders of magnitude larger resistivity in the transverse direction, with a conductivity anisotropy ratio $\sigma_{\|}/\sigma_{\perp} = \rho_{\perp}/\rho_{\|} > 10^4$.

Further insight into the change of longitudinal resistivity after proton implantation is obtained by measuring the temperature dependence of the resistivity before and after the ion-implantation. Figure 3.16 shows that the longitudinal resistivity ($\rho_{\|}$) after proton-implantation has a similar temperature dependence to the pristine sample resistivity. The Arrhenius dependence of $\ln(\rho)$ vs $1/T$ for n-type $Al_{0.42}Ga_{0.58}As$ yields a donor binding energy of $E_D = 158$ meV and $E_D = 147$ meV before and after proton-implantation for silicon doping, which agree with previously published results, *e.g.* $E_D = 150$ meV for $Al_{0.36}Ga_{0.64}As$ [**105**]. The resistivity of p-type $Al_{0.42}Ga_{0.58}As$ first decreases with decreasing temperature, which can be attributed to temperature dependent phonon scattering [**106**], and then resistivity increases again as the temperature decreases below about 5 K. The two activation energies $E_A = 6.4$ meV and $E_{hop} = 0.77$ meV extracted from the two different slopes below 200 K are associated with the carbon acceptor binding energy and nearest-neighbor hopping gap respectively, and the values are consistent with previous reports $E_A = 7.8$ meV and $E_{hop} = 2.1$ meV [**107**].

After proton implantation and anneal, the longitudinal resistivity amplitude increases by a factor of 3.3 for n-type $Al_{0.42}Ga_{0.58}As$ and a factor of 3.6 for p-type $Al_{0.42}Ga_{0.58}As$. Such a small increase in longitudinal resistivity can be largely attributed to the decrease in the conduction channel width. The conducting channels and the separation between adjacent channels are both designed to be 10 μm wide, leading to an expected factor of 2 increase in $\rho_{\|}$. However, the actual undamaged conduction channel width will be even smaller due to the lateral spread and diffusion of the implanted protons and their associated vacancy and interstitial damage, thus leading to a resistivity increase by slightly more than the factor of 2. The Seebeck measurement of pristine and ion-implanted n-type

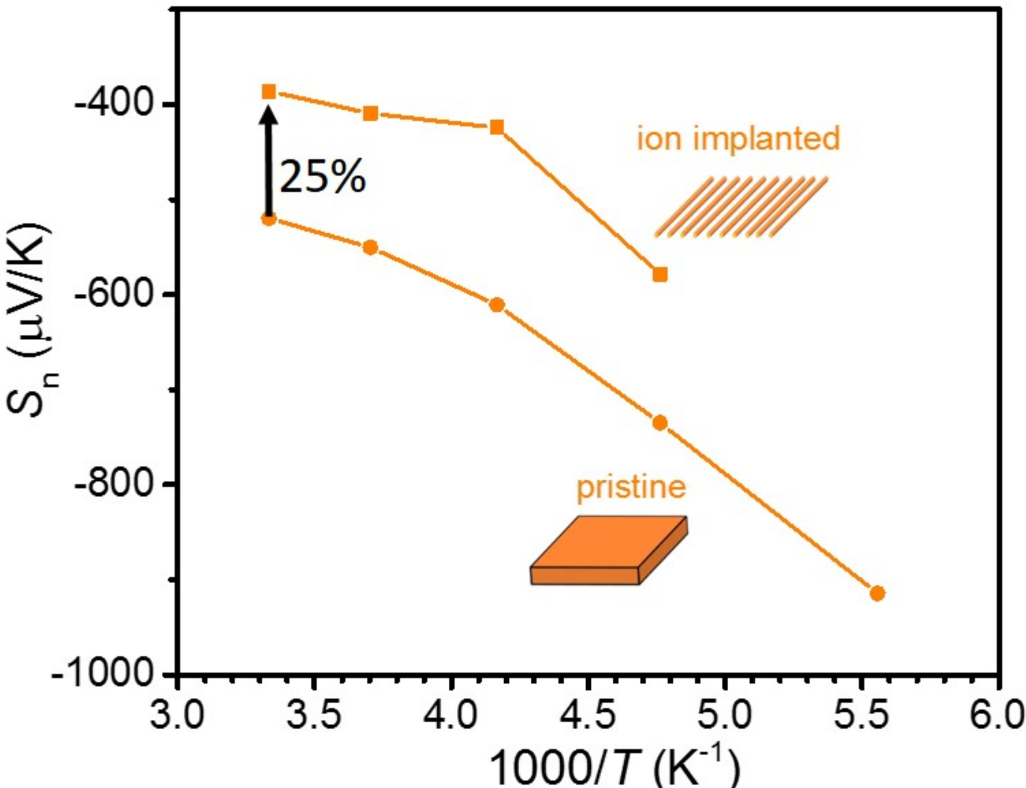

Figure 3.17. The temperature-dependent Seebeck coefficient of pristine and ion-implanted n-type $Al_{0.42}Ga_{0.58}As$. For the ion-implanted samples, only the longitudinal Seebeck coefficient along the conduction channel direction ($S_{\parallel}$) is plotted, the transverse Seebeck coefficient ($S_{\perp}$) is not measurable.

$Al_{0.42}Ga_{0.58}$ (Fig. 3.17) also reveals that the Seebeck coefficient measured in the parallel direction is not significantly reduced (reduction by less than 25%), which indicates the ion-implanted anisotropic thin films are promising candidate materials for thermoelectric applications that require both large conductivity anisotropy and large Seebeck coefficient.

In summary, this section demonstrates an artificial synthesis approach to creating in-plane conductivity anisotropy in bulk-doped semiconductor films based on proton implantation isolation. A post-anneal conductivity anisotropy ratio up to $\rho_\perp/\rho_\parallel = \sigma_\parallel/\sigma_\perp > 10^4$ for both n-type and p-type films is achieved at the price of increasing the longitudinal resistivity by only a factor of $3.3 \sim 3.6$. The increase in longitudinal resistivity may be reduced by decreasing the ratio of the conducting channel spacer to channel width, provided that the proton-implanted isolation region remains wide enough to suppress the transverse conduction. This approach can be readily applied to other semiconductor materials such as Si, SiGe, Bi_2Te_3 and other electric and thermoelectric materials that may lead to novel applications in thermoelectrics.

CHAPTER 4

$p \times n$-type transverse thermoelectrics: Application of anisotropic conductors

This chapter introduces transverse thermoelectrics, a paradigm that is a potential application of anisotropic semiconductors. as well as introducing the "cross-hatched" artificial approach to fabricating $p \times n$-type structures. Section 4.1 introduces transverse thermoelectrics in general, including the anisotropic Seebeck tensor of anisotropic semiconductors and transverse thermoelectric devices. The thermoelectric transport and maximum cooling power density are numerically studied with a normalized notation in Section 4.2. Then Section 4.3 introduces the model of the $p \times n$-type transverse thermoelectrics whose Seebeck anisotropy is ambipolar, *i.e.*, p-type in one direction and n-type transverse, allowing purely transverse thermoelectric transport. Section 4.4 proposes the potential candidate materials and fabrication approaches for $p \times n$-type transverse thermoelectrics. Section 4.5 discusses the interconnect model for the anisotropically conducting n and p layers in cross-hatched $p \times n$ structures. Finally, the plan for a $p \times n$ AlGaAs structure is reported in Section 4.6.

4.1. Introduction to transverse thermoelectrics

4.1.1. Anisotropic Seebeck tensor

It is well known that a temperature difference creates a corresponding electrochemical potential difference in a homogeneous conductor. The density of electric current $\boldsymbol{j}$ in a conductor can be represented as a function of the electric field $\boldsymbol{E}$ and the temperature gradient ∇T [108, 109]:

$$\boldsymbol{j} = \boldsymbol{\sigma} \cdot \boldsymbol{E} + \boldsymbol{\sigma} \cdot (\boldsymbol{S} \cdot \nabla T) \tag{4.1}$$

where $\boldsymbol{E} = -\nabla\bar{\mu}$, $\bar{\mu} = \varphi + \zeta_0/e$ is the electrochemical potential, ζ_0 is the chemical potential energy, e is the electron's charge, $\boldsymbol{\sigma}$ and $\boldsymbol{S}$ are the electric conductivity and Seebeck tensors, respectively. Equation 4.1 can be rewritten as

$$\boldsymbol{j} = \boldsymbol{\sigma} \cdot \left(\boldsymbol{E} + \boldsymbol{E}^T\right), \quad \boldsymbol{E}^T = -\boldsymbol{S} \cdot \nabla T \tag{4.2}$$

wehreby $\boldsymbol{E}^T$ is the so called thermoelectric field.

For an isotropic medium in the presence of a temperature gradient, a thermo-electromotive force (thermo-emf) can only be generated by an inhomogeneity [108]. In isotropic media, the electric conductivity $\boldsymbol{\sigma}$ and the Seebeck tensor $\boldsymbol{S}$ reduce to scalars σ and S, leading to a conservative thermoelectric field and zero thermo-emf:

$$\mathcal{E} = \oint \boldsymbol{E}^T d\boldsymbol{l} = S \oint \nabla T d\boldsymbol{l} = 0. \tag{4.3}$$

In general junctions between two different materials provide the required inhomogeneity. Therefore conventional thermoelectric devices are based on thermocouples consisting of

two materials with different Seebeck coefficients and a temperature difference created between the two junctions of the connected two materials, *i.e.*,

$$\mathcal{E} = \oint \boldsymbol{E}^T d\boldsymbol{l} = S_A \int_{x_1}^{x_2} \nabla T d\boldsymbol{l} + S_B \int_{x_2}^{x_1} \nabla T d\boldsymbol{l} = (S_A - S_B)(T_2 - T_1). \tag{4.4}$$

However, the generation of thermo-emf is also possible in thermoelectrically homogeneous medium, when the thermoelectric properties are anisotropic. Whereas in the isotropic medium, a temperature difference creates a thermoelectric field lengthways, while this is not generally true in anisotropic materials, *i.e.*, the thermoelectric field can be non-parallel to the temperature gradient, $\boldsymbol{E}^T \nparallel \nabla T$. For simplicity, consider a two-dimensional conductor with two orthogonal crystallographic axes a and b, the Seebeck tensor can be represented by a diagonal matrix:

$$\boldsymbol{S} = \begin{pmatrix} S_{aa} & 0 \\ 0 & S_{bb} \end{pmatrix}, \tag{4.5}$$

and after rotating the Cartesian coordinate system by an angle θ about its origin to reach the laboratory coordinates x, y, we have:

$$\boldsymbol{S} = \begin{pmatrix} S_{xx} & S_{xy} \\ S_{yx} & S_{yy} \end{pmatrix} = \begin{pmatrix} S_{aa}\cos^2\theta + S_{bb}\sin^2\theta & (S_{aa} - S_{bb})\sin\theta\cos\theta \\ (S_{aa} - S_{bb})\sin\theta\cos\theta & S_{bb}\cos^2\theta + S_{aa}\sin^2\theta \end{pmatrix}. \tag{4.6}$$

The transverse component of the Seebeck tensor $S_{xy} = S_{yx} = (S_{aa} - S_{bb})\sin\theta\cos\theta$ will lead to a transverse component of the thermoelectric field $E_{\perp}^T$, which is perpendicular to the temperature gradient ∇T direction. The non-zero S_{xy} can have various origins, resulting in different transverse thermoelectric phenomena, as reviewed in Appendix A. Note that if

S_{aa} and S_{bb} have opposite signs, there will be two angles where either $S_{xx} = 0$ or $S_{yy} = 0$, meaning that an appropriately oriented current can induce a *purely* orthogonal heat flow. We call such materials which have a p-type Seebeck in one direction and an n-type Seebeck in the perpendicular direction $p \times n$-type transverse thermoelectrics, and these will be discussed in greater detail in Section 4.3. The transverse thermo-emf generated from the Seebeck anisotropy can be utilized to realize transverse thermoelectric energy conversion devices that have fundamentally different geometric design and thermoelectric utility than the conventional longitudinal thermoelectric devices.

4.1.2. Transverse thermoelectric devices

Conventional thermoelectric devices utilize a longitudinal thermoelectric effect [**10**, p. 1014] to generate electricity, measure temperature differences, or control the temperatures of objects, in which the heat flow of interest is everywhere parallel (p-type) or antiparallel (n-type) to the electrical current flow. Despite their widespread applications, longitudinal thermoelectrics have limitations in micro-scale on-chip cooling because of the complexity of microscale fabrication [**110**], and at cryogenic temperatures because of freeze-out of extrinsically doped semiconductors (Ref. [**10**], Chapter 1), requiring many stages to achieve large thermal differences (Ref. [**10**], Chapter 1) or many thermocouples in series for large thermo-motive voltages [**111**]. A transverse component of the thermoelectric effect [**108**], whereby the electrical current and heat flow (or temperature gradient) are no longer parallel or anti-parallel, can, however, be observed for any material with an anisotropic Seebeck response. Thermoelectric devices which rely on this transverse thermoelectric effect can have distinct advantages in all the above operating applications,

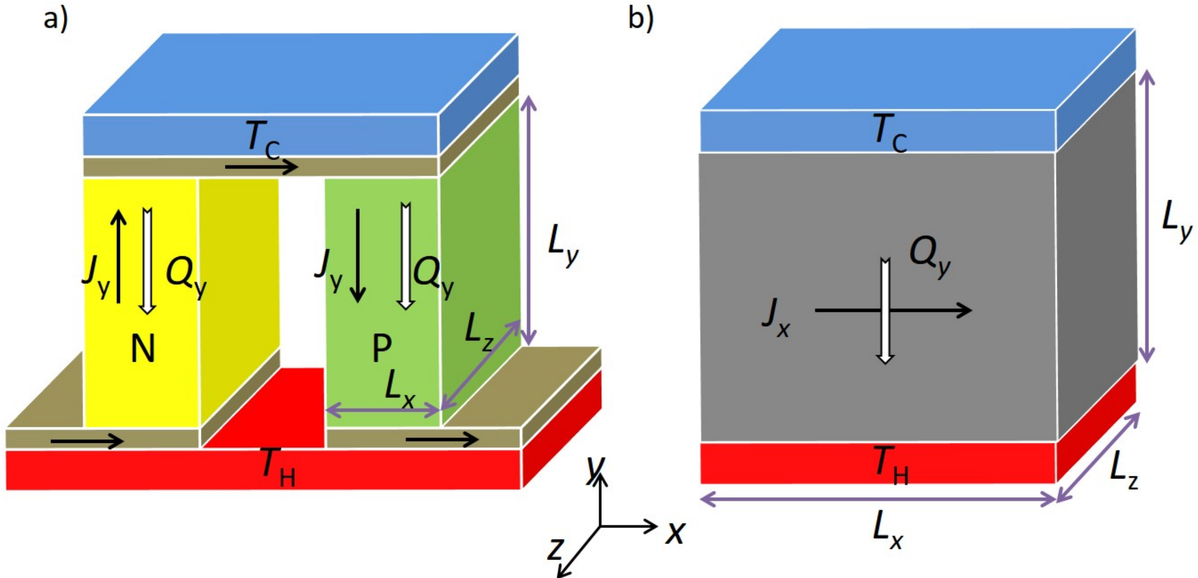

Figure 4.1. (a) Longitudinal (b) Transverse thermoelectric Peltier coolers, whereby heat flow (Q, white arrows) from cold side (T_C) to hot side (T_H) is induced by the applied electrical current density (J, black arrows). The subscripts x, y denote the directions of Q and J. Q_y is parallel/anti-parallel to J_y in (a), and transverse to J_x in (b).

because of their simple, single-leg implementation and their geometric adaptability to the required function, as described below.

Figure 4.1 compares a standard double-leg longitudinal thermoelectric device (Fig. 4.1a) with a single-leg transverse thermoelectric device. Note that the former device requires two different materials with oppositely signed Seebeck coefficients, comprising two legs, and two intermediate electrical contacts connecting the n-leg to a metal and then to a p-leg at the cold junction. The transverse device is single-leg and requires no intermediate junction, enabling geometric scalability to an arbitrary size, small or large.

The physics of the transverse thermoelectric effect is well-established [**10**, **108**]. In transverse thermoelectric devices, a temperature gradient can generate a Seebeck voltage

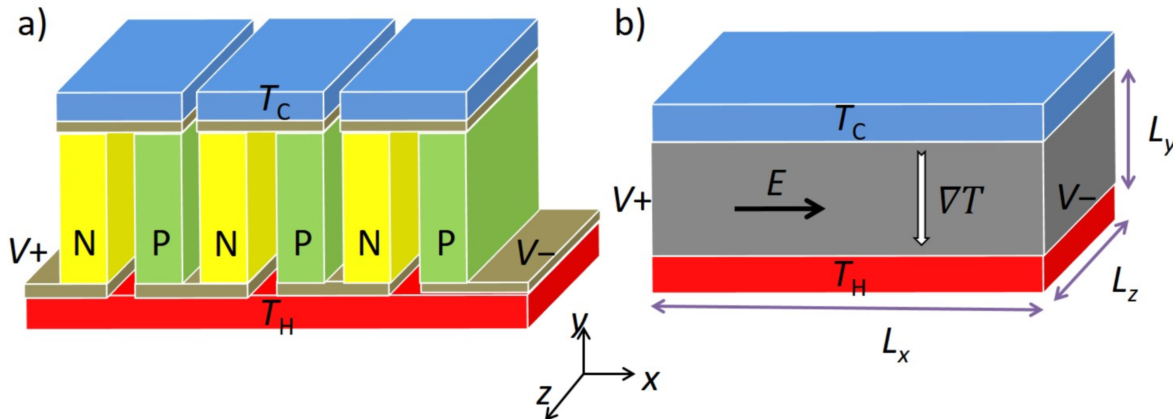

Figure 4.2. (a) Longitudinal and (b) transverse thermoelectric generators for large Seebeck voltage generation. To increase the generated Seebeck voltage $V_+ - V_-$ from a given temperature different $T_H - T_C$, the longitudinal generator requires many thermoelements linked in series, which involves the arrangement of alternate n and p-legs with increasing junction resistance. The transverse thermoelectric generator can just increase the length-to-thickness ratio L_x/L_y.

in the transverse direction, and, conversely, the induced heat flow in the Peltier effect is transverse to the applied electrical current (Fig. 4.1b) [10]. The transverse Seebeck and Peltier coefficients can then be defined as:

$$S_{xy} = \frac{dV/dx}{dT/dy}\,, \pi_{yx} = \frac{Q_y}{J_x}, \tag{4.7}$$

where Q_y, J_x are heat flux density and electric current density, respectively, and the transverse figure of merit is defined as $Z_{xy}T = S_{xy}^2 T/\rho_{xx}\kappa_{yy}$. Similar to the longitudinal figure of merit, the transverse figure of merit determines the efficiency of both Peltier coolers and Seebeck generators; large $Z_{xy}T$ values lead to higher efficiency, although the specific formula differs for the transverse case [12].

The separate directions for electric current and heat flow gives rise to special advantages in the geometric engineering of transverse thermoelectric devices. One such advantage is the generation of a large Seebeck voltage in the x direction with a finite temperature difference in the y direction by changing the length-to-thickness ratio of the transverse thermoelements [108, 109]. As shown in Fig. 4.2, for a vertical temperature difference $\Delta T = T_H - T_C$, the Seebeck voltage generated is $M \cdot S\Delta T$ in a longitudinal thermoelement, where M is the number of series thermocouples, and $S_{xy}\Delta T\frac{L_x}{L_y}$ in a transverse thermoelement. Thus the transverse Seebeck voltage can be increased with a trivial geometric increase of the length L_x or by reducing the sample thickness L_y of a single block of material. The longitudinal Seebeck voltage, on the other hand, can be increased only by increasing M, linking many longitudinal thermoelements in series, requiring an arrangement of n and p-legs in a series of junctions of increasing length and complexity. The dependence of the transverse Seebeck voltage on the length-to-thickness ratio makes transverse thermoelectrics very useful for producing fast-response thermal detectors of very small thickness, and therefore thermal mass, and sizeable Seebeck voltage [112–114].

Another advantage of the separation of electric current and heat flow directions in transverse thermoelectric devices is in tapered geometries for transverse Peltier cooling [115]. To achieve a substantial cooling effect, longitudinal thermoelectrics usually use a cascade structure consisting of a vast number of thermocouples stacked in a pyramid shape (Fig. 4.3a). The bottom stages need to have larger cooling power than the upper stages, because they have to extract the Joule heating of the upper stages and from the heat load while generating a small thermal differential. The thermal resistance associated with junctions at each stage interface limits practical implementation to at most six stages [10].

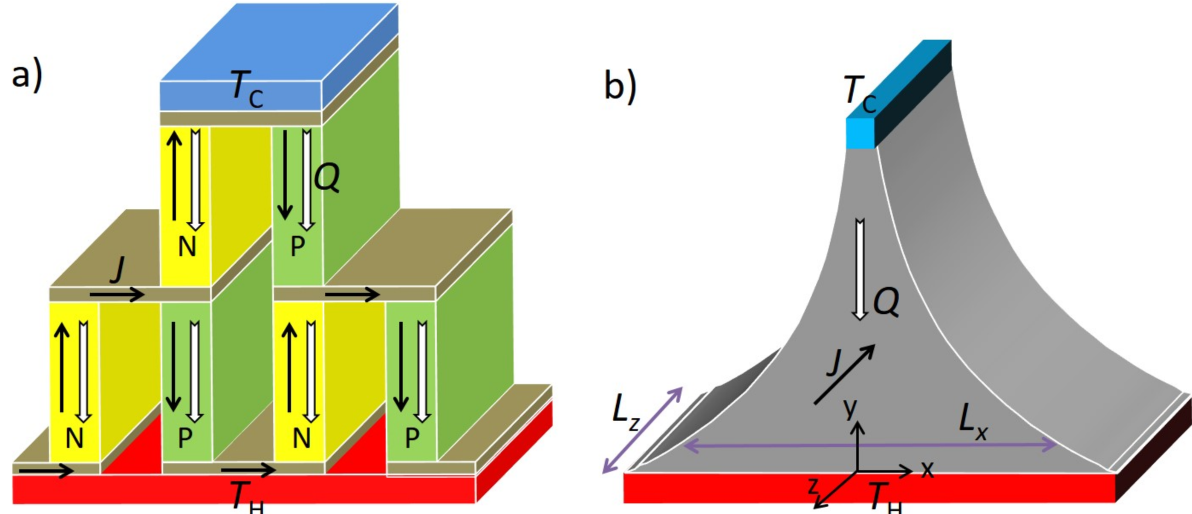

Figure 4.3. (a) Cascaded longitudinal Peltier cooler and (b) exponentially tapered transverse Peltier cooler for large thermal differences. Note the simplicity of the single-leg structure on the right.

However, the cascading structure is much simpler in transverse Peltier coolers which can be simply implemented in an exponentially tapered geometry. As shown in Fig. 4.3(b), an exponentially tapered device has a wide base on the heat-sink side and a narrow strip on the refrigerated source side, with $L_x = L_{x,0} \exp^{-y/L}$, where $L_{x,0} = L_x(y = 0)$, and L sets the characteristic length scale of the tapering. The cooling power is increased along the heat flow direction, because of the increasing area of the cross-section, and performs as a cascade structure without addition of thermal or electrical junctions [**109**]. It has been shown that arbitrarily large cooling temperature differences can be achieved theoretically by use of an exponentially tapered device [**115**], which serves as an infinite-stage cascade cooler; even a trapezoidal shape has been shown experimentally to result in significant enhancement of the maximum cooling temperature [**116**].

4.2. Cooling power of transverse thermoelectrics

In this section, the theory of transverse thermoelectric coolers is advanced. Though the physics of the transverse thermoelectric effect is well-established [108], the performance of transverse coolers, especially the cooling power, has rarely been studied. The maximum temperature difference achievable for layered composite transverse coolers has been approximated analytically [114] and calculated numerically [117], however, general calculations of the thermoelectric performance for transverse thermoelectrics have been limited thus far [12]. To solve this problem, Section 4.2.1 introduces a normalized notation to generalize the governing equations of the thermoelectric transport for arbitrary temperatures and materials parameters. It is confirmed that analytical solutions for the temperature distribution, maximum temperature difference, and maximum cooling power density in transverse coolers do not exist. A numerical study of the normalized temperature distribution and maximum cooling power density of rectangular coolers (Section 4.2.2) reveals that transverse coolers provide superior performance over longitudinal coolers with the same figure of merit. Section 4.2.3 extends the numerical study to exponentially tapered coolers and shows that exponential tapering can enhance the maximum cooling temperature difference and maximum cooling power density, at a price of reducing the total cooling power. The work in this section has been published in SPIE conference proceedings [118].

4.2.1. Normalized thermoelectric transport equations

The Seebeck tensor determines the Peltier heat flux density when an electrical current is applied, according to the Peltier tensor $\mathbf{\Pi} = T\boldsymbol{S}$. Considering an anisotropic Seebeck

tensor with a transverse component S_{xy} (Eq. 4.6), an electrical current $\boldsymbol{J}$=$J_x\hat{\boldsymbol{x}}$ along the x-direction (Fig. 4.1b) will induce a Peltier heat flux $\boldsymbol{Q_\Pi} = \boldsymbol{\Pi J}$= $(T\boldsymbol{S})\,\boldsymbol{J}$ with longitudinal and transverse components

$$Q_{\Pi,x} = \boldsymbol{Q}_\Pi \cdot \hat{\boldsymbol{x}} = S_{xx} T J_x, \tag{4.8}$$

$$Q_{\Pi,y} = \boldsymbol{Q}_\Pi \cdot \hat{\boldsymbol{y}} = S_{yx} T J_x. \tag{4.9}$$

The total heat flux density $\boldsymbol{Q} = \boldsymbol{Q_\Pi} - \boldsymbol{\kappa^c \nabla} T$ consists of one component induced by the electrical current through the Peliter effect and another by the temperature gradient via diffusive Fourier heat flow, whereby $\boldsymbol{\kappa^c}$ is the open circuit thermal conductivity tensor when $\boldsymbol{J} = 0$ [119]. Boundary conditions including isothermal surfaces $T(y = 0) = T_h$ and $T(y = L_y) = T_c$ and equi-potential surfaces $x = 0$ and $x = L_x$ lead to a thermal gradient along the y-direction $\boldsymbol{\nabla} T = dT/dy\hat{\boldsymbol{y}}$, only, and a uniform electric field along the x-axis $E_x\hat{\boldsymbol{x}}$ [119]. Thus the longitudinal current density and transverse heat flow are both only a function of y for a given material:

$$J_x = \frac{E_x}{\rho_{xx}} - \frac{S_{xy}}{\rho_{xx}}\frac{dT}{dy}, \tag{4.10}$$

$$Q_y = T\frac{E_x}{\rho_{xx}} S_{yx} - (1 + zT)\kappa^c_{yy}\frac{dT}{dy}, \tag{4.11}$$

where $zT = (S_{xy}S_{yx}T/\rho_{xx}\kappa^c_{yy}) = (S^2_{xy}T/\rho_{xx}\kappa^c_{yy})$ is the figure of merit for transverse thermoelectrics.

For steady state, the charge and energy conservation conditions require $\boldsymbol{\nabla}\cdot\boldsymbol{J}=0$ and $\boldsymbol{\nabla}\cdot(\boldsymbol{Q}+\bar{\mu}\boldsymbol{J})=0$, where $\bar{\mu}$ is the electrochemical potential, and $-\boldsymbol{\nabla}\bar{\mu}=\boldsymbol{E}$. While the former condition is guaranteed by Eq. 4.10, the latter condition for the transverse cooler here is simplified to :

$$\frac{dQ_y}{dy}=E_xJ_x, \tag{4.12}$$

i.e., the Joule heating E_xJ_x due to longitudinal current must diffuse transversely (Q_y). The governing equation of the temperature distribution for the transverse cooler can be deduced from Eqs. (4.10)-(4.12), which is simplified to the following form assuming temperature-independent thermoelectric parameters:

$$0=\left(\frac{E_x}{S_{xy}}-\frac{dT}{dy}\right)^2+\frac{1+zT}{z}\frac{d^2T}{dy^2}. \tag{4.13}$$

To minimize the number of independent parameters and generalize the equations for various temperatures and device dimensions, we introduce the heat flux and electric field scales $Q_0=(\kappa^c_{yy}T_h/L)$ and $E_0=(S_{xy}T_h/L)$, respectively, which normalize the thermoelectric transport equations. Eqs. (4.11) and (4.13) can be simplified as :

$$Q^*_y=-(zT_h)E^*T^*-(1+(zT_h)T^*)\,\frac{dT^*}{dy^*}, \tag{4.14}$$

$$0=\left(E^*-\frac{dT^*}{dy^*}\right)^2+\frac{1+(zT_h)T^*}{zT_h}\frac{d^2T^*}{d(y^*)^2}, \tag{4.15}$$

where $T^* = (T/T_h)$, $E^* = (E_x/E_0)$, $y^* = (y/L_y)$ and $Q^* = (Q_y/Q_0)$ are normalized temperature, electric field, y coordinate and heat flux density, respectively. Equations (4.14) and (4.15) indicate that the normalized heat flux density Q_y^* and the normalized temperature profile $T^*(y^*)$ only depend on the normalized electrical field E^* and transverse figure of merit zT_h. When the cooling power density at cold side Q_c^* is zero, the maximum normalized temperature difference $\Delta T^* = 1 - T_c^* = 1 - T^*(y^* = 1)$ will be achieved with an optimal E^* that satisfies

$$\frac{\partial \Delta T^*}{\partial E^*}|_{E^*=E^*_{opt}} = 0, \tag{4.16}$$

thus $\Delta T^*_{\max}(zT_h)$ is only a function of zT_h. Similarly the maximum of the cooling power density at the cold side $Q_c^* = Q_y^*(y^* = 1)$ for a given T_c^* can be obtained when E^* satisfies:

$$\frac{\partial \Delta Q_c^*}{\partial E^*}|_{E^*=E^*_{opt'}} = 0, \tag{4.17}$$

and $Q^*_{\mathrm{c,max}}$ depends only on T_c^* and zT_h. Equations (4.14)-(4.17) cannot be exactly solved with analytical methods. Thus it is important to solve the temperature profile and heat flux numerically to study the cooling power of the transverse coolers.

4.2.2. Cooling power of rectangular transverse coolers

The normalized temperature profile in rectangular coolers for maximum temperature difference corresponding to various transverse figure of merit zT_h values (Fig. 4.4) is numerically calculated by solving the governing equations (4.14)-(4.17) with the bvp4c solver in Matlab [120]. The maximum temperature difference is achieved with no heat load $Q_c^* = 0$. The zero slope at the hot side $(y^* = 0)$ indicates that there is no heat diffusing

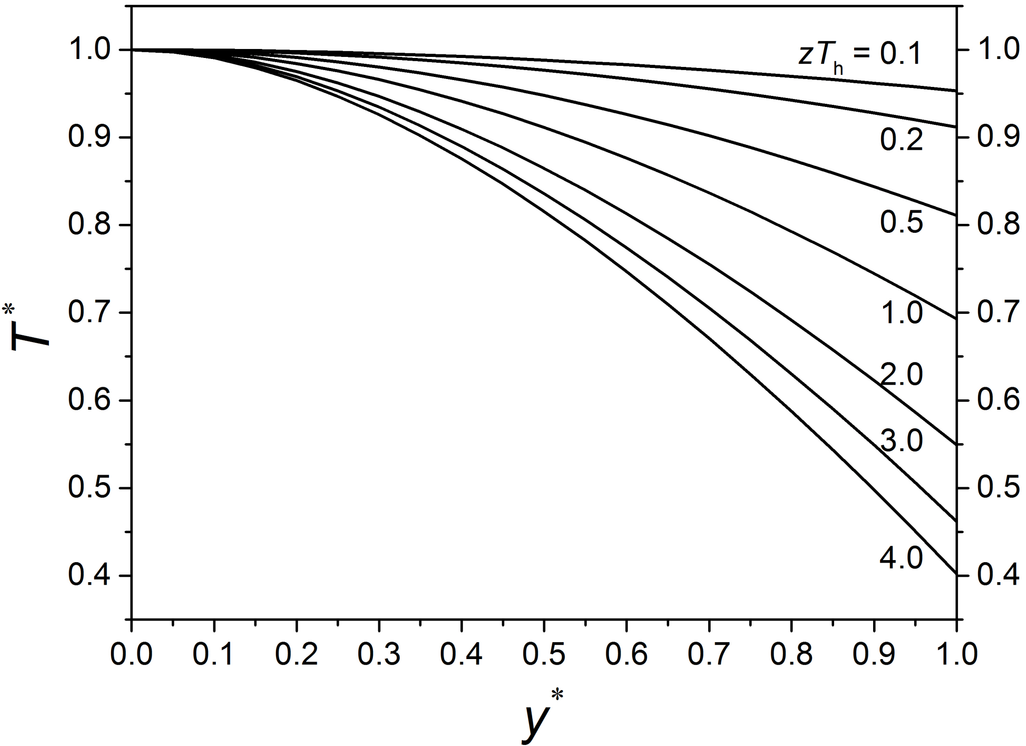

Figure 4.4. Normalized temperature profile of transverse thermoelectric coolers operating at maximum temperature difference for various zT_h values. At $y^* = y/L_y = 0$ the heat sink temperature $T^* = T/T_h = 1$ and at the $y^* = 1$ the cold side heat flow $Q_c = Q_y(y^* = 1) = 0$.

from the heat sink back to the device. Thus all the Peltier cooling power will be used to compensate the Joule heating in the device. The temperature slope from hot side to cold side becomes steeper as zT_h increases.

The dependence of the maximum temperature difference $\Delta T^* = 1 - T_c^*$ on zT_h is summarized in Fig. 4.5, left axis. Transverse coolers show a larger ΔT^* than the analytically solved $\Delta T^* = 1 + \frac{1-\sqrt{1+2zT_h}}{zT_h}$ for longitudinal coolers [11]. For $zT_h = 1$, a 30% temperature reduction is predicted for the transverse cooler, which is slightly larger than

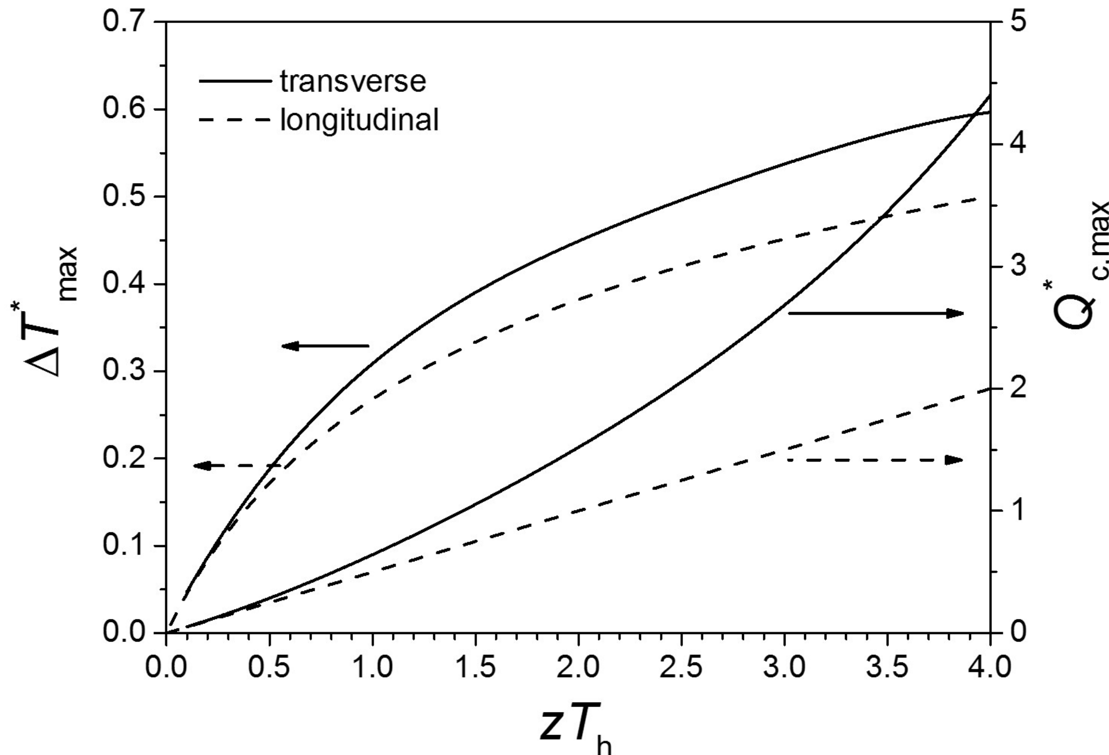

Figure 4.5. The dependence on zT of maximum normalized temperature difference (left axis) whereby $\Delta T^* = (T_h - T_c)/T_h$ and maximum cooling power density when $T_c = T_h$ (right axis) for transverse thermoelectric coolers in comparison with longitudinal coolers. $\Delta T^*_{\max}$ and $Q^*_{\mathrm{c,max}}(T^*_c = 1)$ are numerically calculated for the transverse coolers but can be analytically solved for the longitudinal coolers [**10**, **11**].

the 27% reduction of the conventional longitudinal cooler with the same zT_h. For the sake of theoretical comparison, a larger zT_h of 4 results in a 60% temperature reduction for the transverse cooler compared with 50% for the longitudinal cooler.

The normalized maximum cooling power density $Q^*_{\mathrm{c,max}}$ of the transverse cooler when $T_c = T_h$ is plotted in Fig. 4.5, right axis as a function of zT_h. Unlike the linear dependence $Q^*_{\mathrm{c,max}} = 1/2\ zT_h$ for longitudinal coolers when $T^*_c = 1$ [**10**], $Q^*_{\mathrm{c,max}}$ for transverse coolers

shows a superlinear dependence on zT_h which exceeds the longitudinal limit at all zT_h, approaching the longitudinal behavior in the small zT_h limit. The enhancement in $Q^*_{\mathrm{c,max}}$ for transverse coolers over longitudinal coolers with the same zT_h is 28% when $zT_h = 1$ and rapidly increases to 220% when $zT_h = 4$.

Figure 4.6 shows the maximum cooling power density $Q^*_{\mathrm{c,max}}$ of rectangular transverse coolers as a function of T^*_c for various zT_h values. For a given zT_h, the Fourier diffusion heat flow increases when T^*_c decreases, thus a larger portion of the Peltier cooling power is used to compensate the diffusive heat flow, and the remaining cooling power density at the cold side $Q^*_{\mathrm{c,max}}$ will decrease. The intersection of the curves with the horizontal axis and vertical axis corresponds to the maximum normalized temperature difference case and maximum cooling power density case in Fig. 4.5, respectively. The performance of a rectangular transverse cooler can be readily predicted from Fig. 4.6 for any given heat load or cold side temperature.

4.2.3. Cooling power of exponentially tapered transverse coolers

As discussed in Section 4.1.2, transverse thermoelectric coolers can be exponentially tapered (Fig. 4.3b) to enhance the maximum cooling temperature. Following the analysis of Kooi *et al.* for the N-E effect [**119**], the exponential tapering adds the term of $Q_y \frac{d(\ln z)}{dy}$ to the right of Eq. (4.12), and hence a new term to the right of Eq. (4.13), yielding the equation:

$$0 = \left(\frac{E_x}{S_{xy}} - \frac{dT}{dy}\right)^2 + \frac{1+zT}{z}\frac{d^2T}{dy^2} - \left(\frac{1+zT}{z}\frac{dT}{dy} - \frac{E_x}{S_{xy}}T\right)/L, \tag{4.18}$$

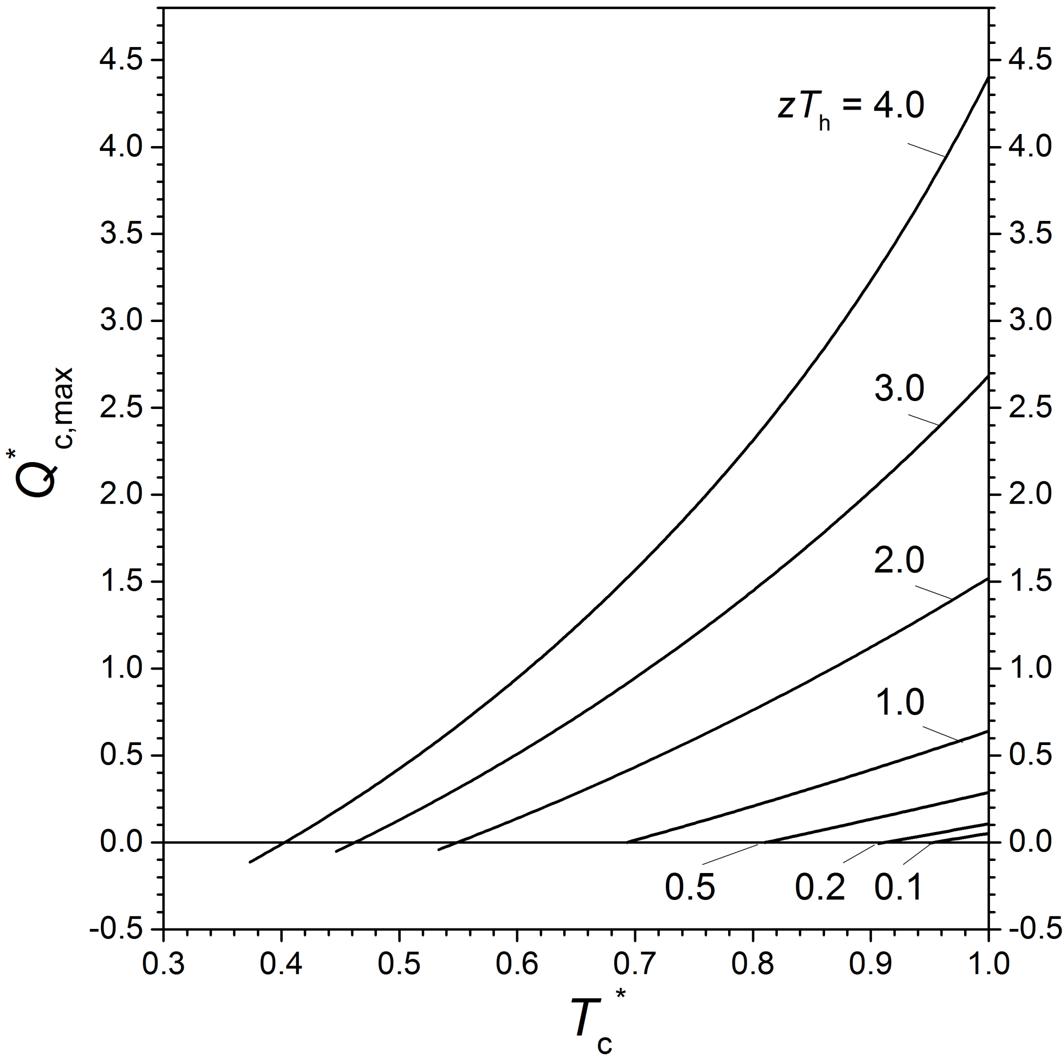

Figure 4.6. The maximum normalized cooling power density $Q^*_{\mathrm{c,max}}$ for transverse thermoelectric cooling as a function of the normalized cold side temperature T^*_c for various zT_h values.

whereby L is the length scale for the exponential tapering defined in

$$L_x(y) = L_x(0) \exp^{-y/L} . \tag{4.19}$$

Similar to the rectangular coolers, we can normalize this equation in terms of $T^* = (T/T_h)$, $E^* = (E_x/E_0)$, $y^* = (y/L)$ and $Q^* = (Q_y/Q_0)$, in which $Q_0 = (\kappa_{yy}^c T_h/L)$ and $E_0 = (S_{xy}T_h/L)$. The normalized equation is:

$$0 = \left(E^* - \frac{dT^*}{dy^*}\right)^2 + \frac{1 + (zT_h)T^*}{zT_h} \frac{d^2T^*}{d(y^*)^2} - \left(\frac{1 + (zT_h)T^*}{zT_h} \frac{dT^*}{dy^*} - E^*T^*\right) . \tag{4.20}$$

Exponential tapering enhances the maximum value of the normalized temperature difference $\Delta T^* = (T_h - T_c)/T_h$. For an exponentially tapered transverse thermoelectric cooler of height $y = L_y$, the parameter L_y/L defines the overall shape of the tapering, whereby L_y is the device thickness along the y axis. The ratio of top $L_x(y = L_y)$ and bottom width $L_x(0)$ of the cooler decreases exponentially as the tapering parameter L_y/L increases. As shown in Fig. 4.8, larger tapering parameters L_y/L correspond to larger ΔT^*_{max} for a given zT_h value. The maximum normalized cooling temperature differences at different $L_y/L > 0$ are larger than that achieved with a rectangular transverse thermoelectric cooler at $L_y/L = 0$ (black line). For a physically reasonable tapering parameter $L_y/L = 5$, which means when the heat sink width is $L_x(0) = 1$ cm, the cold side width is $L_x(y = L_y) = 0.007$ cm, can increase ΔT^*_{max} by 85%, from $\Delta T^*_{\text{max}} = 0.31$ to $\Delta T^*_{\text{max}} = 0.57$, when the figure of merit is $zT_h = 1$.

The same maximum normalized temperature difference achieved with an exponentially tapered cooler with zT_h can be achieved with a rectangular cooler that has a larger figure of merit $z_{\text{eff}}T_h > zT_h$. The $z_{\text{eff}}T_h$ of a rectangular transverse thermoelectric cooler for

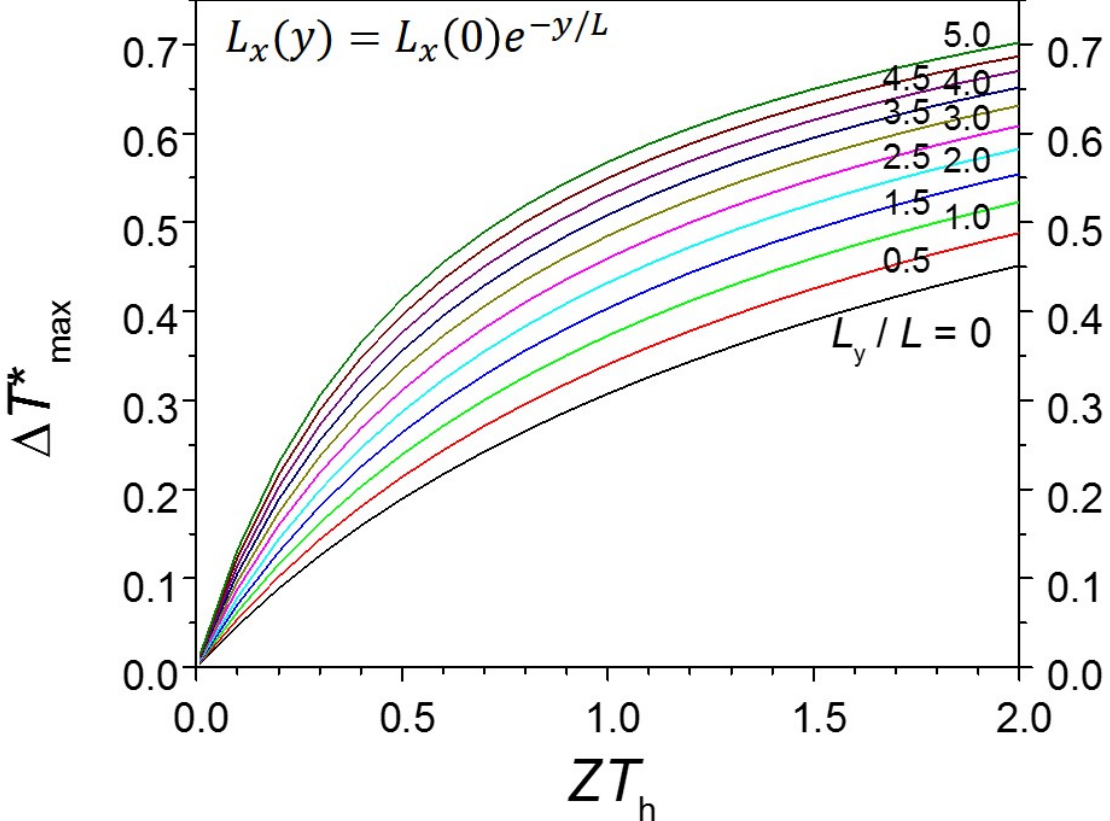

Figure 4.7. The dependence on zT_h of maximum normalized temperature difference whereby $\Delta T^* = (T_h - T_c)/T_h$ for an exponentially tapered transverse cooler with $L_x(y) = L_x(0)e^{(-y/L)}$. The parameter L_y/L defines the overall shape of the tapered coolers, since $L_x(y = L_y)/L_x(0) = e^{(-L_y/L)}$, *i.e.*, the larger L_y/L is, the narrower the top width is relative to the bottom width.

transverse thermoelectric coolers with various tapering parameter L_y/L is obtained by calculating the ΔT^*_{max} for the exponentially tapered cooler (Fig. 4.7), and extracting the corresponding $z_{\text{eff}}T_h$ from the ΔT^*_{max}-zT_h curve for the rectangular cooler(Fig. 4.5). As shown in Fig. 4.8(a), $z_{\text{eff}}T_h$ increases almost linearly with zT_h for each tapering parameter

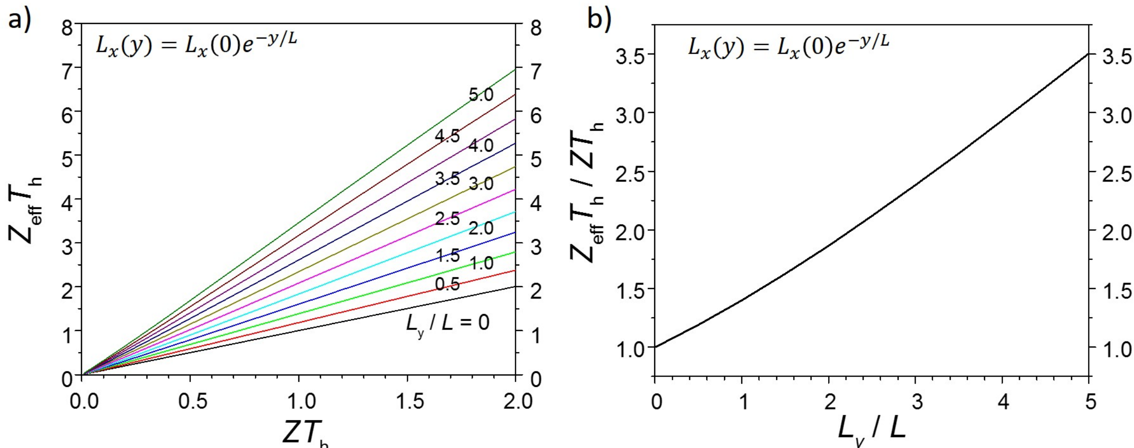

Figure 4.8. (a) Equivalent effective zT_h values to achieve the same normalized temperature difference with a rectangular transverse cooler for various tapering parameters L_y/L. (b) The effective zT_h enhancement depends on the tapering parameter.

L_y/L, thus the zT enhancement factor $\gamma_{zT} = z_{\text{eff}}T_h/zT_h$ can be obtained by take the slope of the lines. Figure 4.8b) shows that γ_{zT} has a quasi-linear dependence on the tapering parameter L_y/L, and a polynomial fitting leads to an empirical approximation of $\gamma_{zT} = 1 + 0.389(L_y/L) + 0.023(L_y/L)^2$ for $L_y/L <= 5$.

The maximum normalized cooling power density $Q^*_{\text{c,max}}$ for the exponentially tapered transverse thermoelectric coolers as a function of T^*_c for various L_y/L values is shown in Fig. 4.9(a), assuming $zT_h = 1.0$. Similar to ΔT^*_{max}, $Q^*_{\text{c,max}}$ for the exponentially tapered transverse thermoelectric coolers ($L_y/L > 0$) is also enhanced compared with the rectangular coolers ($L_y/L = 0$). The enhancement in ΔT^*_{max} and $Q^*_{\text{c,max}}$ for exponentially tapered transverse thermoelectric coolers opens up potential applications in hot-spot cooling that requires large temperature difference and large cooling power density locally. However, the enhancement in the cooling power density comes at a price of reducing the total cooling

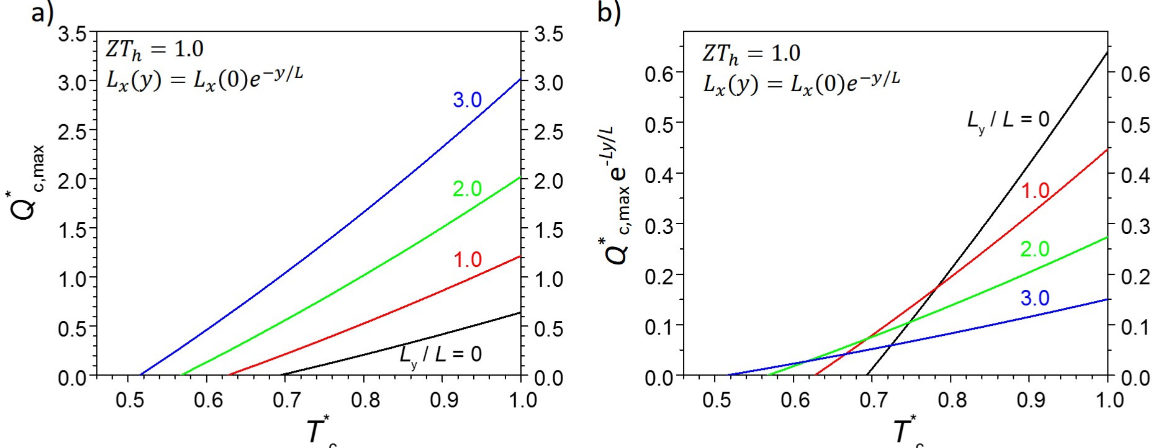

Figure 4.9. (a) The maximum normalized cooling power density $Q^*_{\mathrm{c,max}}$ for an exponentially tapered transverse cooler as a function of the normalized cold side temperature T_c^* for various tapering parameters L_y/L. The figure of merit is assumed to be $zT_h = 1.0$. (b) $Q^*_{\mathrm{c,max}}e^{(-L_y/L)}$ scales the cooling power density at the tapered top by the reduced area of the top surface to effectively give the cooling power density per unit base-area. This is plotted versus T_c^*.

power $Q^*_{\mathrm{c,max}}L_x(y = L_y)$. For a given heat sink base width $L_x(0)$, the total cooling power is proportional to $Q^*_{\mathrm{c,max}}e^{-L_y/L}$. As shown in Fig. 4.9(b), the intersection of the curves with the vertical axis, which correspond to the maxium cooling power case ($T_c^* = 1$), decreases as L_y/L increases, which indicates the tapering brings in a trade-off between the maximum cooling power density and the total cooling power.

In conclusion, this section studies the theory of transverse thermoelectric coolers with a normalized variable notation, which generalizes the equations to be independent on the absolute temperatures and sample parameters. Numerical calculation of the maximum temperature difference and cooling power for the rectangular transverse thermoelectric coolers shows enhancement of performance compared with longitudinal coolers with the same figure of merit. Further study on the exponentially tapered coolers indicates that

the tapering enhances the maximum normalized cooling temperature difference and the maximum cooling power density, though at a price of reducing the maximum total cooling power. This opens up potential applications of exponentially tapered transverse thermoelectric coolers in hot-spot local cooling, which is especially interesting for on-chip thermal management.

4.3. $p \times n$-type transverse thermoelectrics model

In this section, we study the model of a new paradigm of transverse thermoelectrics named as "$p \times n$-type" transverse thermoelectrics, where $p \times n$ refers to p-type Seebeck coefficient and electrical conductivity in one direction and n-type Seebeck coefficient and conductivity in the orthogonal direction. The $p \times n$-type Seebeck anisotropy can result from the $p \times n$-type anisotropic electrical conductivity, which requires both electrons and holes to conduct in parallel, with electrons dominating conduction in one direction and holes dominating the orthogonal direction. The thermoelectric property tensors and transport equations of materials with $p \times n$-type conductivity will be studied in detail below. This model was firstly published in Physics Review Letters [**12**], with my contribution in the band structure simulation of InAs/GaSb type-II superlattices, which was proposed as a candidate $p \times n$ material.

4.3.1. Thermoelectric tensors of $p \times n$ materials

The large transverse Seebeck coefficient in the $p \times n$ materials arises because of parallel anisotropic conduction between electron and hole bands [**12**]. Consider an intrinsic material with anisotropic electron and hole electrical conductivity tensors $\boldsymbol{\sigma}_n$, $\boldsymbol{\sigma}_p$ and isotropic

Seebeck tensors $\boldsymbol{s}_n$,$\boldsymbol{s}_p$. For simplicity, we only consider two conducting directions. In the Cartesian coordinate system defined by the orthogonal principal axes (a, b) of the crystal, the thermoelectric tensors are diagonal:

$$\boldsymbol{\sigma}_n = \begin{bmatrix} \sigma_{n,aa} & 0 \\ 0 & \sigma_{n,bb} \end{bmatrix} \quad , \quad \boldsymbol{\sigma}_p = \begin{bmatrix} \sigma_{p,aa} & 0 \\ 0 & \sigma_{p,bb} \end{bmatrix}$$

(4.21)

$$\boldsymbol{s}_n = \begin{bmatrix} s_n & 0 \\ 0 & s_n \end{bmatrix} \quad , \quad \boldsymbol{s}_p = \begin{bmatrix} s_p & 0 \\ 0 & s_p \end{bmatrix},$$

where $s_n < 0$ and $s_p > 0$. The total conductivity tensor and total resistivity tensor are $\boldsymbol{\sigma} = \boldsymbol{\rho}^{-1} = \boldsymbol{\sigma}_n + \boldsymbol{\sigma}_p$. Note that the Seebeck tensor for each band is isotropic when taken separately.

The Seebeck tensor of the two-band system is the average of the two Seebeck tensors, weighted by the conductivity tensors:

$$\boldsymbol{S} = (\boldsymbol{\sigma}_n \boldsymbol{s}_n + \boldsymbol{\sigma}_p \boldsymbol{s}_p)(\boldsymbol{\sigma}_n + \boldsymbol{\sigma}_p)^{-1}. \tag{4.22}$$

This weighting by conductivity tensors leads to Seebeck coefficients of opposite signs in orthogonal directions. Suppose holes dominate conduction in the a direction and electrons dominate in the b direction, as labeled by the symbol $p \times n$ in Fig. 4.10.

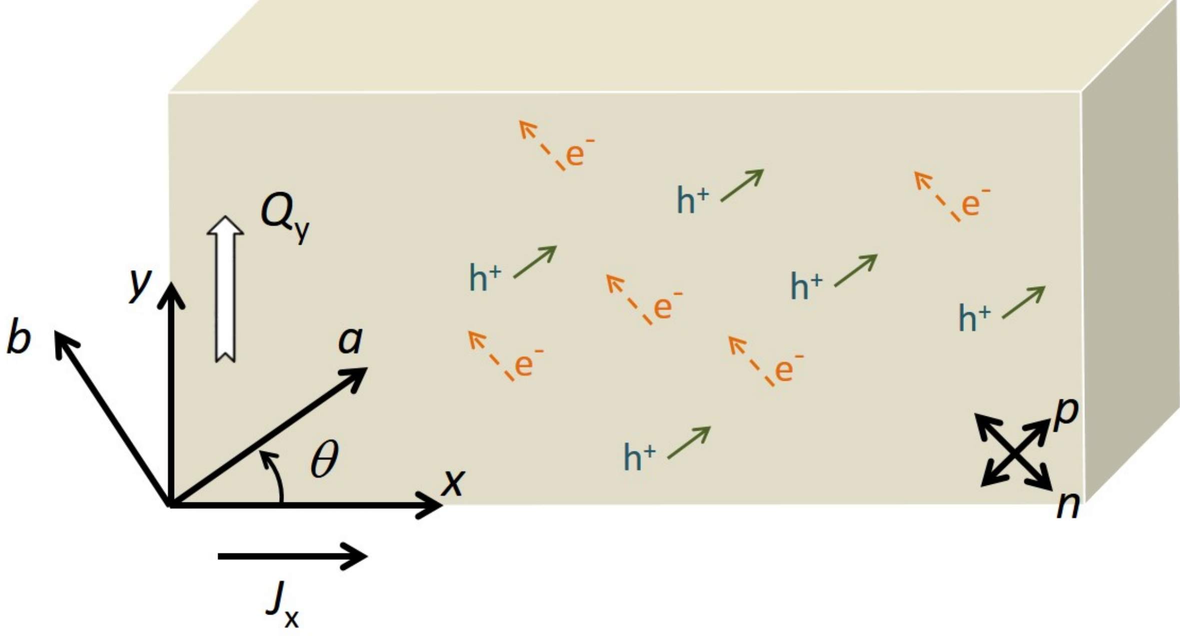

Figure 4.10. $p \times n$-type thermoelectrics have p-type dominated conduction and Seebeck coefficient along the a-axis and n-type dominated conduction and Seebeck coefficient along the orthogonal b-axis, as indicated by the crossed arrow symbol at the bottom right. The movement of electrons (orange dashed arrows) and holes (green solid arrows) in orthogonal directions results in net charge current J_x to the right and net particle or heat flow Q_y up. The carrier transport shown in this figure can be driven either by drift due to an electric field along $+x$ direction or by diffusion due to a temperature gradient along $-y$ direction [12].

We define a small variable ξ as the ambipolar conductivity ratio of two carriers: $\xi_a = \sigma_{n,aa}/\sigma_{p,aa} < 1$, $\xi_b = \sigma_{p,bb}/\sigma_{n,bb} < 1$. The total Seebeck tensor is

$$\boldsymbol{S} = \begin{bmatrix} S_{p,aa} & 0 \\ 0 & S_{n,bb} \end{bmatrix}, \tag{4.23}$$

with components

$$S_{p,aa} = \tfrac{s_p+\xi_a s_n}{1+\xi_a} > 0 \tag{4.24}$$
$$S_{n,bb} = \tfrac{s_n+\xi_b s_p}{1+\xi_b} < 0$$

when $\xi_a < |s_p/s_n|$ and $\xi_b < |s_n/s_p|$. And the Seebeck anisotropy is

$$\Delta S = S_{p,aa} - S_{n,bb} = \frac{1-\xi_a\xi_b}{(1+\xi_a)(1+\xi_b)}(s_p - s_n). \tag{4.25}$$

It will increase as ξ_a, ξ_b get smaller, and reaches the maximum value $(s_p - s_n)$ when $\xi_a = \xi_b = 0$, *i.e.*, when holes only conduct in the a direction and electrons only conduct in the b direction. Note that when the band conductivities are insufficiently anisotropic, Eq. 4.24 is not satisfied, and the Seebeck tensor will be anisotropic and unipolar, either fully p-type or fully n-type as described in Section A. The strong Seebeck anisotropy can lead to a large transverse Seebeck coefficient, as discussion in Section 4.1.1.

4.3.2. Transverse thermoelectric figure of merit

The transverse thermoelectric figure-of-merit is defined as:

$$Z_{xy}(\theta)T = \frac{S_{xy}^2}{\kappa_{yy}\rho_{xx}} = \frac{\sin^2\theta\cos^2\theta(S_{p,aa}-S_{n,bb})^2}{(\sin^2\theta\kappa_{aa}+\cos^2\theta\kappa_{bb})(\cos^2\theta\rho_{aa}+\sin^2\theta\rho_{bb})}. \tag{4.26}$$

It has significance analogous with that of the figure-of-merit in conventional longitudinal thermoelectrics. The larger that the value of $Z_{xy}(\theta)T$, the higher the efficiency of the corresponding transverse thermoelectric generator or cooler is. $\theta_\perp$ maximizes $Z_{xy}(\theta)T$

when [111, 121, 122]

$$\cos^2\theta_\perp = \frac{1}{1+\sqrt{\frac{\kappa_{bb}/\kappa_{aa}}{\rho_{bb}/\rho_{aa}}}} \tag{4.27}$$

with

$$Z_\perp T = Z_{xy}(\theta_\perp)T = \frac{(S_{p,aa}-S_{n,bb})^2 T}{(\sqrt{\rho_{aa}\kappa_{aa}}+\sqrt{\rho_{bb}\kappa_{bb}})^2}. \tag{4.28}$$

Equation 4.27 shows that $\theta_\perp$ has no dependence on the Seebeck anisotropy. In semiconductors the thermal conductivity is usually dominated by the lattice thermal conductivity κ_l. If we consider the thermal conductivity κ_l to be approximately isotropic, then it is useful to define a transverse power factor $PF_\perp$ which can be optimized for optimal transverse thermoelectric performance:

$$PF_\perp = \frac{(S_{p,aa}-S_{n,bb})^2}{(\sqrt{\rho_{aa}}+\sqrt{\rho_{bb}})^2}. \tag{4.29}$$

Since the tensors $\boldsymbol{S}$ and $\boldsymbol{\rho}$ can be calculated with semi-classical Boltzmann transport theory for corresponding scattering mechanisms, the $PF_\perp$ can be theoretically estimated to evaluate the thermoelectric performance of certain band structures. The thermoelectric transport governing equations for the $p\times n$-type transverse thermoeletrics are the same as other transverse thermoelectric systems, and can be solved numerically with a normalized notation as discussed in Section 4.2.1.

4.4. $p \times n$-type transverse thermoelectrics candidates

The signature of $p \times n$-type transverse thermoelectrics is the strongly anisotropic Seebeck tensor, which arises from the anisotropic ambipolar conductivity ratio of electrons and holes. We identified three classes of materials that can potentially be good candidates for $p \times n$-type transverse thermoelectrics: superlattices with engineered anisotropic band structure, materials with "cross-hatched" p and n-type conduction channels, and bulk crystals with ambipolar Seebeck anisotropy. The former two classes can be artificially engineered, and thus will be the focus of our study in this section.

4.4.1. Superlattices with anisotropic band structure

The anisotropic ambipolar conductivity ratio of electrons and holes in $p \times n$ thermoelectric systems can be realized by engineering the carrier band structure of intrinsic semiconductor superlattices. This will be demonstrated here by engineering of a superlattice in the InAs/GaSb type-II superlattice (T2SL) system, with so-called broken-gap alignment. The work in this section has been published in Journal of Electronic Materials [**123**].

Anisotropic band structure can induce anisotropic conductivity, as determined by the effective mass tensor, the deformation potential constant tensor if strain exists, and any anisotropic scattering. If one can engineer the band structure so that the electron band and hole band have markedly different anisotropy, a large anisotropic ambipolar conductivity ratio can be realized and may lead to a large Seebeck anisotropy. Narrow gap ($E_g \sim k_B T$) materials will be preferred for this method, because both electrons and holes have to conduct and large-bandgap intrinsic materials will lead to small electrical conductivity and thus small figure-of-merit.

InAs/GaSb T2SL has a bandgap that can be continuously tuned to zero. As shown in Fig. 4.11(a), the GaSb valence band lies energetically above the InAs conduction band, thus by varying the electron well width d_{InAs} and the hole well width d_{GaSb}, the quantum confinement energy can tune the gap between the electron and hole bands. This tunable bandgap grants the T2SL system the potential for operation at different temperatures with appropriate superlattice period corresponding to $E_g \sim k_B T$.

The anisotropic ambipolar conductivity ratio arises in this case from the different anisotropy of the electron and hole effective mass tensors. The effective mass is inversely proportional to the curvature of the parabolic energy-crystal momentum dispersion. As shown in the calculated band structure(Fig. 4.11b) [**15**], holes have relatively large in-plane effective mass and infinite out-of-plane mass in the layer-to-layer tunneling direction whereas the electron effective mass is small and almost isotropic. With an overall moderate p-type Fermi energy, we can make holes dominate the in-plane conduction and electrons dominate the cross-plane conduction, thus realizing a strongly anisotropic Seebeck tensor and a transverse Seebeck coefficient up to $S_{xy} = 320\,\mu\mathrm{V/K}$ [**12**].

There are several major differences of note between the $p \times n$ transverse thermoelectrics based on T2SL in this section and the two-phase stacked synthetic transverse thermoelectrics of Section A. Firstly, the T2SL is a single crystal with nanoscale layers, while the two-phase stacked synthetic material consists of millimeter-thick layers of two materials with differing lattice structures, which are mechanically and electrically bonded together. Whereas the stacked synthetic TTE structure has layer thicknesses that prevent it from scaling below the $\sim$ cm scale, the T2SL and other transverse thermoelectric crystals can be easily scaled to the micron scale. Another key difference is the origin of

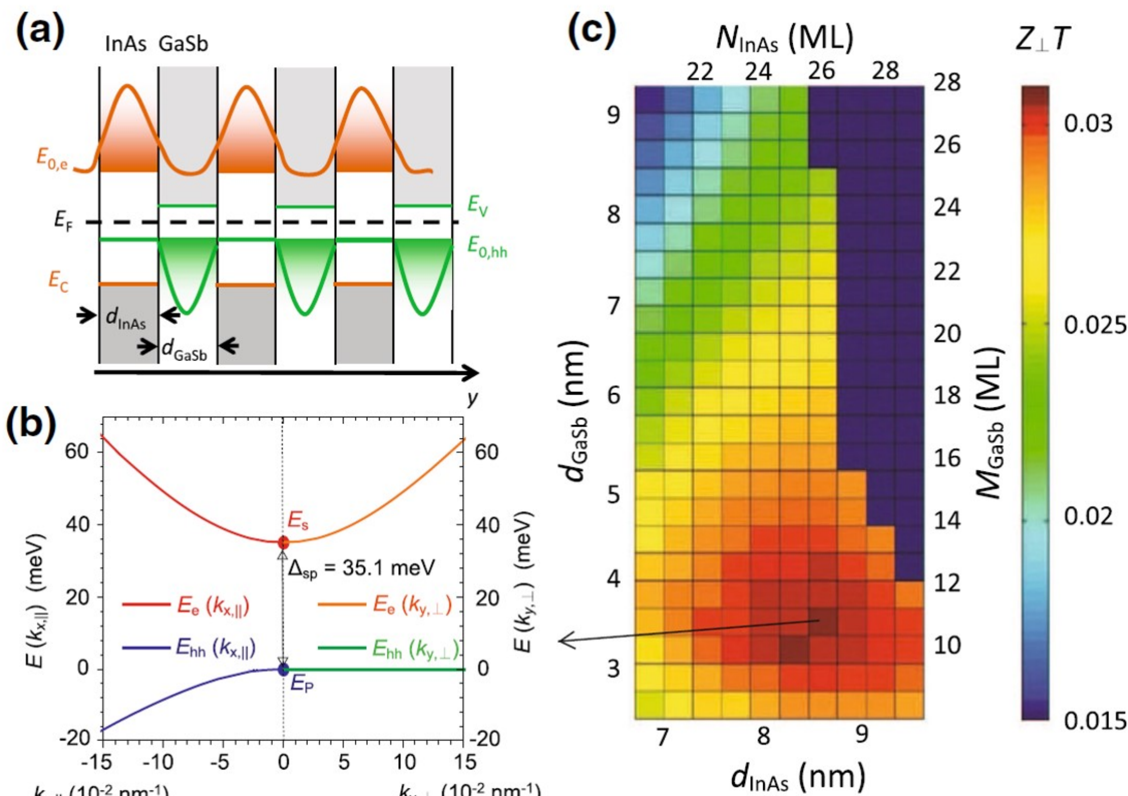

Figure 4.11. (a) Band alignment of T2SL, where the grey color indicates the forbidden bandgap. GaSb valence band E_V (green) lies energetically above the InAs conduction band E_C (orange). E_F is the Fermi energy. $E_{0,e}$ is the ground energy for electron band, and $E_{0,hh}$ is the the ground energy for heavy hole band. (b) Dispersions simulated using nextnano $8 \times 8k \cdot p$ envelope function method [13, 14]. The in-plane dispersion is to the left of $k = 0$, and the out-of-plane dispersion to the right of $k = 0$. $\Delta_{sp} = E_s - E_p$ is the $s - p$ band difference. (c) Plot of the optimized $Z_\perp T$ at 300 K as a function of different InAs and GaSb layer thicknesses [15].

the anisotropic Seebeck coefficient. In $p \times n$ TTE, electrons and holes conduct in parallel in all directions, and the anisotropic ambipolar electrical conductivity ratio induces the Seebeck anisotropy, with electrons and holes subjected to the same temperature gradient. On the other hand in the stacked synthetic TTE, the layers have series resistance in

the cross-plane direction and parallel conduction in the in-plane direction, and it is the difference in both electrical and thermal conductivities of the two materials that leads to the Seebeck anisotropy [**111**]. As pointed out in the comparison in Section A and 4.3, the equations that give rise to the transverse Seebeck coefficient are completely different.

With the band simulation and thermal conductivity measurement results, $Z_{\perp}T$ of different InAs and GaSb thicknesses can be estimated (Fig. 4.11c). The anisotropic electrical conductivity of the T2SL can also be characterized with the triple stripline method introduced in Chapter 2, but here for simplicity we use the simulated values directly. A theoretical estimate of the optimal $Z_{\perp}T \sim 0.03$ for this material system has been predicted. Although this value is still relatively small compared with conventional longitudinal thermoelectrics, the real advantage is in scalability, whereby a maximum cooling up to $\Delta T = 9.1$ K at room temperature is expected [**12**] in an exponentially tapered geometry (Fig. 4.3b), which can be scaled down to micron size. This is competitive with the recent experimental results in on-chip cooling with much more complicated superlattice-based longitudinal thin-film thermoelectrics, which cooled by only $\Delta T \sim$7.1 K [**110**].

4.4.2. Cross-hatched $p \times n$ materials

The second artificial approach to creating a $p \times n$ thermoelectric system is to fabricate aligned p-type conduction channels and orthogonally aligned n-channels to form a "cross-hatched" structure (Fig. 4.12a). The inherent anisotropic conduction within each one-dimensional (1D) channel enables us to have $p \times n$ type electrical conduction (Fig. 4.12b) for the cross-hatched channel array, and thus an anisotropic Seebeck tensor. By alternatively cross-hatching multiple p and n channel array layers, an aritificial $p \times n$ structure

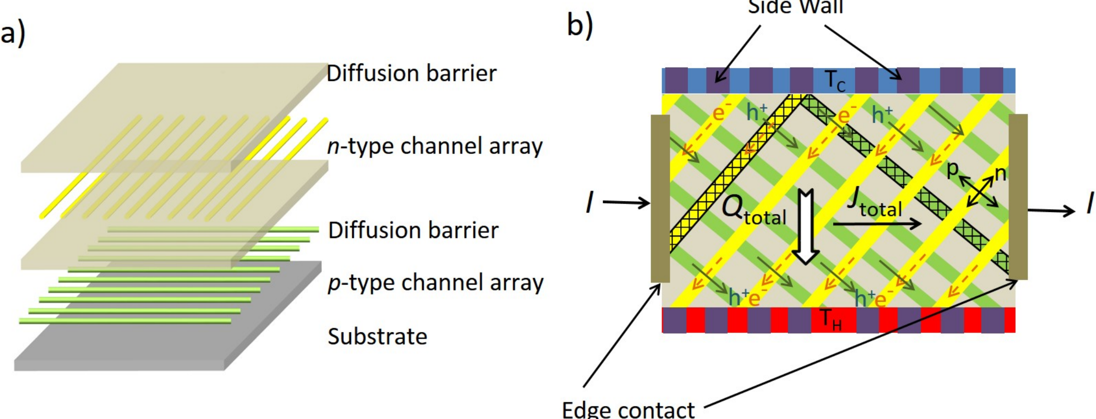

Figure 4.12. Cross-hatched $p \times n$ transverse thermoelectrics. (a) By alternatively aligning n-type conduction channel array and orthogonally oriented p-type conduction channel array, $p \times n$ conduction is realized. (b) A schematic diagram of cross-hatched transverse thermoelectric cooler. With an applied current J, electron-hole pairs are generated at top surface absorbing heat and recombine at the bottom giving off heat, cooling top surface.

can be fabricated. It has to be noted that the diffusion buffer layer between p and n layers in Fig. 4.12(b) is optional, since the device would function equally well if electrons and holes equilibrated at every point in the device. In any case, the depleted region at the $p-n$ junction between two layers may serve as a diffusive barrier layer.

The 1D conduction channels in the cross-hatched $p \times n$ material can be fabricated with nanowires, 3D-printed graphene/polymer stripes, or ion-implantation isolated bulk crystal channels as described in Chapter 3. Theoretically, the 1D conduction channels can be fabricated from any material, as long as the aspect ratio is large enough. 1D nanostructures such as nanowires (NWs) and nanotubes (NTs) are natural candidates, due

to the large aspect ratio, the possibility to make thin-film thermoelectrics, and the good thermoelectric properties compared with bulk materials. The conduction channel arrays can also be defined by other approaches, for example, the 3D-printed graphene/polymer stripes can form p-type aligned channels, and the ion implantation isolation can be used to define both n and p-type aligned conduction channel arrays in bulk crystals. An actual cross-hatched $p \times n$ device can even have a composite structure with n and p layers fabricated with different techniques, for example, p-type 3DG stripes on top cross-hatching with the n-type AlGaAs conduction channels at the bottom.

4.4.3. Bulk crystals with ambipolar Seebeck anisotropy

The classes of material with ambipolar Seebeck anisotropy include materials with open Fermi surfaces, materials with closed Fermi surfaces but with opposing curvature and sharp singularities, and narrow-gap semiconductors with anisotropic band structures. Weak ambipolar Seebeck anisotropy has been reported for materials with open Fermi surfaces, for example single-crystal rhenium ($\Delta S < 10$ μV/K) [**124**], $PdCoO_2$, $PtCoO_2$ and related materials ($\Delta S \approx 100$ - 200 μV/K, but $S_p < 20$ μV/K) [**125**]. Beryllium has also been reported to have weak ambipolar Seebeck anisotropy below 600 K with $\Delta S < 10$μV/K [**126**]; this was attributed to singularities of its strongly anisotropic Fermi surfaces. Two more noteworthy materials are narrow-gap semiconductors $ReGe_xSi_{1.75-x}$ [**127**] with $S_p = +200$ μV/K and $S_n = -220$ μV/K in a and c directions, and $CsBi_4Te_6$ [**128**] with $S_p = +100$ μV/K and $S_n = -80$ μV/K in the b and c directions, respectively.

Initial calculation based on published data shows that the largest transverse figure-of-merit for bulk crystals is $Z_{\perp}T \approx 0.025$ for $CsBi_4Te_6$ (experimental) and $Z_{\perp}T \approx 0.04$

(theoretical) at $T = 300$ K, and $Z_{\perp}T \approx 0.36$ for $ReSi_{1.75}$ (experimental) at $T = 1060$ K. $p \times n$-type bulk crystals with higher transverse figure of merit at room temperature are yet to be discovered. The transverse figure-of-merit of bulk crystals with ambipolar Seebeck anisotropy is not significantly larger than those with unipolar anisotropic Seebeck tensor as reviewed in Appendix A. However, in the anisotropic crystals with a unipolar anisotropic Seebeck tensor, there is always an accompanying longitudinal component of the induced heat flow (or electrical current) in a Peltier (or Seebeck) effect, which reduces the efficiency of the transverse thermoelement. For proper transverse performance, an ambipolar Seebeck tensor is desired.

4.5. Cross-hatched $p \times n$ layer interconnect model

Cross-hatched $p \times n$ structure based on the bulk crystal can be realized by alternatively stacking the n and p layers with anisotropic conductivity created with ion implantation isolation. However, the thermoelectric performance of such $p \times n$ structures will depend on the degree of electrical equilibration between the n and p layers. In this section, we study two extreme cases, the short-circuit model and the open-circuit model, the results of which set limits for the expected performance of the actual $p \times n$ structure.

The thermoelectric transport inside the cross-hatched $p \times n$ structure involves diffusion, generation, and recombination of electrons and holes. The n and p layer channel arrays form pn-junctions wherever the cross-hatching occurs. A temperature gradient applied 45° to the channel direction causes a driving force to the free carriers from the hot to the cold part of the structure. The resulting current alters the local carrier balance between generation and recombination and leads to enhanced generation of electron-hole

pairs in the hot part and increased recombination in the cold part of the pn-junctions. This is similar to the pn-junction thermoelectric generator [129–131] in longitudinal thermoelectrics. However, in the cross-hatched $p \times n$ structure, the electrons and holes diffuse along orthogonal directions as confined by the conduction channels (Fig. 4.12b), and accumulate at opposite edges.

For simplicity, we consider two extreme cases, the first of which is the short-circuit model, in which the local vertical pn-junction effective resistance is much smaller than the in-plane conduction channel resistance. The second case is the open-circuit model, in which the pn-junctions are fully depleted, and the n and p channels are electrically isolated except for at edges.

4.5.1. Short-circuit model

In the short-circuit model, the electrical potential of electrons and holes at pn-junctions away from edges is identical, which indicates that they are subjected to the same local electric field. Assuming a strong mechanical bond between layers, the n and p channels can be regarded as thermally shorted at pn-junctions as well. Thus the system can be approximated as an ideal $p \times n$-type transverse thermoelectric system as studied in Section 4.3. The metric to evaluate the performance of the cross-hatched $p \times n$ structure is the transverse figure of merit, with the maximum value:

$$Z_\perp T = Z_{xy}(\theta_\perp)T = \frac{(S_p - S_n)^2 T}{(\sqrt{\rho_n \kappa_n} + \sqrt{\rho_p \kappa_p})^2}, \tag{4.30}$$

whereby the Seebeck coefficient S, resistivity ρ and thermal conductivity κ for electrons and holes are measured along the channel directions of n and p-layers, respectively.

4.5.2. Open-circuit model

The open-circuit model assumes the n and p conduction channels are electrically isolated at the depleted vertical pn-junctions within the layer area. Only at the edges are the n- and p-layers shorted by metal contacts. As shown in Fig. 4.13(a). n and p conduction channels are cross-hatched with channel orientation forming angle θ_n and θ_p with the x axis, respectively. A temperature gradient is applied in the $+x$ direction, which generates a transverse Seebeck voltage between top and bottom contacts that drives a current I through an external load resistor R_L.

This cross-hatched structure consists of multiple thermocouples, each formed by one pair of p and n conduction channels that overlap at the left or right edges, as marked by the dashed lines in Fig. 4.13(a). Assuming the p and n channels perfectly overlap at left and right edges with overlapped region width d_0 along the y axis, the electrical conduction between top and bottom contacts can be regarded as the parallel connection of multiple conductions paths. Each conduction path from bottom to top is formed by multiple thermocouples connected in series. Assuming the device length L is much larger than its width W, the number of parallel conduction paths and the average number of thermocouples in each conduction path are:

$$N_{||} = \frac{W}{w_n} + \frac{W}{w_p} = W\left(\frac{\sin\theta_n}{d_n} + \frac{\sin\theta_p}{d_p}\right) = \frac{W}{d_0}\left(\tan\theta_n + \tan\theta_p\right) \tag{4.31}$$

and

$$N = \frac{L}{W\left(\tan\theta_n + \tan\theta_p\right)}, \tag{4.32}$$

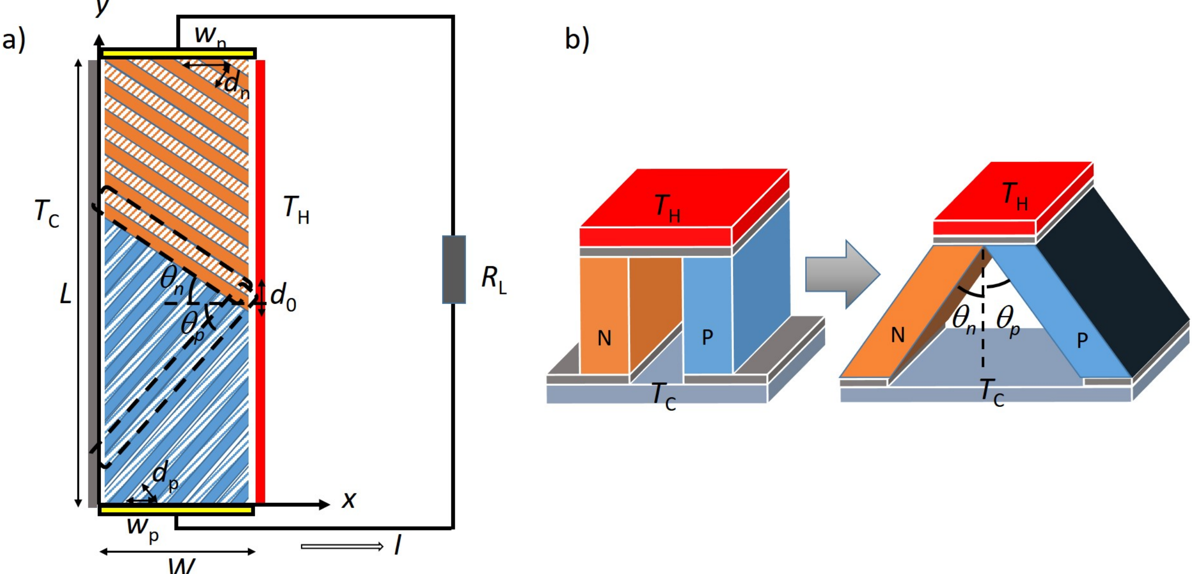

Figure 4.13. (a) Diagram of a cross-hatched $p \times n$ Seebeck generator. The p-type (blue strips) and n-type (orange strips) conduction channels are aligned with angle θ_p and θ_n to x axis, respectively. With a temperature difference applied to the left and right surfaces, a transverse Seebeck voltage is generated in the y direction, driving a current I through the load resistor R_L. (b) The formation of tilted longitudinal thermocouple. In the open-circuit model, one pair of p and n channels that overlap at the left/right edges effectively forms a tilted longitudinal thermocouple.

respectively. Here d_n and d_p are the pitch width of n and p conduction channels, and w_n and w_p are the width of the contacting area between the conduction channel and top/bottom edges.

The efficiency of this transverse Seebeck generator can be calculated assuming a uniform temperature gradient along x direction:

$$\eta = \frac{W_{R_L}}{Q_H} = \frac{I^2 R_L}{K\Delta T + (S_p - S_n)(T_H I_0)\frac{L}{d_0} - \frac{1}{2}I^2 R}, \tag{4.33}$$

whereby W_{R_L} is the output power to the load resistor, Q_H is the heat flow from the hot side (right edge), I is the total current, I_0 is the current for each parallel conduction path, K is the thermal conductance between left and right edges and R the inner resistance between top and bottom contacts. This equation can be reduced to:

$$\eta = \frac{u\Delta T}{\frac{(1+u)^2}{Z} + T_H(1+u) - \frac{1}{2}\Delta T}, \tag{4.34}$$

where $u = R_L/R$ and $Z = \frac{N^2(S_p-S_n)^2}{KR}$. To maximize the efficiency, the transverse figure of merit parameter Z has to be maximized.

Assuming the thermal conduction between hot and cold edges are dominated by phononic heat flow, the thermal conductance can be approximated as $K = \kappa_l \frac{Lt}{W}$, whereby κ_l is the lattice thermal conductivity and t is the thickness of n and p layers. Thus we have:

$$Z = \frac{(S_p - S_n)^2}{\kappa_l} \frac{1}{\frac{\rho_n}{\cos^2\theta_n} + \frac{\rho_p}{\cos^2\theta_p}}, \tag{4.35}$$

which is maximized to be

$$Z_{\max} = \frac{(S_p - S_n)^2}{\kappa_l(\rho_n + \rho_p)} \text{ when } \theta_\text{n}, \theta_\text{p} \to 0. \tag{4.36}$$

The essence of the open-circuit model is to realize an overall transverse Seebeck effect with tilted longitudinal thermocouples. As shown in Fig. 4.13(b), the unit thermocouple in the cross-hatched structure can be formed by tilting the two legs of a longitudinal thermocouple. In the extreme case $\theta_n, \theta_p \to 0$, the cross-hatched structure reduces to

parallel longitudinal thermocouples along x axis, and the resistance between top and bottom edges are $R \to \infty$, thus $u = R_L/R \to 0$, which leads to $\eta \to 0$. To achieve the $Z_{\max}$ in Eq. 4.36, $R_L \to$ inf is required.

The actual thermoelectric transport in the cross-hatched $p \times n$ structure will not strictly follow the short-circuit or the open-circuit models, instead, it will be somewhere in-between. The two models analyzed above provide two bounds of the transverse figure of merit as defined in Eq. 4.30 and 4.35. By comparing the Z value of the actual device, which can be calculated with measured total transverse Seebeck coefficient S_{xy}, longitudinal resistivity ρ_{xx} and thermal conductivity κ_{yy} via $Z = S_{xy}^2/\rho_{xx}\kappa_{yy}$, to those predicted by the two models, a weighting coefficient can be determined so that the actual thermoelectric transport can be understood as a weighted combination of two models.

4.6. Cross-hatched $p \times n$ AlGaAs fabrication progress and future work

To experimentally demonstrate cross-hatched $p \times n$ materials, the fabrication of $p \times n$ structure based on $Al_{0.42}Ga_{0.58}As$ is attempted for a proof-of-concept transverse Seebeck measurement. AlGaAs is chosen due to its large Seebeck coefficient for both n and p-type doped materials [**99**]. The Seebeck coefficient of n-type $Al_xGa_{1-x}As$ is maximized with the aluminum mole fraction $x = 0.42$, which yields multiple degenerate valleys of the conduction bands.

4.6.1. Fabrication flow

The overall fabrication flow is shown in Fig. 4.14. A p-type $Al_{0.42}Ga_{0.58}As$ layer is grown by molecular beam epitaxy (MBE) on top of semi-insulating GaAs (100) substrate with

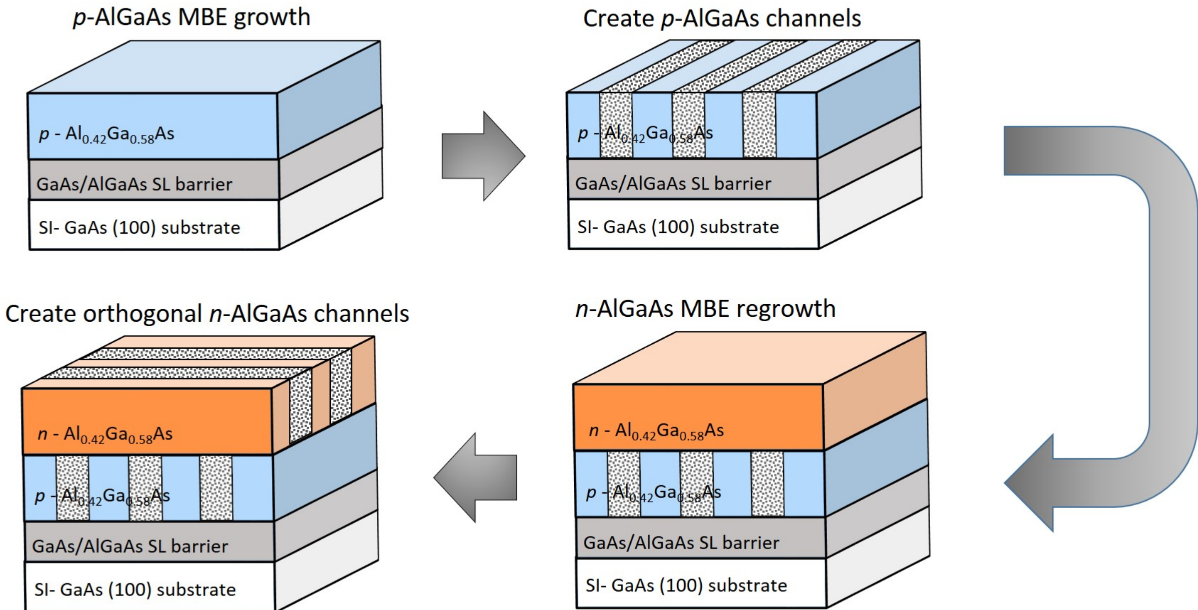

Figure 4.14. The overall fabrication flow for cross-hatched $p \times n$ AlGaAs crystal. The p and n-type conduction channels are created via ion implantation isolation.

a GaAs/AlGaAs superlattice buffer layer to reduce the lattice mismatch. Then p-type conduction channels are created via ion implantation isolation, which is followed by MBE regrowth of another n-type $Al_{0.42}Ga_{0.58}As$ layer on top. And finally n-type conduction channels orthogonal to the p-type channels are fabricated by ion implantation isolation.

4.6.2. $p + n$-AlGaAs

The MBE regrowth quality and its influence on the Seebeck coefficient of the n and p layers are studied by growing a $p + n$ structure without ion implantation isolation. The growth protocol is shown in Fig. 4.15, the $d = 500$ nm thick p-$Al_{0.42}Ga_{0.58}As$ is first grown with MBE, with a 25 nm thick undoped GaAs cap layer on top. Then another $d = 500$ nm thick n-$Al_{0.42}Ga_{0.58}As$ is grown with another highly doped thin GaAs cap layer. One

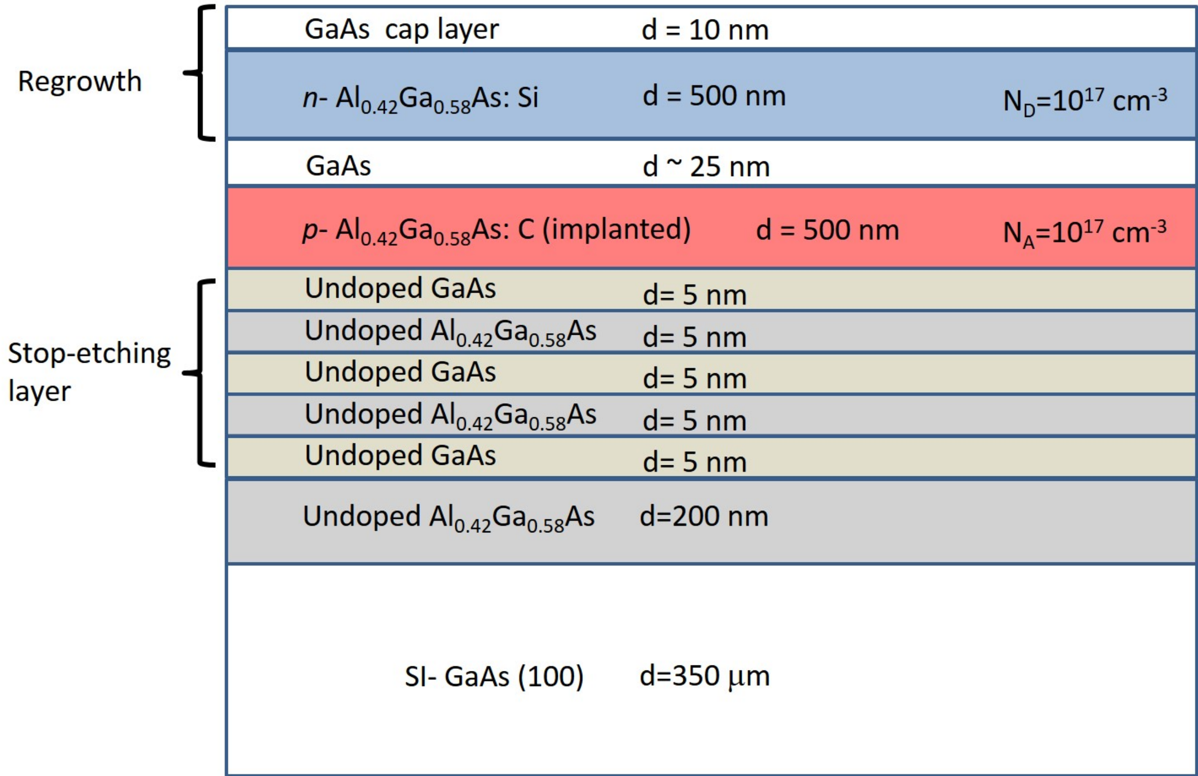

Figure 4.15. Growth protocol of the $p+n$ bilayer $Al_{0.42}Ga_{0.58}As$ structure.

group of samples have both p and n layers grown at once, while another group of samples is taken out of the MBE chamber and put in air for 12 hours and then the n layer is regrown.

Ultrasonic bath with concentrated H_2SO_4 kept below 300 K is used to process the GaAs cap surface before regrowth to reduce oval defects [**132**]. The undoped GaAs layer between the p and n-AlGaAs layers function as a cap layer that protects the AlGaAs surface before regrowth. The cap thickness $d \sim 25$ nm is chosen since atomic force microscopy (AFM) study shows that the etching depth of GaAs in concentrated H_2SO_4 (96 %) with ultrasonic bath remains below 10 nm after 10 minutes.

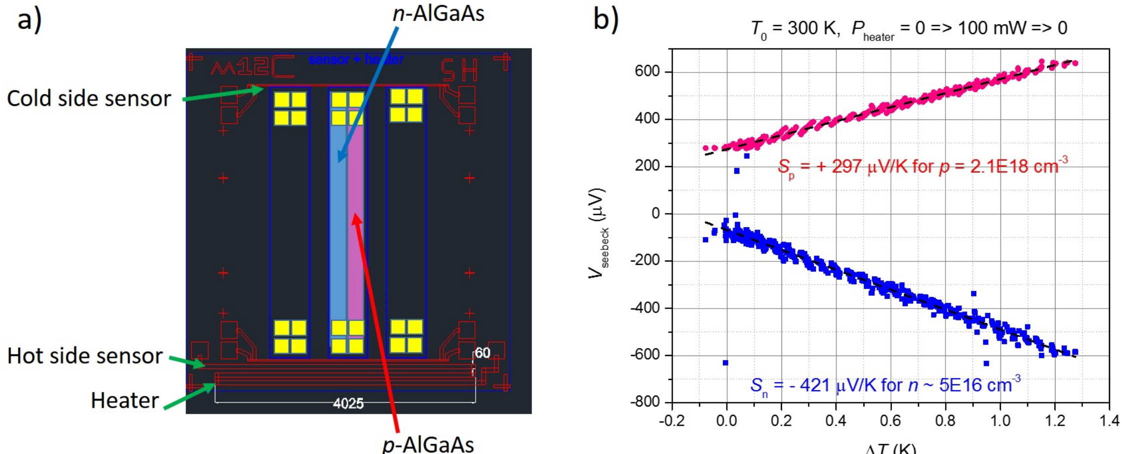

Figure 4.16. (a) Photomask patterns for on-chip Seebeck measurement device. (b) Example Seebeck measurement result for the $p + n$ AlGaAs structure with both layers grown at once. S_p and S_n are directly extracted from the slop of the Seebeck voltage measured at two outer contacts, which require further scaling to compensate for the over-estimated temperature difference.

The Seebeck coefficient for the p and n-AlGaAs layer and the total Seebeck coefficient of two layers (pn-junction thermoelectrics) are measured with an on-chip Seebeck measurement setup. As shown in Fig. 4.16(a), the on-chip Seebeck measurement setup is formed by two resistor temperature sensors on the hot and cold sides, a meander-shaped resistance heater, and the bar-shaped mesa-etched sample between the two sensors. Both the sensor and the heater are fabricated with gold filament, which has a linear resistance-temperature dependence at room temperature. Half of the bar area is etched down to the p-AlGaAs surface, and ohmic contacts for both n and p-AlGaAs layers at the two ends are used to measure the Seebeck voltage.

Figure 4.16b shows the measured Seebeck voltage as a function of temperature difference for $n-$ and p-AlGaAs layers for the $p + n$-AlGaAs structure with both layers grown

in MBE chamber at once. The Seebeck coefficient is extracted from the slope. The actual temperature difference between the two metal contacts is slightly smaller than that measured by the two temperature sensors. Assuming the temperature distribution is roughly linear from the hot to cold side, we can simply scale the measured Seebeck coefficient with a geometric correction factor $d_{\text{sensor}}/d_{\text{contacts}}$. The results are shown in Table. 4.1.

Table 4.1. The geometrically corrected Seebeck coefficient for p+n-AlGaAs and single layer AlGaAs.

Sample	p (cm^{-3})	n (cm^{-3})	S_p (μV/K)	S_n (μV/K)	S_{pn} (μV/K)
$p+n$-AlGaAs (grown at once)	2.1E18	≤5.0E16	+345	−490	+780
$p+n$-AlGaAs (regrown)	1.9E18	≤5.3E17	+440	−170	+370
p-AlGaAs	1.6E18	N/A	+370	N/A	N/A
n-AlGaAs	N/A	5.0E16	N/A	−630	N/A

The measured Seebeck coefficient of the n-AlGaAs in $p+n$-AlGaAs structure ($S_n = -490$ μV/K for all grown at once and $S_n = -170$ μV/K for regrown) drastically deviates from that of the single layer n-AlGaAs ($S_n = -630$ μV/K). This happens when the pn-junction resistance is much smaller than the n-layer sheet resistance. Similar to the open-circuit model discussed in the last section, when the p and n-AlGaAs layers are electrically isolated by the depleted pn-junction, the total Seebeck coefficient $S_{pn} \approx S_p - S_n$. Comparing S_{pn} for the $p+n$-AlGaAs structure to $S_p - S_n$ for single layer AlGaAs we can see that the grown-at-once sample is much closer to the open-circuit model than the regrown sample.

The inconsistency between all-grown-at-once and regrown $p+n$-AlGaAs Seebeck coefficients can be attributed to the inconsistent doping of the n-AlGaAs layer. As shown in

Table. 4.1, the carrier density measured by Hall measurement indicates that the electron density of the regrown sample is one order higher than that of the all-grown-at-once sample. Such an inconsistency can be caused by accidental change of MBE growth condition such as the silicon filament current. Also both the electron and hole density deviate from the aimed value in the growth protocol (10^{17} cm^{-3}). This is because the doping in the MBE chamber was calibrated with GaAs, instead of $Al_{0.42}Ga_{0.58}As$. A new round of doping calibration and growth of the $p+n$-AlGaAs structure are required to achieve aimed doping density and consistent Seebeck coefficient for the regrown sample.

4.6.3. Future work

The fabrication of the cross-hatched $p\times n$ AlGaAs structure requires further experimental effort. Firstly, the doping density of both n and p-type AlGaAs need to be re-calibrated to achieve aimed carrier density with the MBE system. Only when that is done, the all-grown-at-once and regrown $p+n$-AlGaAs structure can be attempted again to examine the total Seebeck coefficient of the pn-junction thermoelectrics, which will determine whether the short-circuit model or the open-circuit model fits the thermoelectric transport in the cross-hatched $p \times n$ structure based on AlGaAs.

Secondly, the cross-hatched p and n conduction channels need to be fabricated in the two AlGaAs layers via ion implantation isolation. Figure 4.17a) shows the overview of the wafer-scale photolithography patterns for the p and n layer ion implantation. Different regions of the wafer can be used for following Seebeck characterization of single n-layer, single p-layer and $p \times n$ structure. Transverse Seebeck coefficient of the cross-hatched $p \times n$ structure needs to be measured. It has to be noted that to avoid shorting the

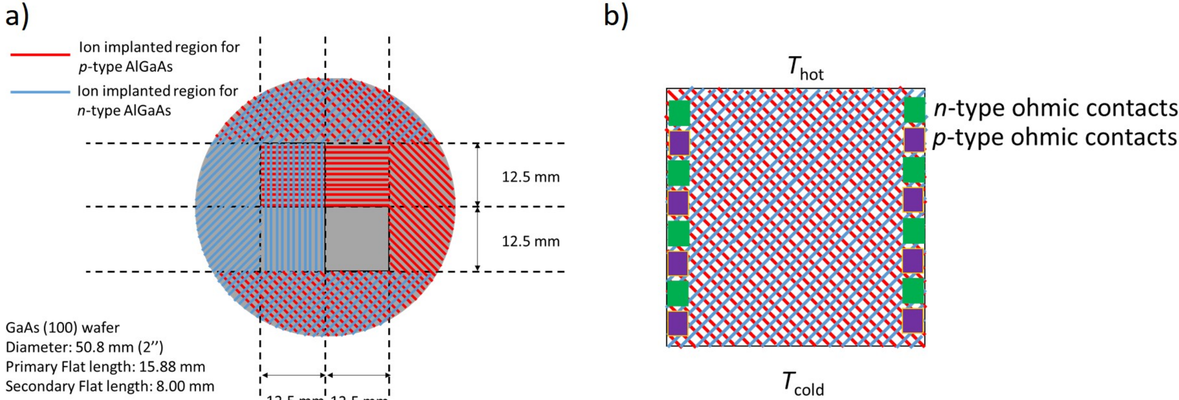

Figure 4.17. (a) The wafer-scale photolithography patterns for cross-hatched $p \times n$ AlGaAs. (b) Transverse Seebeck measurement device structure. n and p-type ohmic contacts are alternatively deposited on left and right edges and to avoid shorting the temperature difference between top and bottom edges.

temperature difference between the hot and cold side, alternative scattered n and p-type ohmic contacts should be fabricated at the sample electrical contact edges, as shown in Fig. 4.17(b). In the Seebeck measurement, the scattered ohmic contacts on the two edges will be shorted to other contacts on the same edge with external cables.

Finally, the aluminum composition ratio x and the doping density for both electrons and holes can be optimized to achieve the maximum transverse figure of merit. Theoretical study [**133**] has shown that for single-layer n-type $Al_xGa_{1-x}As$, the optimum x that maximizes the figure of merit at room temperature is $x = 0.31$ with predicted optimal doping density 1.44×10^{19} cm^{-3}.

Bibliography

[1] GA Umana-Membreno, B Klein, H Kala, J Antoszewski, N Gautam, MN Kutty, E Plis, S Krishna, and L Faraone. Vertical minority carrier electron transport in p-type inas/gasb type-ii superlattices. *Applied Physics Letters*, 101(25):253515, 2012.

[2] E Stilp, A Suter, T Prokscha, Z Salman, E Morenzoni, H Keller, P Pahlke, R Hühne, Christian Bernhard, Ruixing Liang, et al. Controlling the near-surface superfluid density in underdoped yba2cu3o6+ x by photo-illumination. *Scientific reports*, 4, 2014.

[3] Myung-Jin Yim and Kyung-Wook Paik. Design and understanding of anisotropic conductive films (acfs) for lcd packaging. In *Polymeric Electronics Packaging, 1997. Proceedings., The First IEEE International Symposium on*, pages 233–242. IEEE, 1997.

[4] Panikkanvalappil R Sajanlal, Theruvakkattil S Sreeprasad, Akshaya K Samal, and Thalappil Pradeep. Anisotropic nanomaterials: structure, growth, assembly, and functions. *Nano Reviews & Experiments*, 2, 2011.

[5] Tejas A Shastry, Jung-Woo T Seo, Josue J Lopez, Heather N Arnold, Jacob Z Kelter, Vinod K Sangwan, Lincoln J Lauhon, Tobin J Marks, and Mark C Hersam. Large-area, electronically monodisperse, aligned single-walled carbon nanotube thin films fabricated by evaporation-driven self-assembly. *Small*, 9(1):45–51, 2013.

[6] Saewon Kang, Taehyo Kim, Seungse Cho, Youngoh Lee, Ayoung Choe, Bright Walker, Seo-Jin Ko, Jin Young Kim, and Hyunhyub Ko. Capillary printing of highly aligned silver nanowire transparent electrodes for high-performance optoelectronic devices. *Nano letters*, 15(12):7933–7942, 2015.

[7] Per-Olof Persson and Gilbert Strang. A simple mesh generator in matlab. *SIAM review*, 46(2):329–345, 2004.

[8] Arnaud Robert-Peillard and Slava V Rotkin. Modeling hysteresis phenomena in nanotube field-effect transistors. *IEEE transactions on nanotechnology*, 4(2):284–288, 2005.

[9] James F Ziegler and Jochen P Biersack. The stopping and range of ions in matter. In *Treatise on Heavy-Ion Science*, pages 93–129. Springer, 1985.

[10] H Scherrer, S Scherrer, and DM Rowe. *Thermoelectric Handbook–Macro to Nano*. Taylor & Francis, 2006.

[11] Yu G Gurevich, GN Logvinov, Oscar Angeles Fragoso, and JL del RioV. Lowest temperature at thermoelectric cooling. In *2007 4th International Conference on Electrical and Electronics Engineering*, 2007.

[12] Chuanle Zhou, S Birner, Yang Tang, K Heinselman, and M Grayson. Driving perpendicular heat flow:(p× n)-type transverse thermoelectrics for microscale and cryogenic peltier cooling. *Physical review letters*, 110(22):227701, 2013.

[13] *nextnano3*.

[14] CH Grein, PM Young, ME Flatté, and H Ehrenreich. Long wavelength inas/ingasb infrared detectors: Optimization of carrier lifetimes. *Journal of Applied Physics*, 78(12):7143–7152, 1995.

[15] Chuanle Zhou. *Transverse p×n- type thermoelectrics: type II superlattices and their thermal conductivity characterization*. PhD thesis, Northwestern University, 2013.

[16] Guihua Yu, Anyuan Cao, and Charles M Lieber. Large-area blown bubble films of aligned nanowires and carbon nanotubes. *Nature nanotechnology*, 2(6):372–377, 2007.

[17] Yung Joon Jung, Swastik Kar, Saikat Talapatra, Caterina Soldano, Gunaranjan Viswanathan, Xuesong Li, Zhaoling Yao, Fung Suong Ou, Aditya Avadhanula, Robert Vajtai, et al. Aligned carbon nanotube-polymer hybrid architectures for diverse flexible electronic applications. *Nano letters*, 6(3):413–418, 2006.

[18] Jie-Feng Gao, Ding-Xiang Yan, Bo Yuan, Hua-Dong Huang, and Zhong-Ming Li. Large-scale fabrication and electrical properties of an anisotropic conductive polymer composite utilizing preferable location of carbon nanotubes in a polymer blend. *Composites Science and Technology*, 70(13):1973–1979, 2010.

[19] Robert E Newnham. *Properties of materials: anisotropy, symmetry, structure*. Oxford University Press on Demand, 2005.

[20] Hsin Wang, Wallace D Porter, Harald Böttner, Jan König, Lidong Chen, Shengqiang Bai, Terry M Tritt, Alex Mayolet, Jayantha Senawiratne, Charlene Smith, et al. Transport properties of bulk thermoelectricsan international round-robin study,

part i: Seebeck coefficient and electrical resistivity. *Journal of electronic materials*, 42(4):654–664, 2013.

[21] L van der PAUYV. A method of measuring specific resistivity and hall effect of discs of arbitrary shape. *Philips Res. Rep.*, 13:1–9, 1958.

[22] LJ van der Pauw. Determination of the resistivity tensor and hall tensor of anisotropic conductors. *Phillips Res. Repts*, 16:187–195, 1961.

[23] WLV Price. Electric potential and current distribution in a rectangular sample of anisotropic material with application to the measurement of the principal resistivities by an extension of van der pauw's method. *Solid-State Electronics*, 16(7):753–762, 1973.

[24] O Bierwagen, R Pomraenke, S Eilers, and WT Masselink. Mobility and carrier density in materials with anisotropic conductivity revealed by van der pauw measurements. *Physical Review B*, 70(16):165307, 2004.

[25] J Kleiza and V Kleiza. A method for measuring an electric conductivity tensor of plane media. *Elektronika ir Elektrotechnika*, 59(3), 2005.

[26] Jonas Kleiza, Mifodijus Sapagovas, and Vytautas Kleiza. The extension of the van der pauw method to anisotropic media. *Informatica*, 18(2):253–266, 2007.

[27] S Ašmontas, V Kleiza, and J Kleiza. A method for measuring the specific electrical conductivity of an anisotropically conductive medium. *Acta Physica Polonica A*, 113(6):1559–1569, 2008.

[28] Kasper A Borup, Karl FF Fischer, David R Brown, G Jeffrey Snyder, and Bo B Iversen. Measuring anisotropic resistivity of single crystals using the van der pauw technique. *Physical Review B*, 92(4):045210, 2015.

[29] A Haddadi, G Chen, R Chevallier, AM Hoang, and M Razeghi. Inas/inas1- xsbx type-ii superlattices for high performance long wavelength infrared detection. *Applied Physics Letters*, 105(12):121104, 2014.

[30] C Cervera, JP Perez, R Chaghi, JB Rodriguez, P Christol, Leszek Konczewicz, and Sylvie Contreras. Transport measurements on inas/gasb superlattice structures for mid-infrared photodiode. In *Journal of Physics: Conference Series*, volume 193, page 012030. IOP Publishing, 2009.

[31] F Szmulowicz, S Elhamri, HJ Haugan, GJ Brown, and WC Mitchel. Demonstration of interface-scattering-limited electron mobilities in inas/ gasb superlattices. *Journal of applied physics*, 101(4):043706, 2007.

[32] A Rogalski, J Antoszewski, and L Faraone. Third-generation infrared photodetector arrays. *Journal of Applied Physics*, 105(9):091101, 2009.

[33] Manijeh Razeghi, Darin Hoffman, Binh-Minh Nguyen, Pierre-Yves Delaunay, Edward Kwei-wei Huang, Meimei Z Tidrow, and Vaidya Nathan. Recent advances in lwir type-ii inas/gasb superlattice photodetectors and focal plane arrays at the center for quantum devices. *Proceedings of the IEEE*, 97(6):1056–1066, 2009.

[34] WW Bewley, H Lee, I Vurgaftman, RJ Menna, CL Felix, RU Martinelli, DW Stokes, DZ Garbuzov, JR Meyer, M Maiorov, et al. Continuous-wave operation of lambda= 3.25 mum broadened-waveguide w quantum-well diode lasers up to t= 195 k. *Applied Physics Letters*, 76:256, 2000.

[35] EH Aifer, JG Tischler, JH Warner, I Vurgaftman, WW Bewley, JR Meyer, JC Kim, LJ Whitman, CL Canedy, and EM Jackson. W-structured type-ii superlattice long-wave infrared photodiodes with high quantum efficiency. Technical report, DTIC Document, 2006.

[36] Jung-Hui Tsai, Yuan-Hong Lee, Ning-Feng Dale, Jhih-Syuan Sheng, Yung-Chun Ma, and Sheng-Shiun Ye. Application of ingaas/gaas superlattice-base structure for ingap/gaas superlattice-emitter bipolar transistor. *Applied Physics Letters*, 96(6):063505, 2010.

[37] Th Zahner, R Stierstorfer, S Reindl, T Schauer, Alfons Penzkofer, and H Lengfellner. Picosecond thermoelectric response of thin yba 2 cu 3 o 7- δ films. *Physica C: Superconductivity*, 313(1):37–40, 1999.

[38] A Sreekumaran Nair, Zhu Peining, V Jagadeesh Babu, Yang Shengyuan, and Seeram Ramakrishna. Anisotropic tio 2 nanomaterials in dye-sensitized solar cells. *Physical Chemistry Chemical Physics*, 13(48):21248–21261, 2011.

[39] FR Gamble, JH Osiecki, Mo Cais, R Pisharody, FJ DiSalvo, and TH Geballe. Intercalation complexes of lewis bases and layered sulfides: a large class of new superconductors. *Science*, 174(4008):493–497, 1971.

[40] JJ Gu, K Kuwabara, K Tanaka, H Inui, M Yamaguchi, A Yamamoto, T Ohta, and H Obara. Crystal structure and thermoelectric properties of resi 1.75 silicide. In *MRS Proceedings*, volume 753, pages BB6–10. Cambridge Univ Press, 2002.

[41] DDL Chung. Polymer-matrix composites for microelectronics. *Polymers and Polymer Composites(UK)*, 8(4):219–229, 2000.

[42] PT Robinson, V Florescu, G Rosen, and MT Singer. Annual connector & interconnection technol. symp, 1990.

[43] D.D. Johnson. New material technology for high density interconnections. pages 151–165, New York, 1997. IEEE, 3rd Int. Symp. Adv. Pkg. Mater.: Processes, Properties and Interfaces.

[44] L Li and DDL Chung. Z-axis anisotropic electrically conducting polymer-matrix composite film. *Journal of Electronic Packaging*, 119(4):255–259, 1997.

[45] Melburne C LeMieux, Mark Roberts, Soumendra Barman, Yong Wan Jin, Jong Min Kim, and Zhenan Bao. Self-sorted, aligned nanotube networks for thin-film transistors. *Science*, 321(5885):101–104, 2008.

[46] Xiaolin Li, Li Zhang, Xinran Wang, Iwao Shimoyama, Xiaoming Sun, Won-Seok Seo, and Hongjie Dai. Langmuir-blodgett assembly of densely aligned single-walled carbon nanotubes from bulk materials. *Journal of the American Chemical Society*, 129(16):4890–4891, 2007.

[47] Shashank Shekhar, Paul Stokes, and Saiful I Khondaker. Ultrahigh density alignment of carbon nanotube arrays by dielectrophoresis. *ACS nano*, 5(3):1739–1746, 2011.

[48] Si-ping Han, Hareem T Maune, Robert D Barish, Marc Bockrath, and William A Goddard III. Dna-linker-induced surface assembly of ultra dense parallel single walled carbon nanotube arrays. *Nano letters*, 12(3):1129–1135, 2012.

[49] Yunsheng Xu and DDL Chung. Z-axis anisotropic electrical conductor films in adhesive and standalone forms for electrical interconnection. *Journal of electronic materials*, 28(11):1307–1313, 1999.

[50] BV Olson, EA Shaner, JK Kim, JF Klem, SD Hawkins, LM Murray, JP Prineas, ME Flatté, and TF Boggess. Time-resolved optical measurements of minority carrier recombination in a mid-wave infrared inassb alloy and inas/inassb superlattice. *Applied Physics Letters*, 101(9):092109, 2012.

[51] G Strasser, S Gianordoli, L Hvozdara, W Schrenk, K Unterrainer, and E Gornik. Gaas/algaas superlattice quantum cascade lasers at $\lambda \approx 13$ μm. *Applied physics letters*, 75(10):1345–1347, 1999.

[52] TC Harman, PJ Taylor, MP Walsh, and BE LaForge. Quantum dot superlattice thermoelectric materials and devices. *science*, 297(5590):2229–2232, 2002.

[53] Lihong Shi, Donglai Yao, Gang Zhang, and Baowen Li. Large thermoelectric figure of merit in si ge x nanowires. *Applied Physics Letters*, 96:173108, 2010.

[54] Rama Venkatasubramanian, Edward Siivola, Thomas Colpitts, and Brooks O'quinn. Thin-film thermoelectric devices with high room-temperature figures of merit. *Nature*, 413(6856):597–602, 2001.

[55] Yang Tang and M Grayson. Magnetotransport potentials for anisotropic thin films with stripline and ground plane contacts. In *SPIE OPTO*, pages 93700L–93700L. International Society for Optics and Photonics, 2015.

[56] Gilbert De Mey. Potential calculations in hall plates. *Advances in electronics and electron physics*, 61:1–62, 1983.

[57] JP Newsome. Determination of the electrical characteristics of hall plates. *Proc. IEE*, 110(4):653–659, 1963.

[58] T Mimizuka. The accuracy of the relaxation solution for the potential problem of a hall plate with finite hall electrodes. *Solid-State Electronics*, 21(10):1195–1197, 1978.

[59] A Nathan, W Alegreto, H. P. Baltes, and T Sugiyama. Carrier transport in semiconductor magnetic domain detectors. *IEEE Trans. Electron Devices*, ED-34:2077–2085, 1987.

[60] Jian Sun and Jürgen Kosel. *Finite-element modelling and analysis of hall effect and extraordinary magnetoresistance effect*. INTECH Open Access Publisher, 2012.

[61] Bewley L V. *Two-dimensional fields in electrical engineering*. Macmillan Company, New York, 1948.

[62] Tobin A Driscoll and Lloyd N Trefethen. *Schwarz-Christoffel Mapping*, volume 8. Cambridge University Press, 2002.

[63] Jochen Alberty, Carsten Carstensen, and Stefan A Funken. Remarks around 50 lines of matlab: short finite element implementation. *Numerical Algorithms*, 20(2-3):117–137, 1999.

[64] Laszlo Andor, HP Baltes, AROKIA Nathan, and HG Schmidt-Weinmar. Numerical modeling of magnetic-field-sensitive semiconductor devices. *IEEE Transactions on Electron Devices*, 32(7):1224–1230, 1985.

[65] HJ Lee, MS Tse, K Radhakrishnan, K Prasad, J Weng, SF Yoon, X Zhou, and HS Tan. Characterization of ni/ge/au/ni/au contact metallization on algaasingaas heterostructures for pseudomorphic heterojunction field effect transistor application. *Materials Science and Engineering: B*, 35(1):234–238, 1995.

[66] Soo-Jin Chua and Seng Hin Lee. Contact resistivity dependence on ge: Ni ratio in auniauge metallization on n-gaas. *Japanese journal of applied physics*, 33(1R):66, 1994.

[67] Anna Baranska, Anna Szerling, Piotr Karbownik, Krzysztof Hejduk, Maciej Bugajski, Adam Laszcz, Krystyna Golaszewska-Malec, and Wojciech Filipowski. Ohmic contacts for room-temperature algaas/gaas quantum cascade lasers (qcl). *Optica Applicata*, 43(1), 2013.

[68] Masanori Murakami. Development of refractory ohmic contact materials for gallium arsenide compound semiconductors. *Science and Technology of Advanced Materials*, 3(1):1–27, 2002.

[69] Yih-Cheng Shih, Masanori Murakami, EL Wilkie, and AC Callegari. Effects of interfacial microstructure on uniformity and thermal stability of aunige ohmic contact to n-type gaas. *Journal of applied physics*, 62(2):582–590, 1987.

[70] M Kamada, T Suzuki, F Nakamura, Y Mori, and M Arai. Investigation of orientation effect on contact resistance in selectively doped algaas/gaas heterostructures. *Applied physics letters*, 49(19):1263–1265, 1986.

[71] Cheng-Te Lin, Chi-Young Lee, Tsung-Shune Chin, Rong Xiang, Kei Ishikawa, Junichiro Shiomi, and Shigeo Maruyama. Anisotropic electrical conduction of vertically-aligned single-walled carbon nanotube films. *Carbon*, 49(4):1446–1452, 2011.

[72] Michael Engel, Joshua P Small, Mathias Steiner, Marcus Freitag, Alexander A Green, Mark C Hersam, and Phaedon Avouris. Thin film nanotube transistors based on self-assembled, aligned, semiconducting carbon nanotube arrays. *Acs Nano*, 2(12):2445–2452, 2008.

[73] Shanju Zhang, Qingwen Li, Ian A Kinloch, and Alan H Windle. Ordering in a droplet of an aqueous suspension of single-wall carbon nanotubes on a solid substrate. *Langmuir*, 26(3):2107–2112, 2009.

[74] Michael S Arnold, Alexander A Green, James F Hulvat, Samuel I Stupp, and Mark C Hersam. Sorting carbon nanotubes by electronic structure using density differentiation. *Nature nanotechnology*, 1(1):60–65, 2006.

[75] Li Shi, Deyu Li, Choongho Yu, Wanyoung Jang, Dohyung Kim, Zhen Yao, Philip Kim, and Arunava Majumdar. Measuring thermal and thermoelectric properties of one-dimensional nanostructures using a microfabricated device. *Journal of heat transfer*, 125(5):881–888, 2003.

[76] Jinquan Wei, Hongwei Zhu, Bin Jiang, Lijie Ci, and Dehai Wu. Electronic properties of double-walled carbon nanotube films. *Carbon*, 41(13):2495–2500, 2003.

[77] Jiwoong Park and Paul L McEuen. Formation of a p-type quantum dot at the end of an n-type carbon nanotube. *Applied Physics Letters*, 79(9):1363–1365, 2001.

[78] Ali Javey, Moonsub Shim, and Hongjie Dai. Electrical properties and devices of large-diameter single-walled carbon nanotubes. *Applied Physics Letters*, 80(6):1064–1066, 2002.

[79] Joshua P Small, Kerstin M Perez, and Philip Kim. Modulation of thermoelectric power of individual carbon nanotubes. *Physical review letters*, 91(25):256801, 2003.

[80] Moonsub Shim, Ali Javey, Nadine Wong Shi Kam, and Hongjie Dai. Polymer functionalization for air-stable n-type carbon nanotube field-effect transistors. *Journal of the American Chemical Society*, 123(46):11512–11513, 2001.

[81] Yangxin Zhou, Anshu Gaur, Seung-Hyun Hur, Coskun Kocabas, Matthew A Meitl, Moonsub Shim, and John A Rogers. P-channel, n-channel thin film transistors and pn diodes based on single wall carbon nanotube networks. *Nano Letters*, 4(10):2031–2035, 2004.

[82] Giles P Siddons, David Merchin, Ju Hee Back, Jae Kyeong Jeong, and Moonsub Shim. Highly efficient gating and doping of carbon nanotubes with polymer electrolytes. *Nano Letters*, 4(5):927–931, 2004.

[83] Zhiyong Zhang, Xuelei Liang, Sheng Wang, Kun Yao, Youfan Hu, Yuzhen Zhu, Qing Chen, Weiwei Zhou, Yan Li, Yagang Yao, et al. Doping-free fabrication of carbon nanotube based ballistic cmos devices and circuits. *Nano Letters*, 7(12):3603–3607, 2007.

[84] Soo Min Kim, Jin Ho Jang, Ki Kang Kim, Hyeon Ki Park, Jung Jun Bae, Woo Jong Yu, Il Ha Lee, Gunn Kim, Duong Dinh Loc, Un Jeong Kim, et al. Reduction-controlled viologen in bisolvent as an environmentally stable n-type dopant for carbon nanotubes. *Journal of the American Chemical Society*, 131(1):327–331, 2008.

[85] Jialu Zhang, Chuan Wang, Yue Fu, Yuchi Che, and Chongwu Zhou. Air-stable conversion of separated carbon nanotube thin-film transistors from p-type to n-type using atomic layer deposition of high-κ oxide and its application in cmos logic circuits. *Acs Nano*, 5(4):3284–3292, 2011.

[86] Esther García-Tuñon, Suelen Barg, Jaime Franco, Robert Bell, Salvador Eslava, Eleonora D'Elia, Robert Christopher Maher, Francisco Guitian, and Eduardo Saiz. Printing in three dimensions with graphene. *Advanced Materials*, 27(10):1688–1693, 2015.

[87] Adam E Jakus, Ethan B Secor, Alexandra L Rutz, Sumanas W Jordan, Mark C Hersam, and Ramille N Shah. Three-dimensional printing of high-content graphene scaffolds for electronic and biomedical applications. *ACS nano*, 9(4):4636–4648, 2015.

[88] Jung Hyun Kim, Won Suk Chang, Daeho Kim, Jong Ryul Yang, Joong Tark Han, Geon-Woong Lee, Ji Tae Kim, and Seung Kwon Seol. 3d printing of reduced graphene oxide nanowires. *Advanced Materials*, 27(1):157–161, 2015.

[89] Simon J Leigh, Robert J Bradley, Christopher P Purssell, Duncan R Billson, and David A Hutchins. A simple, low-cost conductive composite material for 3d printing of electronic sensors. *PLoS One*, 7:e49365, 2012.

[90] Joseph T Muth, Daniel M Vogt, Ryan L Truby, Yiğit Mengüç, David B Kolesky, Robert J Wood, and Jennifer A Lewis. Embedded 3d printing of strain sensors within highly stretchable elastomers. *Advanced Materials*, 26(36):6307–6312, 2014.

[91] Ilda Kazani, Gilbert De Mey, Carla Hertleer, Jedrzej Banaszczyk, Anne Schwarz, Genti Guxho, and Lieva Van Langenhove. Van der pauw method for measuring resistivities of anisotropic layers printed on textile substrates. *Textile Research Journal*, page 0040517511416280, 2011.

[92] N.F. Mott. Conduction in non-crystalline materials. *Philos. Mag.*, 10:835–852, 1969.

[93] Ping Sheng. Fluctuation-induced tunneling conduction in disordered materials. *Physical Review B*, 21(6):2180, 1980.

[94] J Syurik, OA Ageev, DI Cherednichenko, BG Konoplev, and A Alexeev. Non-linear conductivity dependence on temperature in graphene-based polymer nanocomposite. *Carbon*, 63:317–323, 2013.

[95] Ping Sheng, EK Sichel, and JI Gittleman. Fluctuation-induced tunneling conduction in carbon-polyvinylchloride composites. *Physical Review Letters*, 40(18):1197, 1978.

[96] J Voit and H Büttner. Fluctuation-induced tunneling and the conduction mechanism in metallic polyacetylene. *Solid State Communications*, 67(12):1233–1237, 1988.

[97] MJ Kane, N Apsley, DA Anderson, LL Taylor, and T Kerr. Parallel conduction in gaas/alxga1-xas modulation doped heterojunctions. *Journal of Physics C: Solid State Physics*, 18(29):5629, 1985.

[98] Boya Cui, Yang Tang, and M Grayson. Introducing fourier-domain mobility spectrum analysis (fmsa) to deduce multi-component carrier mobility and density. In *SPIE OPTO*, pages 937030–937030. International Society for Optics and Photonics, 2015.

[99] S Hava and R Hunsperger. Thermoelectric properties of ga1- xalxas. *Journal of applied physics*, 57(12):5330–5335, 1985.

[100] F Ren, SJ Pearton, WS Hobson, TR Fullowan, J Lothian, and AW Yanof. Implant isolation of gaas-algaas heterojunction bipolar transistor structures. *Applied physics letters*, 56(9):860–862, 1990.

[101] T van Lippen, H Boudinov, HH Tan, and C Jagadish. Electrical isolation of alxga1–xas by ion irradiation. *Applied Physics Letters*, 80:264, 2002.

[102] AVP Coelho, H Boudinov, Tv Lippen, Hoe Hark Tan, and Chennupati Jagadish. Implant isolation of algaas multilayer dbr. *Nuclear Instruments and Methods in Physics Research Section B: Beam Interactions with Materials and Atoms*, 218:381–385, 2004.

[103] Yang Tang, G Koblmüller, H Riedl, and M Grayson. Towards p$\times$ n transverse thermoelectrics: extreme anisotropic conduction in bulk doped semiconductor thin films via proton implantation. In *SPIE OPTO*, pages 976508–976508. International Society for Optics and Photonics, 2016.

[104] W Macherzyński, M Wośko, B Paszkiewicz, B Ściana, R Paszkiewicz, and M Tłaczała. Fabrication of ohmic contact based on platinum to p-type compositionally graded algaas layers. In *Journal of Physics: Conference Series*, volume 146, page 012034. IOP Publishing, 2009.

[105] Tadao Ishibashi, Seigo Tarucha, and Hiroshi Okamoto. Si and sn doping in alxga1-xas grown by mbe. *Japanese Journal of Applied Physics*, 21(8A):L476, 1982.

[106] JJ Yang, WI Simpson, and LA Moudy. Gaas and related compounds. *Inst. of Phys., Bristol and London, Ser*, 63:107–112, 1981.

[107] F Fischer, M Grayson, D Schuh, M Bichler, and G Abstreiter. Modulating the growth conditions: Si as an acceptor in (110) gaas for high mobility p-type heterostructures. *Applied Physics Letters*, 86:192106, 2005.

[108] A. A. Snarskii and L. P. Bulat. Anisotropic thermoelements. In D. M. Rowe, editor, *Thermoelectric Handbook–Macro to Nano*, chapter 45. Taylor & Francis, 2006.

[109] H. J. Goldsmid. Transverse thermoelectric effects and their application. In David Michael Rowe, editor, *Materials, preparation, and characterization in thermoelectrics*, volume 1, chapter 1. CRC press, 2012.

[110] Ihtesham Chowdhury, Ravi Prasher, Kelly Lofgreen, Gregory Chrysler, Sridhar Narasimhan, Ravi Mahajan, David Koester, Randall Alley, and Rama Venkatasubramanian. On-chip cooling by superlattice-based thin-film thermoelectrics. *Nature Nanotechnology*, 4(4):235–238, 2009.

[111] HJ Goldsmid. Application of the transverse thermoelectric effects. *Journal of electronic materials*, 40(5):1254–1259, 2011.

[112] Th Zahner, R Förg, and H Lengfellner. Transverse thermoelectric response of a tilted metallic multilayer structure. *Applied Physics Letters*, 73(10):1364–1366, 1998.

[113] A Kyarad and H Lengfellner. Angle-dependent photovoltaic effect in al–si multilayers. *Applied Physics Letters*, 87(18):182113, 2005.

[114] A Kyarad and H Lengfellner. Transverse peltier effect in tilted pb-bi2te3 multilayer structures. *Applied physics letters*, 89(19):2103, 2006.

[115] BJ O'Brien and CS Wallace. Ettingshausen effect and thermomagnetic cooling. *Journal of Applied Physics*, 29(7):1010–1012, 1958.

[116] TS Gudkin, EK Iordanishvili, and EE Fiskind. Transverse cooling effect in a statefied medium with artificial anisotropy. *Sov. Tech. Phys. Lett*, 4(5):607–610, 1978.

[117] Syed Ashraf Ali and Sandip Mazumder. Computational study of transverse peltier coolers for low temperature applications. *International Journal of Heat and Mass Transfer*, 62:373–381, 2013.

[118] Yang Tang, Ming Ma, and M Grayson. Cooling power of transverse thermoelectrics for cryogenic cooling. In *SPIE Defense+ Security*, pages 98210J–98210J. International Society for Optics and Photonics, 2016.

[119] CF Kooi, RB Horst, KF Cuff, and SR Hawkins. Theory of the longitudinally isothermal ettingshausen cooler. *Journal of Applied Physics*, 34(6):1735–1742, 1963.

[120] L.F. Shampine, M.W. Reichelt, and J. Kierzenka. *Solving Boundary Value Problems for Ordinary Differential Equations in MATLAB with bvp4c*.

[121] VP Babin, TS Gudkin, DASHEVSK. ZM, LD Dudkin, IORDANIS. EK, VI Kaidanov, KOLOMOET. NV, OM Narva, and LS Stilbans. Anisotropic synthetic thermoelements and their maximum capabilities. *Soviet Physics Semiconductors-USSR*, 8(4):478–481, 1974.

[122] AG Samoilovich, MV Nitsovich, and VM Nitsovich. On the theory of anisotropic thermoelectric power in semiconductros. *physica status solidi (b)*, 16(2):459–465, 1966.

[123] Yang Tang, Boya Cui, Chuanle Zhou, and Matthew Grayson. p× n-type transverse thermoelectrics: A novel type of thermal management material. *Journal of Electronic Materials*, 44(6):2095–2104, 2015.

[124] AT Burkov and MV Vedernikov. High temperature thermoelectric power and electrical resistivity of monocrystalline rhenium; their relation with electronic structure. *Zh. Eksp. Teor. Fiz.*, 85(5):1821–1825, 1983.

[125] Khuong P Ong, David J Singh, and Ping Wu. Unusual transport and strongly anisotropic thermopower in ptcoo 2 and pdcoo 2. *Physical review letters*, 104(17):176601, 2010.

[126] AT Burkov and MV Vedernikov. Anomalous anisotropy of high temperature of thermo-emf in beryllium. *Fizika Tverdogo Tela*, 28(12):3737–3739, 1986.

[127] J-J Gu, M-W Oh, H Inui, and D Zhang. Anisotropy of mobility ratio between electron and hole along different orientations in re ge x si 1.75- x thermoelectric single crystals. *Physical Review B*, 71(11):113201, 2005.

[128] Duck-Young Chung, SD Mahanti, Wei Chen, Citrad Uher, and Mercouri G Kanatzidis. Anisotropy in thermoelectric properties of csbi 4 te 6. In *MRS Proceedings*, volume 793, pages S6–1. Cambridge Univ Press, 2003.

[129] Gerhard Span, Martin Wagner, Stefan Holzer, and T Grasser. Thermoelectric power conversion using generation of electron-hole pairs in large area pn junctions. In *2006 25th International Conference on Thermoelectrics*, pages 23–28. IEEE, 2006.

[130] André Becker, Ruben Chavez, Nils Petermann, Gabi Schierning, and Roland Schmechel. A thermoelectric generator concept using ap–n junction: Experimental proof of principle. *Journal of electronic materials*, 42(7):2297–2300, 2013.

[131] Ruben Chavez, S Angst, J Hall, J Stoetzel, V Kessler, L Bitzer, F Maculewicz, N Benson, H Wiggers, D Wolf, et al. High temperature thermoelectric device concept using large area pn junctions. *Journal of Electronic Materials*, 43(6):2376–2383, 2014.

[132] H Fronius, A Fischer, and K Ploog. Elimination of gaas oval defects and high-throughput fabrication of selectively doped al x ga 1- x as/gaas heterostructures by mbe. *Journal of Crystal Growth*, 81(1):169–174, 1987.

[133] Payam Norouzzadeh and Daryoosh Vashaee. The effect of multivalley bandstructure on thermoelectric properties of al x ga1- x as. *Journal of Electronic Materials*, 44(2):636–644, 2015.

[134] W Nernst et al. Ueber das auftreten electromotorischer kräfte in metallplatten, welche von einem wärmestrome durchflossen werden und sich im magnetischen felde befinden. *Annalen der Physik*, 265(10):343–347, 1886.

[135] WM Yim and A Amith. Bi-sb alloys for magneto-thermoelectric and thermomagnetic cooling. *Solid-State Electronics*, 15(10):1141IN31145–1144IN41165, 1972.

[136] Rudolf B Horst and Lloyd R Williams. Potential figure of merit of the bisb alloys. In *Proceedings of Third International Conference on Thermoelectric Energy Conversion, Arlington, Texas*, page 183, 1980.

[137] K Fischer, C Stoiber, A Kyarad, and H Lengfellner. Anisotropic thermopower in tilted metallic multilayer structures. *Applied Physics A*, 78(3):323–326, 2004.

[138] A Kyarad and H Lengfellner. Al-si multilayers: A synthetic material with large thermoelectric anisotropy. *Applied physics letters*, 85, 2004.

[139] Tsutomu Kanno, Kouhei Takahashi, Akihiro Sakai, Hiromasa Tamaki, Hideo Kusada, and Yuka Yamada. Detection of thermal radiation, sensing of heat flux, and recovery of waste heat by the transverse thermoelectric effect. *Journal of Electronic Materials*, 43(6):2072–2080, 2014.

[140] Kouhei Takahashi, Tsutomu Kanno, Akihiro Sakai, Hiromasa Tamaki, Hideo Kusada, and Yuka Yamada. Bifunctional thermoelectric tube made of tilted multilayer material as an alternative to standard heat exchangers. *Scientific reports*, 3, 2013.

[141] SL Korolyuk, IM Pilat, SAMOILOV. AG, SLIPCHEN. VN, AA Snarskii, and EF Tsarkov. Anisotropic thermoelements. *SOVIET PHYSICS SEMICONDUCTORS-USSR*, 7(4):502–507, 1973.

[142] I. M. Pilat. *Teplovye priemniki izlucheniya (Thermal Detectors)*. Gos. Opticheskii Inst., 1990.

[143] AA Ashcheulov, NN Glemba, and LI Prostebi. A device for rapid characterization of thermoelectric coolers. *Izv. Vyssh. Uchebn. Zaved., Elektromekh*, (12):1333, 1980.

[144] A. A. Ashcheulov, V. M. Kondratenko, N. K. Voronka, and I. M. Rarenko. *Direct Methods of Energy Conversion*. Ashkhabad, 1986.

[145] Lukyan Ivanovich Anatychuk. Thermoelements and thermoelectric devices. *K.: Naukova Dumka Publ*, page 768, 1979.

[146] BK Voronov, LD Dudkin, and NN Trusova. Anisotropy of thermoelectric properties in chromium disilicide and in single crystals of the highest silicide of manganese. *SOV PHYS CRYSTALLOGR, NOV-DEC. 1967, 12,–3–, 448-449*, 1967.

[147] ZH He, ZG Ma, QY Li, YY Luo, JX Zhang, RL Meng, and CW Chu. Investigation of transverse peltier effect on top-seeded melt textureyba2cu3o7- δ. *Applied physics letters*, 69(23):3587–3589, 1996.

[148] XH Li, H-U Habermeier, and PX Zhang. Laser-induced off-diagonal thermoelectric voltage in la 1- x ca x mno 3 thin films. *Journal of Magnetism and Magnetic Materials*, 211(1):232–237, 2000.

[149] Kun Zhao, Kui-Juan Jin, Yan-Hong Huang, Hui-Bin Lu, Meng He, Zheng-Hao Chen, Yue-Liang Zhou, and Guo-Zhen Yang. Laser-induced ultrafast photovoltaic effect in la 0.67 ca 0.33 mno 3 films at room temperature. *Physica B: Condensed Matter*, 373(1):72–75, 2006.

[150] WM Huber, ST Li, A Ritzer, D Bäuerle, H Lengfellner, and W Prettl. Transverse seebeck effect in bi2sr2cacu2o8. *Applied Physics A*, 64(5):487–489, 1997.

[151] Tsutomu Kanno, Satoshi Yotsuhashi, and Hideaki Adachi. Anisotropic thermoelectric properties in layered cobaltite a {sub x} coo {sub 2}(a= sr and ca) thin films. *Applied physics letters*, 85(5), 2004.

[152] GD Tang, HH Guo, T Yang, DW Zhang, XN Xu, LY Wang, ZH Wang, HH Wen, ZD Zhang, and YW Du. Anisotropic thermopower and magnetothermopower in a misfit-layered calcium cobaltite. *Applied Physics Letters*, 98(20):202109, 2011.

APPENDIX A

Transverse thermoelectric phenomena

By definition, a transverse thermoelectric effect exists whenever a material has a non-zero transverse Seebeck coefficient S_{xy}. In this section we review the three most prominent transverse thermoelectric phenomena with different origins of S_{xy}, namely the Nernst-Ettingshausen (N-E) effect, in which a magnetic field induces the transverse effect, two-phase stacked synthetic materials in which macroscale anisotropy yields the transverse effect, and homogeneous anisotropic crystals with unipolar Seebeck, whose band structure gives rise to the transverse effect.

I) Nernst-Ettingshausen Effect

The Nernst-Ettingshausen (N-E) effect [**134**] is a thermomagnetic effect in which a magnetic field is used to induce a transverse heat flow perpendicular to both the electrical current and the magnetic field (Fig. A.1a), resulting in a non-zero S_{xy}. This effect occurs in semimetals or semiconductors in which there is an abundance of both electrons and holes in approximately equal number. Whereas the longitudinal thermoelectric effect is compromised when there are two types of charge carrier, because electrons and holes carry heat in opposite directions, in the N-E effect the magnetic field B gives electrons and holes a common direction of motion perpendicular to the applied current, and this Lorenz force drives the net component of the heat in the same direction. Whereas the superiority of longitudinal thermoelectrics has been established in applications above room temperature, the N-E effect outperforms more standard methods at low temperatures at

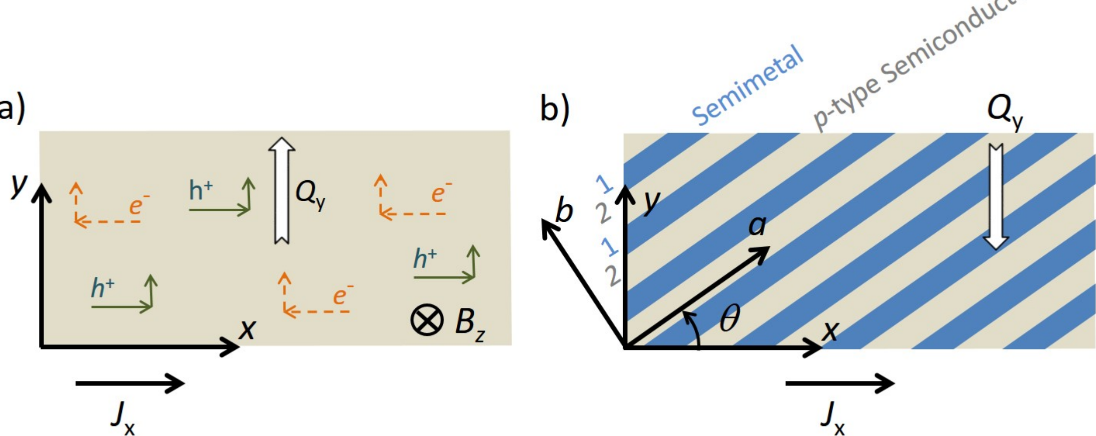

Figure A.1. (a) NernstEttingshausen effect. In the presence of a B-field, electrons and holes in a semimetal or narrow-gap semiconductor both feel a Lorenz force component in the upwards direction, resulting in a net heat flow transverse to the electrical current. (b) A stacked synthetic transverse thermoelement cut from a two-phase (1 and 2) layered material. The anisotropic Seebeck tensor arises from having the layers in series along one axis, and in parallel along the other axis.

which doped semiconductors would freeze out. Thus, some semimetals, for example, Bi [**135**], and narrow-gap semiconductors, for instance, Bi-Sb alloys [**135**, **136**], can be useful thermomagnetic materials at low temperatures, at which the mobility μ is large enough for the product $\mu B \geq 1$ (Ref. [**10**], chapter 8).

Research on thermomagnetic cooling was most active from the 1960s to 1980s, and focused on Bi and BiSb alloys. Yim and Amith [**135**] observed a thermomagnetic figure-of-merit $Z_{xy}T = 0.33$ at 115 K with the alloy $Bi_{0.99}Sb_{0.01}$ in a magnetic field up to 0.8 T. Horst and Williams [**136**] subsequently increased this value to $Z_{xy}T = 1.0$ at 150 K in a magnetic field of 1.0 T by using the alloy $Bi_{0.97}Sb_{0.03}$. Geometrical enhancement of cooling

in transverse thermoelements has been demonstrated at cryogenic temperatures with a $Bi_{0.97}Sb_{0.03}$ N-E cooler, with $\Delta T = 36$ K for a rectangular cooler and $\Delta T = 54$ K for an exponential shape cooler in a 1.5 T magnetic field at 156 K heat sink temperature [**119**]. However, the strong magnetic field limits practical applications of the N-E effect.

The N-E effect is quantified in terms of the Nernst coefficient, defined as:

$$N = -\frac{E_x/B_z}{dT/dy}, \tag{A.1}$$

which gives rise to a transverse Seebeck component $S_{xy} = NB_z$. Explained qualitatively, this equation implies that a thermal diffusion current (Q_y), as a result of the temperature gradient, dT/dy, induces a transverse drift current flow (J_x), because of the Lorenz force in a perpendicular magnetic field (B_z). At equilibrium, the charges accumulate to build up a transverse Seebeck voltage in the x direction, resulting in a transverse electric field E_x and a counter-propagating diffusion current $J'_x = -J_x$ that compensates J_x.

II) Two-Phase Stacked Synthetic Materials

Another transverse thermoelectric phenomenon, introduced in the 1970s, is that observed in two-phase [**109**] stacked synthetic transverse thermoelectrics. These materials realize Seebeck anisotropy with alternating slabs of semiconductor with large Seebeck coefficient and (semi)metal with large electrical and thermal conductivity (Fig. A.1b). The anisotropy of the resulting diagonalized Seebeck tensor can, by basis rotation, be turned into a non-zero transverse Seebeck coefficient. An electrical current applied at an optimum angle will induce a transverse heat flow, and the angle can be chosen to maximize the transverse figure of merit.

The two-phase stacked synthetic transverse thermoelement can be used for Peltier cooling. It was first proposed by Babin *et al.* [**121**] in 1974, and later demonstrated by Gudkin et al. [**116**], by use of a BiSbTe-Bi two-phase system, in 1978. They observed a good transverse figure-of-merit $Z_{xy}T = 0.25$ and Peltier cooling of $\Delta T = 23$ K with a rectangular block. The cooling was enhanced to $\Delta T = 35$ K by use of a trapezoidal block, the cold side of which was one tenth the width of the heat sink. Interest in transverse Peltier cooling decreased after the 1980s but has been renewed in recent years because of the need for miniaturized cooling devices for microelectronics. In 2006 Kyarad and Lengfellner [**113**,**114**] achieved 22 K cooling by use of Bi_2Te_3Pb multilayer structures with a simpler form of construction. However, two-phase synthetic transverse Peltier coolers are limited in conventional thermoelectric cooling because they have lower figure-of-merit than commercial longitudinal Peltier coolers. Other applications, for example, microscale cooling, are also limited because the slabs are, typically, of millimeter dimensions and such implementations are very difficult to reduce to the micro-scale for electronics or thin-film applications [**109**]. Furthermore, the extrinsic doping eliminates the possibility of cryogenic cooling, because charge carriers in the extrinsic semiconductor layer freeze out at the low-temperature limit.

The transverse Seebeck effect in two-phase stacked synthetic transverse thermoelements has also been studied. Zahner et al. demonstrated use of transverse thermoelements made of alternating layers of copper and constantan with a relatively fast response ($\tau = 0.1$ ms for a sample 0.1 mm thick) as thermal detectors [**112**]; later, a similar response time was reported by Fischer et al. [**137**] for constantanchromel multilayers. Kyarad and Lengfellner [**138**] reported large Seebeck anisotropy of approximately 1.5 mV/K in AlSi

multilayers and estimated the response time to be $\tau = 1$ μs for samples 0.1 mm thick. Kanno et al. [139] reported a serpentine Bi/Cu heat flux sensor with a simple layered structure and a sensing capability of 0.4 $\mu V(Wm^{-2})^{-1}$. The transverse Seebeck effect has also been studied for power generation. As recently reported by Takahashi et al. [140], an 11-cm-long tubular thermoelectric generator based on $Bi_{0.5}Sb_{1.5}Te_3$/Ni was able to provide an open-circuit voltage of 240 mV and power of 2.7 W under a temperature difference $\Delta T = 85$ K created by hot fluid inside the tube ($T_H = 368$ K) and cold fluid outside ($T_C = 283$ K), pushing synthetic transverse thermoelectrics closer to commercial applications of waste heat recovery from fluid media.

As already mentioned, the transverse Seebeck coefficient in two-phase stacked synthetic materials arises from the different character of the two thermoelectric materials. Suppose components 1 and 2 in the two-phase stacked synthetic system have Seebeck coefficients S_1 and S_2 and are of the same thickness. In the parallel direction (a direction) each component will contribute to the Seebeck voltage according to its electrical conductance, *i.e.*, they behave like two Seebeck generators in parallel connection which are subjected to the same temperature gradient. Thus:

$$S_a = \frac{S_1\sigma_1 + S_2\sigma_2}{\sigma_1 + \sigma_2}. \tag{A.2}$$

In the perpendicular direction (b direction), each component will contribute according to its thermal resistance, because they are connected in series, which leads to:

$$S_b = \frac{S_1/\kappa_1 + S_2/\kappa_2}{1/\kappa_1 + 1/\kappa_2}. \tag{A.3}$$

Ideally S_1 and S_2 should be large and of opposite sign and the electrical and thermal conductivities should be greatly imbalanced, $\sigma_1 \gg \sigma_2$ and $\kappa_1 \gg \kappa_2$; then, in the a direction the overall Seebeck coefficient will be approximately equal to S_1 and in the b direction it will be close to S_2, resulting in the large Seebeck anisotropy. As discussed in Section 4.1.1, the Seebeck anisotropy can be converted to a non-zero transverse Seebeck coefficient by cutting from the two-phase material at an angle θ.

III) Anisotropic Crystals with Unipolar Seebeck Coefficients

Some homogeneous anisotropic crystals also have unipolar, anisotropic Seebeck coefficients and a corresponding transverse component of the thermoelectric effect. Here "unipolar" means that the Seebeck coefficient in all directions has the same sign but different magnitude. According to theory [**122**], the highly anisotropic Seebeck tensor can arise either from mixed conduction of electrons and holes, or from single-carrier-dominated conduction.

Mixed conduction of electrons and holes usually leads to an intrinsic transverse thermoelectric component in semimetals and narrow-gap semiconductors. Korylyuk et al. [**141**], in 1973, were the first to demonstrate a transverse thermoelectric effect in the single crystal, narrow-gap semiconductor CdSb ($E_g = 0.49$ eV), which had large Seebeck anisotropy $\Delta S = 280\mu\text{V/K}$ but a small figure-of-merit $Z_{xy}T \approx 0.002$. The conduction in CdSb is intrinsic, mixed conduction near room temperature [**142**], and, because of the relative temperature independence of the thermoelectric coefficients combined with optical

transparency, CdSb and its eutectics have been used in rapid transverse radiation detectors [143, 144]. The semimetal Bi was the material used in the first transverse thermoelement, dubbed at the time an "anisotropic thermoelement" by the authors, with $\Delta S \approx 50\mu V/K$ and $Z_{xy}T \approx 0.02$ [145].

Single-carrier-dominated materials with a unipolar anisotropic Seebeck tensor have also been reported. Some silicon compounds, for example $MnSi_{1.75}$ [10, p. 299] and $CrSi_2$ [146], have Seebeck anisotropy ($\Delta S \approx 50 - 100\mu V/K$ at 300 K) over a wide temperature range (2001000 K for $CrSi_2$). High-T_C superconductors YBCO [147], LCMO [148, 149], and $Bi_2Sr_2Ca\text{-}Cu_2O_8$ [150] and stoichiometries of CaCoO [151,152], have also been shown to have a weak transverse Seebeck coefficient $S_{xy} \approx 1-35\mu V/K$ induced by heat flux from a laser. Thin films made from these materials have shown potential as ultrafast heat-flux sensors, for example, picosecond response was observed for a $YBa_2Cu_3O_{7-\delta}$ thin film 10 nm thick at room temperature [37].

The anisotropic Seebeck tensor of anisotropic crystals can arise in the presence of two or more anisotropic scattering mechanisms, or in the presence of two types of charge carrier if at least one type has an anisotropic effective mass [122]. It has been shown that for a single-carrier material with one scattering mechanism the Seebeck coefficient is isotropic irrespective of crystal anisotropy. The Seebeck tensor becomes anisotropic only when the conduction in different directions is dominated by different scatteringmechanisms, or under anisotropic conduction of several carrier species [108].

Despite the ability of transverse materials to serve as rapid-response heat-flux sensors, they do not fulfill their potential as high-output voltage power generators and compact,

micro-scale Peltier coolers. The existing materials described above either require an external magnetic field, cannot be scaled-down in fabrication, or suffer from values of the transverse figure-of-merit or Seebeck coefficient which are too small. To overcome these limitations and to enhance the transverse figure-of-merit, it is worth studying ways of artificially inducing a larger transverse Seebeck coefficient, and studying other materials with strong Seebeck anisotropy for possible use as transverse thermoelectric materials.

Vita

NAME: Yang Tang

BORN: May 20th, 1988 in Suining, Sichuan Province, China.

EDUCATION: Ph.D. in Electrical Engineering at Northwestern University, September 2009 – December 2016.

Bachelor of Science in Microelectronics at Peking University, Beijing, China, September 2005 – June 2009.

PUBLICATIONS:

1. **Yang Tang**, Boya Cui, Chuanle Zhou, and M. Grayson. "$p \times n$-Type Transverse Thermoelectrics: A Novel Type of Thermal Management Material." Journal of Electronic Materials 44, No. 6 (2015): 2095-2104.
2. Chuanle Zhou, S. Birner, **Yang Tang**, K. Heinselman, and M. Grayson. "Driving Perpendicular Heat Flow:($p \times n$)-Type Transverse Thermoelectrics for Microscale and Cryogenic Peltier Cooling." Physical Review Letters 110, No. 22 (2013): 227701.
3. Nagaraja, Arpun R., Nicola H. Perry, Thomas O. Mason, **Yang Tang**, Matthew Grayson, Tula R. Paudel, Stephan Lany, and Alex Zunger. ”Band or Polaron:

The Hole Conduction Mechanism in the p-Type Spinel Rh_2ZnO_4." Journal of the American Ceramic Society 95, No. 1 (2012): 269-274.

4. Perkins, J. D., Paudel, T. R., Zakutayev, A., Ndione, P. F., Parilla, P. A., Young, D. L., **Yang Tang**, M. Grayson, T. O. Mason, J. S. Bettinger, Y. Shi, and M. F. Toney. "Inverse design approach to hole doping in ternary oxides: Enhancing p-type conductivity in cobalt oxide spinels". Physical Review B, 84(20), (2011): 205207.
5. Stevens, Blake L., C. A. Hoel, C. Swanborg, **Yang Tang**, Chuanle Zhou, M. Grayson, K. R. Poeppelmeier, and S. A. Barnett. "DC reactive magnetron sputtering, annealing, and characterization of $CuAlO_2$ thin films." Journal of Vacuum Science & Technology. A. Vacuum, Surfaces, and Films 29, No. 1 (2011): 11018.
6. **Yang Tang**, Ming Ma, and M. Grayson. "Cooling power of transverse thermoelectrics for cryogenic cooling." SPIE Defense+ Security (pp. 98210J-98210J). International Society for Optics and Photonics, 2016.
7. **Yang Tang**, G. Koblmüller, H. Riedl, and M. Grayson. "Towards $p \times n$ transverse thermoelectrics: extreme anisotropic conduction in bulk doped semiconductor thin films via proton implantation." SPIE OPTO (pp. 976508-976508). International Society for Optics and Photonics, 2016.
8. **Yang Tang**, and M. Grayson. "Magnetotransport potentials for anisotropic thin films with stripline and ground plane contacts." SPIE OPTO (pp. 93700L-93700L). International Society for Optics and Photonics, 2015.

9. Boya Cui, **Yang Tang**, and M. Grayson. "Introducing Fourier-domain mobility spectrum analysis (FMSA) to deduce multi-component carrier mobility and density." SPIE OPTO (pp. 937030-937030). International Society for Optics and Photonics, 2015.
10. Chuanle Zhou, **Yang Tang**, and M. Grayson. "$p \times n$-type transverse thermoelectrics: an alternative Peltier refrigerator with cryogenic promise." SPIE OPTO (pp. 900006-900006). International Society for Optics and Photonics, 2014.